Myelin Water Imaging Using Transverse Relaxation

by

Nima Mehdizadeh

A thesis submitted in partial fulfillment of the requirements for the degree of

Master of Science

Department of Biomedical Engineering
University of Alberta

Abstract

Tracking myelination and demyelination in the brain is a crucial part of studies on neurodegenerative diseases such as Multiple Sclerosis (MS). Classic MRI techniques are unable to provide enough information about the pathology of tracts and lesions. Multi-component analysis of multi-echo data has shown promising results in the field of myelin water imaging (MWI). Such analyses are predicated on the assumption that multi-echo signal acquired from a specific voxel in the brain can be sourced to various water compartments, which go through relaxation at different paces independently. Numerous techniques have been developed to model MRI signals to acquire the proportion of water compartments to track myelin content. This ratio is typically called the myelin water fraction (MWF) value.

In this thesis, we implemented multi-component analyses for MWF from multi-echo gradient or spin echo sequences based on past literature. Once implemented, we investigate advances in analysis for each method. Using multi-echo spin-echo (MESE), constraining the transmit RF field $B_1{}^+$ parameter for the process of MWI analysis was investigated by supplying $B_1{}^+$ using an independent mapping sequence. This new approach was compared to the standard MWI method of estimating the B1+ from the decay curve. Simulations were performed using the same principles and modeling prescribed for the fitting procedure to analyze our proposition.

By comparing the estimation results and reference data, we found a notable difference which resulted in significant changes in MWF maps using the proposed method. In 3D MESE data, approximated by a 3D gradient and spin echo (GRASE) sequence, MWF values were generally underestimated in white matter regions using the stan-

dard method. Similar patterns were observed in 2D MESE data, however, estimations in the in-vivo results showed major underestimations where B_1^+ was more than 1.05; and we noticed stronger deviation from the reference B_1^+ maps in 2D MESE compared to 3D data. The MWF brain maps from the standard method were in alignment with estimated maps demonstrated in previous literature. Results were partly in alignment with simulations, but the in-vivo estimations showed skewness and bias in the optimization step that is responsible for estimation of B_1^+; which could be due to the artifacts present in MRI data. In short, supplying the B1+ parameter via an independent flip angle map was found to offer improvements in both 2D and 3D MWF methods. The major improvement was supplying greater certainty in this key parameter, rather than attempting estimation from the MWI sequence that may be limited by SNR, artifacts or duplicate B_1^+ solutions.

For MWI from multi-echo gradient echo (MEGRE) data, standard two and three pool analysis models were implemented and tested in human brain subjects. The effects of previously-introduced spatial saturation were examined and a non-local filter to overcome low SNR issues was proposed. The application of a saturation pulse in ME-GRE data acquisition helped with reducing the physiological noise arising from the blood inflow as previously suggested by the literature. Using the non-local filter showed improvements in image quality of MWF maps, and the correlation coefficient of ME-GRE results compared to the reference method increased when using the three-pool model.

In conclusion, this thesis work has implemented spin echo and gradient echo-based analysis methods for myelin water imaging in human brain on a 3T system. Advances in MESE-type approaches introduced an independent flip angle (B_1^+) map to constrain solutions for both 2D and 3D sequences. MEGRE methods were briefly studied as well including applying a non-local filter.

Preface

This thesis is an original work by Nima Mehdizadeh. No part of this thesis has been previously published.

Acknowledgements

In the first year of this M.Sc. program, we were focusing on ME-GRE based MWI projects; and I was wondering whether the path we were on had any justifications and what it was that we were looking for. I shared my concerns with my supervisor, Dr. Alan Wilman, and his response was that our mission as researchers is to take every path, look down every rabbit hole to see if there is something useful (I am paraphrasing of course). His response was so appealing to me that I started some projects according to my impression of it. Naturally, these projects were mostly of the high-risk high-return kind, as they were most interesting and alluring rabbit holes. These projects took a lot of time and to no surprise, almost all of them failed. I can safely say if Dr. Wilman did not interfere with the direction of my research, most probably this thesis would only contain a bunch of failed attempts; for that, I am truly grateful. I am very lucky that my supervisor was not only a good person but a great mentor as well.

I would like to thank my dear parents and friends for all their supports and helps along this journey what they call a master's program.

Table of Contents

List of Tables

List of Figures

Chapter 1

Introduction

Magnetic resonance imaging (MRI) has undoubtedly been proven a very useful tool for soft tissue imaging in the brain. In addition, many MRI techniques are sensitive to myelin content in the brain. More specifically, quantitative MRI (qMRI) techniques have been developed over the years to indirectly study the myelination/de-myelination in the nervous system in diseases such as multiple sclerosis. One category of these indirect myelin tracking techniques is commonly described as myelin water imaging (MWI) methods. These techniques try to estimate myelin content by manipulating the MRI signal originated from the water trapped in myelin bi-layers, named myelin water (MW). This thesis focuses on the major subdivision of such methods that use multi-component transverse relaxation (T_2 and T_2^*) measurements to calculate the portion of MW in the brain as a myelin water fraction (MWF).

This introduction covers information about myelin structure and function, along with some common MWI techniques. It also reviews common practices using T_2 or T_2^* parameter to calculate MWF and the underlying considerations, such as modeling the signal and sequence parameters.

1.1 Myelin

1.1.1 Myelin function and structure

Neurons or nerve cells are the main components of brain and peripheral nervous system (PNS), and carry out the responsibility of processing and transmission of electrical signals. A nerve cell (Figure 1.1) is comprised of the cell body or soma (non-processing portion that contains the nucleus), dendrites (protoplasmic extensions that receive electrochemical stimulations), axon or nerve fiber (conducts electrical impulses known as action potentials), and synaptic terminals (which pass electrochemical signals to other neurons) [1].

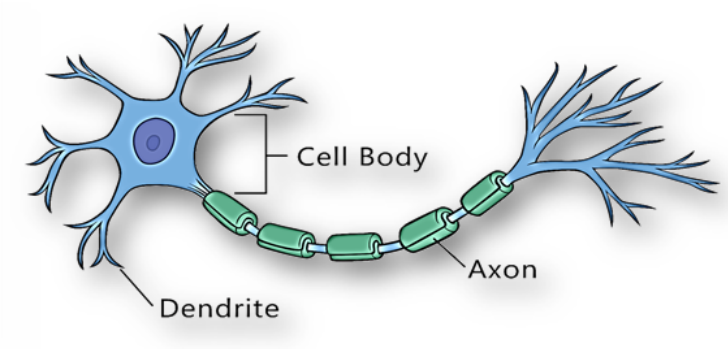

Figure 1.1: A sketch of a typical nerve. From left to right are dendrites, soma, myelinated axon, and synaptic terminals.

Two major components of the central nervous system (CNS) are gray matter (GM) and white matter (WM). GM is mostly comprised of cell bodies, while WM contains relatively few cell bodies and mainly is composed of axons. Axons in WM are generally covered by a multilayer stack of uniformly thick membranes called myelin [2]. Myelin consists of bilayers composed of roughly 80% lipid and 20% protein, which is unusual since other membranes are generally 50% lipid and 50% protein [1]. Myelin fibers act as electrical insulators for neurons and have evolved to increase saltatory conduction, and reduce energy requirements which may thus help the organism to withstand low oxygen or starvation periods [3].

In Figure 1.2, the major dense lines represent myelin sheaths. Between myelin sheaths are small extracellular spaces [2], that are approximately 30 Å wide and filled with water which is referred to as myelin water. This myelin water is the primary component in all of the indirect methods probing the myelin content, and the definition of myelin water includes all water that is in close contact with myelin bilayers [4].

There are several neurological diseases such as MS that will cause demyelination in the WM and create demyelinated areas referred to as lesions. Lesion is a general pathologic term referring to focal areas of abnormal tissue [1]. MRI is very sensitive to white matter (WM) abnormalities and detection of lesions in MS with standard T_2-weighted imaging, with or without fluid suppression. However, there are a number of processes that can lead to changes in the signal intensity (*e.g.* edema, gliosis, demyelination); thus conventional MRI techniques have difficulty in detecting the full pathological state of such lesions [5]. Therefore, over the years, efforts have been made to produce MRI techniques that are able to probe the state of lesions and quantify myelin content. These techniques can be generally separated into two categories: direct methods (directly quantify the signal originating from the myelin bi-layers) and indirect methods (use other means to estimate the myelin content) [5].

1.1.2 Myelin Content via Myelin Water

In MRI, the signal is mainly originated from hydrogen protons. The mobility of these protons determines the T_2 relaxation times. Hydrogen protons in water molecules have high mobility and display moderate to long T_2 times ($> 10ms$). Hydrogen protons which are part of macromolecules (*e.g.* proteins and myelin lipids) are much less mobile, hence they have a much shorter T_2 time ($10\,\mu\text{s} < T_2 < 1\,ms$) [5]. In the direct methods, the main goal is to acquire the signal directly arising from protons in the myelin sheaths. Therefore, ultra-short echo time sequences are implemented in these methods, however, very short T_2 signals are not specific to myelin bi-layers [7]. Meanwhile, indirect methods like magnetization transfer (MT) and multi-component

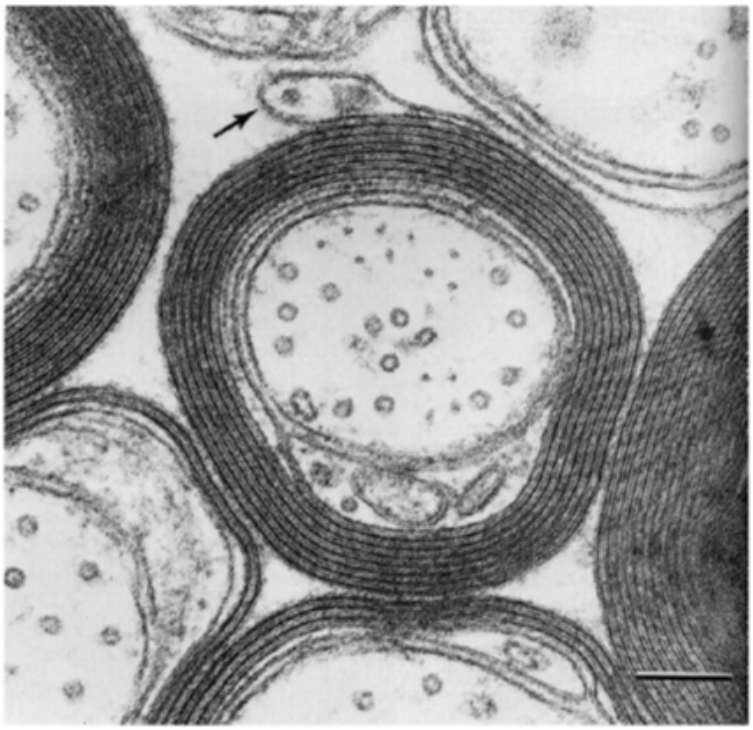

Figure 1.2: Electron micrograph shows a cross-section of a myelinated nerve. The bar in the bottom right corner represents 0.1 μm $\times$ 150000 [6]

transverse relaxation analyses, try to measure the portion of myelin water instead. MT tries to benefit from the fact that myelin water is in close contact with lipid bi-layers and implements two different acquisitions; One acquisition adopts a saturating RF pulse pre-acquisition that has excitation frequency outside of the bandwidth of free water, and the other one without any saturating pulses. The saturation pulse excites the protons in macromolecules and thus saturates the magnetization of the water protons that are in contact with them. Therefore, there would be a difference between the signals of the two acquisitions proportionate to the protons of the macromolecules. Using this principle one can calculate the so-called MT ratio [8]. In theory when there is more myelin water present in an arbitrary voxel more water would be saturated, which means there would be a larger MT value. However, myelin bi-layers are not the only source of bounded protons, which decreases the correlation of myelin content with the calculated MT ratio.

Multi-component fitting methods are the main focus here, and the principle idea behind all these methods is to use transverse relaxation parameter to distinguish between myelin water signal and other water compartments. All such multi-echo analyses are based on the underlying assumption that water exchange between the water compartments is slow enough that it would not affect the T_2 relaxometry solutions [9]. Most of these methods are developed on a single voxel basis, which means that the analysis would be applied to each voxel independently. There have been attempts to use multi-voxel based algorithms, which assume that myelin content in the brain varies slowly and applies a smoothness factor accordingly [10]. However, there are not enough pathological studies that would back results from multi-voxel analyses. Moreover, the assumption for spatial smoothness might not hold in cases with demyelinated lesions. Herewith, all the analyses presented in this research are done on a single voxel basis.

1.2 Multi-component T_2 Relaxometry

1.2.1 T_2 Relaxation

As the importance of transverse relaxation has been established, it would be beneficial to review the basics of this parameter before getting into the multi-component analysis. In the presence of an external constant magnetic field, $\vec{B_0}$, the ensembles of spins will tend to align slightly more in the main magnetic field direction producing a net magnetic moment, $\vec{M_0}$, at thermal equilibrium [11, 12]. By application of a radio-frequency (RF) pulse (excitation pulse) the orientation of this magnetic moment may be altered. The spins tend to return to equilibrium after some time and can be described using two processes: longitudinal and transverse relaxation. The longitudinal relaxation, also known as spin-lattice relaxation, is the process of returning the longitudinal magnetization to thermal equilibrium. The transverse relaxation, also known

as spin-spin relaxation can be described as the divergence of excited spins precession, causing loss of transverse magnetization (induced signal) [13]. The T_2 parameter is the decay time constant for the dynamic processes that govern the relaxation of the transverse magnetization. The effects of the static processes that contribute to transverse magnetization are refocused in spin-echo acquisitions with an RF pulse (typically a 180° pulse). The static processes are external field induced (*e.g.* susceptibility sources) and the dynamic processes are thermodynamic in nature [14]. Spin dynamics can be described using Bloch equations in the rotating frame [15]:

$$\frac{d\vec{M}}{dt} = \gamma\vec{M} \times \vec{B} - \frac{M_x\hat{x} + M_y\hat{y}}{T_2} - \frac{(M_z - M_0)\hat{z}}{T_1} \tag{1.1}$$

Where, B_0 is conventionally aligned along the $\hat{z}$ axis, and considering $M_{xy} = M_x + iM_y$, yields the following solutions in the rotating frame:

$$M_{xy} = M_{xy}(0)exp(-t/T_2) \tag{1.2}$$

$$M_z = M_0 + [M_z(0) - M_0]exp(-t/T_1) \tag{1.3}$$

Where $M_{xy}(0)$ and $M_z(0)$ are the initial magnetizations in the transverse plane along the longitudinal axis, respectively.

Transverse relaxation of a sample is governed by the frequency distribution of the randomly fluctuating background magnetic field and by static field effects. Low frequency oscillating local dipolar fields can affect the precessional frequency of local nuclei, contributing to local de-phasing of the transverse magnetization. Such low-frequency content of local dipolar fields increases monotonically as the molecular motion decreases, resulting in shortening of the T_2. These dipole-dipole interactions are believed to be the dominant mechanism determining relaxation rates [16]. In heterogeneous environments (*e.g.* biological tissues), water protons interact with a variety of macromolecules (*e.g.* lipids and proteins) which relatively restrict the motion of ions; and also membranes that restrict motion of water and bind water protons

in a smaller area compared to free water; the aftermath of this motion restriction of protons is shortening of the T_2 parameter of the affected water-compartment [13, 14]. Relaxation is also affected by the rate of exchange between water compartments in multi-component media [13]. If the water exchange rate is faster than the decay due to relaxation, the sample would assume a relaxation time constant that is the weighted average of T_2 values of the contributing compartments. However, if the exchange rate is slower, relaxation can be described as multi-exponential relaxation, which is usually observed in myelinated regions such as WM [1, 14].

1.2.2 Myelin Water Imaging Using T_2 Parameter

Prior to the introduction of MWI using multi-component T_2 analysis, several in vitro NMR studies investigated spin-spin relaxation in tissue in the nervous system and WM. Vasilescu *et al.* [17] applied relaxation measurements to water in the frog sciatic nerve and found three distinct relaxation components. Later in 1991, Menon and Allen [18], applied linear analysis to in-vitro relaxation time measurements and found up to four reproducible components for the transverse relaxation. Such in-vivo studies found that about one-sixth of the total WM has a relatively short T_2 relaxation time (ranged from $10\,ms$ to $40\,ms$), and they associated this water reservoir with myelin water [9, 19]. These findings inspired Mackay and his colleagues to replicate the same experiment in vivo, which lead to a landmark paper that started a chain of future studies in this field. Mackay *et al.* [19] carried out a simple experiment, in which they applied a single slice Carr-Purcell-Meiboom-Gill (CPMG) sequence to acquire multi-echo T_2 signal decay (32 echoes in total). Then they applied a non-negative least squares (NNLS) method to the multi-echo signal of each voxel and observed three different peaks in the T_2 distribution (Figure 1.3b). The shorter T_2 components were associated with water trapped within myelin sheaths and the longer T_2 components were identified as extra/intra-cellular water (IE water). The third component with a very long T_2 time ($> 1\,s$) was linked to CSF.

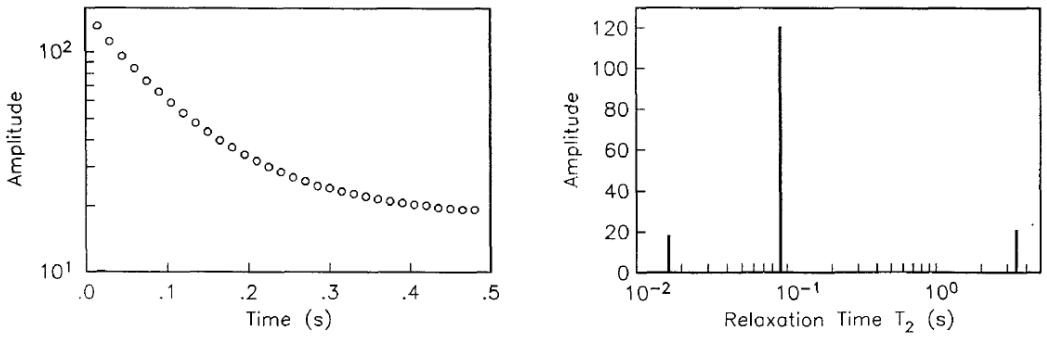

(a) (b)

Figure 1.3: a) Spin-spin relaxation decay curve from a volume of interest in normal-appearing WM (in vivo). b) T_2 relaxation distribution from the decay curve in (a). The three components are assigned to: i) water compartmentalized in the myelin sheath with T_2 between 10 and $55\,ms$, ii) water in cytoplasmic and extracellular spaces with T_2 between 70 and $95\,ms$, and iii) cerebrospinal fluid with T_2 greater than $1\,s$ [19].

Moreover, Mackay *et al.* tried to calculate the ratio of myelin water peak to the total water in the signal decay and defined it as myelin water fraction (MWF). Later in a study by Beaulieu *et al.* [20], it was found that the short T_2 signal component was exclusively existent in myelinated nerves. In 2006, Laule *et al.* [7] scanned post-mortem brains and then photographed stained samples to acquire Luxol fast blue (LFB) mean optical densities (OD) to correlate with MWF values (Figure 1.4). Their studies showed high correlation can be found in several pathological studies in [7, 21, 22].

1.2.3 Three Dimensional Gradient Echo Spin Echo (3D-GRASE)

Similar to the early days of many other innovative ideas, Mackay's method had issues and challenges. To name a few: specific absorption rate (SAR) issues for short echo times ($\leq 10ms$), noise effect problems for MWF and T_2 distribution, and most importantly long acquisition time ($25\,min$) [23]. For a whole-brain acquisition, scan time would be too long to be even considered practicable for clinical settings [24]. Therefore, over the following years after their paper, many have attempted to create

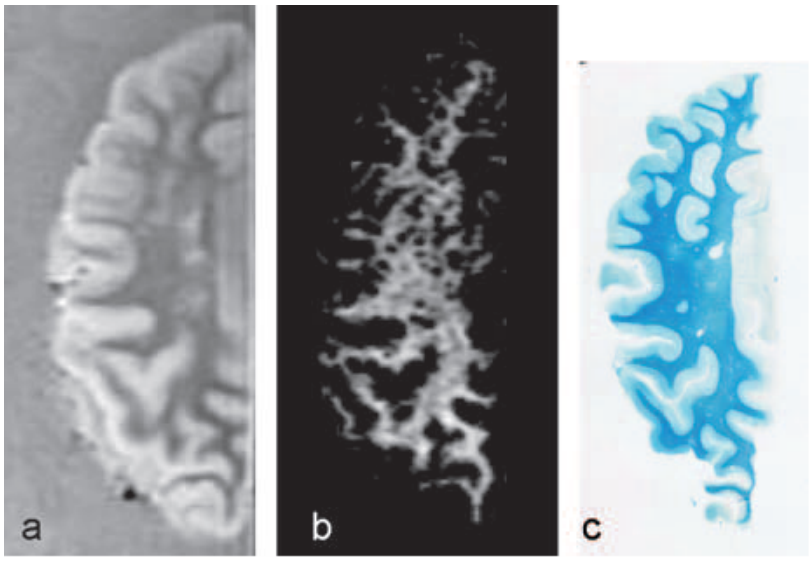

Figure 1.4: Comparison of MRI results and histopathology. There seem to be a good qualitative correlation between (a) TE =10 milliseconds, (b) myelin water image, and (c) LFB [7].

MWF maps using more feasible methods and sequences, employing the same principles.

Multi-slice excitation might be contaminated by magnetization transfer (MT) effects, which may lead to the underestimation of MWF in the affected regions [24]. Thus to reduce MT effects, a safe approach would be to excite a 3D slab to acquire MESE data, which would lead to a very long acquisition time. To overcome the long scan time, Mädler and Mackay in 2007, introduced 3D-GRASE which also has sequence limitations [24], which we will circle back to later in this chapter.

Figure 1.5, portrays the GRASE pulse sequence. This sequence adopts the same principles as 3D-MESE. First, a $90°x$ RF pulse is applied, and then a train $180°y$ refocusing RF-pulses. There are two k-space lines with additional $T_2{}^*$ weighting which are collected around the main echo time, which are the source of acceleration. The gradient echo weighted k-space lines capture the outer lines of the k-space and main echoes capture the center lines. This introduces some $T_2{}^*$ weighted artifacts to the final images.

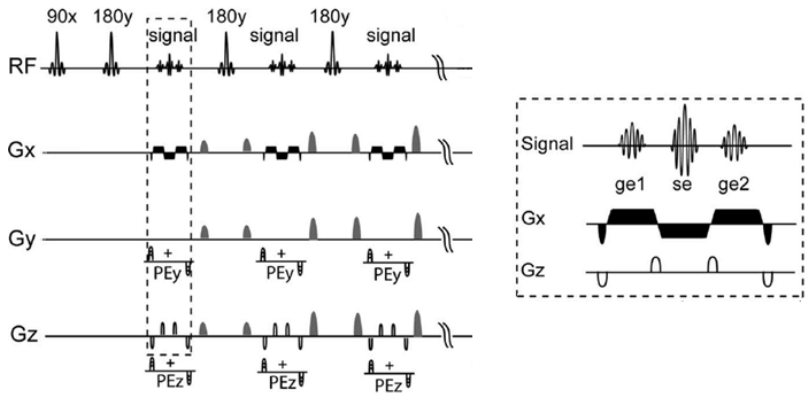

Figure 1.5: Pulse sequence diagram of the 3D GRASE sequence. Gradients Gx, Gy, and Gz are used for the readout, primary, and secondary phase encoding, respectively. Details of the readout scheme used for GRASE acquisition (inside the dashed box) are enlarged and shown on the right (dashed box, right side)

1.2.4 Multi-component Fitting

The first step of fitting for multi-echo data is defining a model that sufficiently describes and predicts the real data. It is assumed that there is a range of T_2 values present in the multi-echo data. Therefore, the general form of the model could be the sum of time-domain functions with their corresponding weights:

$$Y_i = \sum_{j=1}^{M} S_j \times DEC(t_i, T_{2,\mathrm{j}}, \bar{\theta}),\ i = 1, 2, \ldots, n \tag{1.4}$$

Where n is the number of echoes, Y_i represents the echo signal amplitude acquired at time t_i, M is the number of (usually logarithmically spaced) relaxation time in an arbitrary range of T_2 values, S_j is the corresponding weight, $DEC(.)$ is the decay function predicting signal decay associated with each T_2 value, and $\bar{\theta}$ represents all other parameters that affect and determine the shape of the signal decay curve. The simplest form of the model would be multi-exponential decay; in which we would have:

$$DEC(t, T_2, \bar{\theta}) = e^{-t/T_2} \tag{1.5}$$

This simple model requires perfect 180° refocusing pulses. However, in practice, it is hardly possible to achieve perfect refocusing angles, due to through-plane (slice pro-

file) variation, B_1 calibration errors, and RF inhomogeneity (which gets exacerbated at higher field strengths) [1, 9, 25]. Therefore, different voxels across the excited slab would experience a range of refocusing angles that significantly differ from the intended 180°. Imperfect refocusing angles produce alternate echo pathways that contaminate later echoes. This phenomenon is called stimulated echo in literature and introduces T_1 and B_1 effects to the decay curve [1, 25, 26].

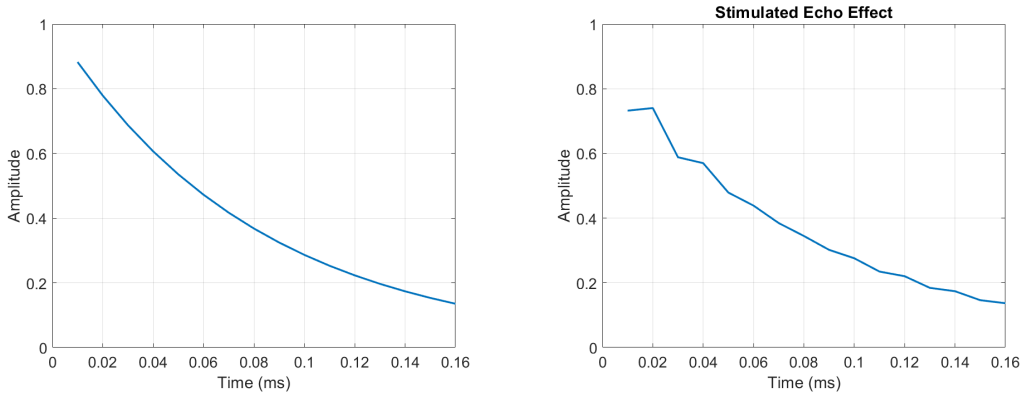

(a) (b)

Figure 1.6: From basic MR principles, we expect T_2 to be observed as (a) exponential decay ($T_2 = 80ms, T_1 = 1000ms$, flip angle = 180°). However, in practice, (b) multi-echo sequences are not observed to have pure exponential decay due to contributions from alternative echo pathways when refocusing pulses are not precisely 180° ($T_2 = 80ms, T_1 = 1000ms$, flip angle = 140°).

1.2.5 Extended Phase Graph (EPG) Algorithm

The $B_1{}^+$ field inhomogeneity effects in multi-echo acquisitions result in signal decays that are contaminated by stimulated echoes. The aftermath is that real data deviate significantly from a "pure" T_2 decay curve. Therefore, in order to have a realistic model, stimulated echoes need to be accounted for. The EPG algorithm [27] has been extensively used for multi-component T_2 fitting procedures and functions by iteratively tracking the phase of several populations of spins as they undergo RF refocusing and exponential relaxation [26].

Total magnetization $\vec{M}$ in each voxel can be described by transverse (M_X, M_Y) and

longitudinal (M_Z) components. Throughout a multi-echo acquisition, $\vec{M}$ is calculated only before and after the application of RF pulses. Computation of the total magnetization using "pure" magnetization M_X, M_Y, and M_Z requires summation over a large number of spin ensembles which is usually deemed not feasible as it requires heavy computations[27]. In order to avoid this in the EPG algorithm, a magnetization phase state vector (MPSV) is defined with three types of phase states or sub-states: F states refer to dephasing spins in the transverse plane, F^* states refer to re-phasing spins in the transverse plane, and Z states refer to spins along the longitudinal axis which retain their phase. Moreover, a subscript is assigned to each state that denotes the number of phase increment steps (equals to one TE period) that each spin population has accrued [26].

$$MPSV = (F_1, F_1^*, Z_1, \ldots, F_N, F_N^*, Z_N)^t \tag{1.6}$$

Where N stands for the number of echoes, superscript t (= transpose) is used for the convenient representation of the column vectors. In order to predict signal decay, it is sufficient to calculate sub-states at each echo time.

It is assumed that before excitation, all spins are along the longitudinal axis with intact phases. After the application of 90° RF excitation, all the spins are moved on to the transverse plane and start dephasing; thus F_1 is set to 1 (normalized value). Now, a series of matrices are employed that account for the effects of RF refocusing, phase transition, and relaxation.

Assuming that refocusing pulses at each echo are identical, rotation matrix $\boldsymbol{R}$ that accounts for RF refocusing is as follows:

$$\begin{bmatrix} F_n^+ \\ F_n^+ \\ Z_n^+ \end{bmatrix} = \begin{bmatrix} \cos^2(\alpha/2) & \sin^2(\alpha/2) & -i\sin(\alpha) \\ \sin^2(\alpha/2) & \cos^2(\alpha/2) & i\sin(\alpha) \\ -0.5i\sin(\alpha) & 0.5i\sin(\alpha) & \cos(\alpha) \end{bmatrix} \begin{bmatrix} F_n \\ F_n^* \\ Z_n \end{bmatrix} \tag{1.7}$$

Where superscript "+" indicates the new values after application of the RF refocusing pulse, α stands for the rotation angle that the magnetization vector experiences.

Between refocusing pulses, spins go through the following transitions:

$$\begin{aligned} F_n &\rightarrow F_{n+1} \\ F_n^* &\rightarrow F_{n-1} \\ F_1^* &\rightarrow F_1 \\ Z_N &\rightarrow Z_N \end{aligned} \tag{1.8}$$

These transitions are defined in matrix $\boldsymbol{T}$ and are similar for each phase increments. An echo is formed when F_1^* transitions to F_1; because the change from rephasing to dephasing necessitates a period of coherence when spins are in phase and are measurable.

The relaxation matrix $\boldsymbol{E}$ quantifies the exponential relaxation for half of the TE period and is defined as:

$$\begin{bmatrix} F_n^+ \\ F_n^+ \\ Z_n^+ \end{bmatrix} = \begin{bmatrix} E_2 & 0 & 0 \\ 0 & E_2 & 0 \\ 0 & 0 & E_1 \end{bmatrix} \begin{bmatrix} F_n \\ F_n^* \\ Z_n \end{bmatrix} \tag{1.9}$$

Where:

$$E_2 = \exp(-\frac{TE}{2T_2}), E_1 = \exp(-\frac{TE}{2T_1}) \tag{1.10}$$

Using the aforementioned matrices, the magnitude of the nth echo M_n can be defined using the following iterative equation:

$$MPSV_n = (\boldsymbol{ETRE})^n MPSV_0 \tag{1.11}$$

$$M_n = MPSV_n(1) \tag{1.12}$$

Where the first part of the right-hand side of Equation (1.11) is the matrix multiplication of relaxation matrix $\boldsymbol{E}$, transition matrix $\boldsymbol{T}$, and the rotation matrix $\boldsymbol{R}$ then multiplied by $\boldsymbol{E}$ again; the entire matrix multiplication is set to the power n which denotes the echo index, where $n = 0$ delineates the state of spins right after excitation

pulse.The value of $MPSV_0$ is set to the normalized value of $[1, 0, 0, ...]^T$.

Using the EPG algorithm, the following model for signal decay can be written:

$$DEC(t, T_2, \bar{\theta}) = EPG(t, T_2, T_1, \alpha) \tag{1.13}$$

Where T_1 is the longitudinal relaxation parameter, which is usually considered a constant value ($= 1s$) for all voxels. Since inter-echo spacing is significantly smaller than T_1 values, one can assume a constant value for the generation of a dictionary matrix for the fitting procedure; and it has been shown that this assumption would result in negligible effects on the final solution [26]. α denotes the refocusing angle of the voxel; this parameter can be supplied by getting a B_1 map or by implementing an inverse problem.

1.2.6 Non-Negative Least squared (NNLS) Curve Fitting Algorithm

The NNLS algorithm was initially introduced by Lawson and Hanson (1974) [28], and later was adopted by Whittall and Mackay (1989) for T_2 decay curve analysis [1]. Thereafter, it has been vastly used in the literature, especially in MWI. In order to use NNLS for T_2 decay analysis, a cost function must be defined:

$$\min_x \|DX - Y\|_2^2 \tag{1.14}$$

Where Y is the observed signal decay, and D is a dictionary matrix containing decay curves based on the model which is assumed for the signal decay. These decay curves have similar parameters and differ only by T_2 relaxation value. The T_2 values used to calculate the decay curves are usually a set of logarithmically spaced values between the smallest predicted T_2 value (which is associated with myelin water) and the longest predicted value (CSF or free water). The vector X is the set of weights associated with T_2 distribution and the final solution to the NNLS algorithm. Using this non-regularized form for the cost function would lead to solutions that are spikes in the T_2 distribution (as in Figure 1.3b).

In most numerical methods treating ill-posed problems, the problem is replaced with a nearby solution that approximates the required solution which is considered more satisfactory. Often this is accomplished by including additional information, *e.g.* the calculated solution should be smooth. Such methods are called regularization and they use a regularization parameter to handle the degree of applied smoothing [29]. This smoothing is to ensure that the final solution would not be too sensitive to perturbation of D or Y; and the solution would be more realistic since tissues are more likely to have a distribution of T_2 components as opposed to delta functions or spikes in the distribution. To apply the regularization cost function would be re-written as below:

$$\min_x \|DX - Y\|_2^2 + \mu\|X|_2^2 \tag{1.15}$$

Where μ is the regularization factor. Commonly, the value of this parameter is determined such that there would be a 2% increase in the sum of squared residual of the fitted curve, compared to the non-regularized solution; which is supposed to deliver the desired level of smoothing [26, 30].

After calculating the T_2 distributions, weights corresponding to shorter T_2 values smaller than a certain threshold (usually $40ms$) are assumed to be originating from myelin water. Therefore, to compute myelin water fraction one must calculate the ratio of the sum of weights smaller than the threshold to the total sum of weights:

$$MWF = \frac{\sum_{T_2=T_{2min}}^{T_2=Threshold} X(T_2)}{\sum X(T_2)} \tag{1.16}$$

1.3 Multi-echo Gradient Recalled Echo

In gradient-echo acquisitions unlike spin-echo acquisitions, there is no refocusing pulses after the excitation pulse. Therefore, the acquired signal at echo time will be affected by mesoscopic field inhomogeneities, which will affect the transverse relaxation [31]. In GRE acquisitions, the effective transverse relaxation is delineated

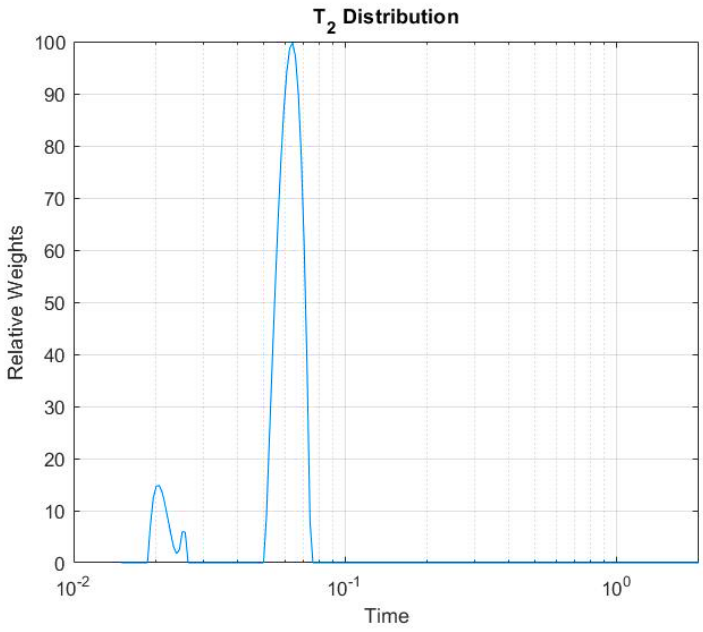

Figure 1.7: Sample T_2 distribution extracted from regularized NNLS solution of in-vivo data. The smaller components ($T_2 < 40\,ms$) are associated with myelin water. The data was acquired from the 3D-GRASE sequence on a Siemens 3T scanner. There are artifacts in the in-vivo data which affect the NNLS solution in different ways, the two little peaks in the MW range is the evidence of that.

by $T_2{}^*$ and is related to T_2 by [31, 32]:

$$\frac{1}{T_2^*} = \frac{1}{T_2} + \frac{1}{T_2'} \tag{1.17}$$

Where T_2' is the determined by mesoscopic field inhomogeneities [31]. As the multi-echo gradient-echo (ME-GRE) acquisition does not need refocusing pulses; it has multiple advantages over MESE: 1) Reduced SAR, which comes in handy at higher field strengths; 2) smaller first echo time (TE_1) and shorter echo-spacing (TE), thus increased number of measurements before myelin signal fades away (although $T_2{}^*$ times are shorter than T_2); 3) Reduced acquisition time and increased volume coverage with the multi-slice 2D acquisition; 4) relatively simple pulse sequence design [4, 5, 32, 33].

The ME-GRE methods come with many challenges and concerns. There are issues that contribute to non-white noise [32], such as respiratory cycle effects which intro-

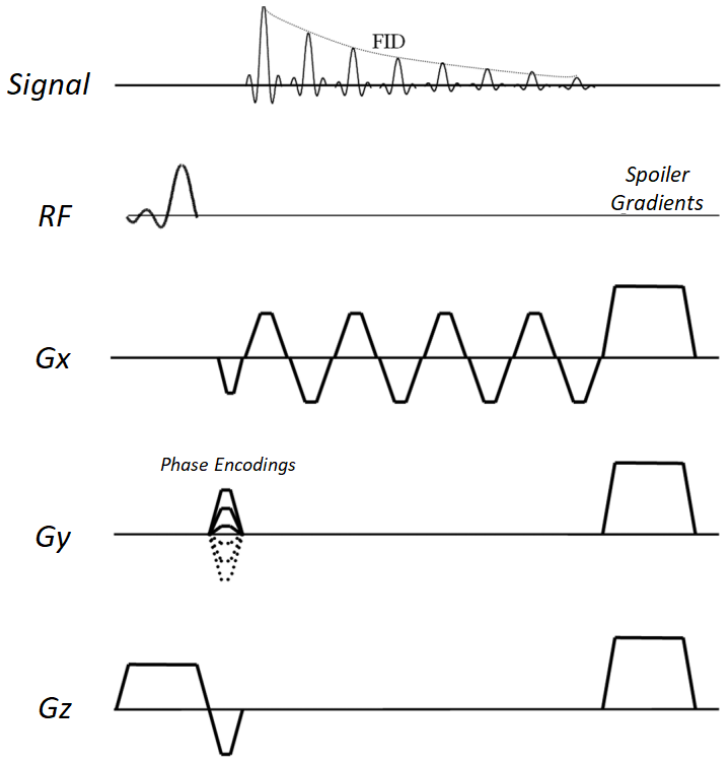

Figure 1.8: The diagram of the ME-GRE pulse sequence with a train of alternating readout gradients (Gx) polarity played out immediately after the phase-encoding (Gy). Only 8 echoes are plotted for simplicity.

duce fluctuations in susceptibility related to the variations in oxygen concentration, low frequency resting-state signal fluctuation observed in the brain [5, 32], and local movements caused by pulsation of nearby arteries [32]. Dominant physiological noises have been reported to increase the noise levels up to three times when comparing in-vivo to in-vitro data [5]. There is also the contribution of B_0 field inhomogeneities that produce local field gradient effects that will introduce non-exponential decay to ME-GRE signals [5, 8, 32, 34]. Sequence parameters can also have notable effects on the outcome of the analysis. For example, using a short repetition time (TR) with a large excitation flip angle would introduce T_1 effects to the proportions of water compartments. Since myelin water is believed to display relatively shorter longitudinal relaxation parameter than the other water-compartments; there would be significant MWF overestimations as myelin water magnetization would recover faster.

The complex exponential functions that are commonly used to describe ME-GRE decays are not orthogonal which makes the ME-GRE data analysis very sensitive to the incorporated models [8].

1.3.1 ME-GRE Signal Modeling

Two different approaches have been adopted to analyze ME-GRE data: 1) regularized NNLS fit for a range of T_2^* values to get a pseudo-continuous distribution (the same process as the MESE data but with different range and threshold) [34], and 2) a multiple-pool model that contains fewer parameters and usually employs a nonlinear least squared (NLLS) method to yield the solution [4, 32, 33]. The latter method was proposed so the distinction of transverse relaxation components would be better defined (to overcome the misclassification of water compartment weights which the regularized NNLS method faces) and introduces the possibility of investigation of water compartments other than myelin water [5, 33]. Here we solely focus on the three-pool model, in which the water compartments are assumed to be myelin water, extra-cellular water, and axonal water [4, 5, 8, 33].

In WM, magnetic susceptibility effects of the distribution of myelin lipids and iron introduce compartment-specific resonance frequency shifts [4]. The frequency shift effects are believed to be dependent on the angle of the WM fiber bundle with respect to the main magnetic field (B_0) [4, 8, 34]. There have also been studies that claim compartment-specific frequency shifts at 3 Tesla are small enough to be ignored [34]. However, in order to have a thorough model, the full complex three pool model equation is written below:

$$S(t) = \{A_{my} \times e^{-t(R^*_{2my}+i2\pi f_{my})} + A_{ax} \times e^{-t(R^*_{2ax}+i2\pi f_a x)} + A_{ex} \times e^{-t(R^*_{2ex}+i2\pi f_{ex})}\} \times e^{-i2\pi f_{bkg} t+\varphi_0} \tag{1.18}$$

Where subscripts my, ax, and ex stand for myelin water, axonal water, and extra-cellular water compartments, respectively. A is the amplitude of each water compart-

ment contributing to the signal decay. R_2^* is the transverse relaxation parameter, and f denotes the compartment-specific frequency shift. The f_{bkg} represents the background frequency of the entire voxel introduced by the mesoscopic magnetic field effect and φ_0 denotes the receiver coil offset.

In order to solve Equation (1.18) an NLLS method with a proper initial guess for each parameter is usually applied. One can ignore the frequency shifts to fit for fewer parameters or only use the magnitude of ME-GRE data to the absolute value of Equation (1.18) for simplicity [4, 33]. More recent papers utilize both magnitude and phase data to fit to Equation (1.18), this incorporation is reported to improve MWF estimation especially where WM bundles are perpendicular to the B_0 field [8]. After fitting the parameters, one can simply calculate MWF by getting the proportion of myelin water:

$$MWF = \frac{A_m}{A_m + A_{ax} + A_{ex}} \tag{1.19}$$

1.3.2 Local Field Inhomogeneity Correction

In practice, the magnetic field inside any system placed into an MRI scanner is always inhomogeneous. The inhomogeneities in the B_0 magnetic field produce local field gradients (LFG), inducing an additional non-exponential decay to the signal [31]. On the premise that there exists a constant linear background gradient G'_x parallel to the read direction, the measured signal can be written as [15]:

$$S(t') = \int dx \rho(x) e^{-i\gamma G_x x t' - i\gamma G'_x x (t' + T_E)} = \int dx \rho(x) e^{-i\gamma G_x x t' (1 + G'_x/G_x) - i\gamma G'_x x T_E} \tag{1.20}$$

The first part of the phase term is a scaling factor of the k-space variable which produces distortion (when $G'_x << G_x$ this term can be ignored) and the other phase term is a position-dependent term that is linearly related to echo time:

$$\Phi(x) = -\gamma G'_x x T_E \tag{1.21}$$

The phase difference over a distance d can be written as:

$$\Delta\Phi = -\gamma G'_x d T_E \tag{1.22}$$

Assuming that each voxel contains a homogeneous distribution of spins, the phase difference across the voxel leads to dephasing of the total signal. This dephased signal is given by [15]:

$$\hat{\rho} = \rho_0 \left[\frac{1}{\Delta\Phi} \int_{-\Delta\Phi/2}^{+\Delta\Phi/2} e^{i\Phi} d\Phi \right] = \rho_0 \, sinc(\Delta\Phi/2) \tag{1.23}$$

To compensate for the LFG effects, usually a preparation (prior to the NLLS process) step is implemented to estimate the local gradients in each direction and then the "sinc" function correction is applied. There have been studies that include the "sinc" function in the signal decay model and fit for the LFG as an extra parameter [35].

1.4 Sequence Optimization

1.4.1 3D-GRASE Optimization

Echo Shifting Method

Compared to EPI imaging, GRASE images manifest much fewer chemical shift effects and image distortions caused by field inhomogeneities. Such manifestation of effects is inversely proportional to the number of Hahn spin echoes in the echo train. In a GRASE sequence, the CPMG sequence is performed with refocusing RF pulses interlaced with a number of gradient-echo trains (N_{GE}). The CPMG sequence part from that of the EPI sequence significantly reduces the evolution of the phase errors due to field inhomogeneity. The remaining small phase errors re-appear periodically in the gradient-echo train. If this periodicity is not removed from k-space data, the convolution of the periodic error function with object data results in destructive replication artifacts in the frequency domain image. One can impose a periodic order to temporal acquisition of successive data in order to deal with the discontinuity in the phase function. This necessitates shifting the acquisition times in order to deal

with the discontinuities in the phase due to the small phase errors [36].

GRASE images of the human brain appear artifact free. However, body images show artifactual bands of signal parallel to lipid and water interfaces. This is associated with mentioned phase discontinuities in the k-space [36].

Below is the description of how to incrementally change the temporal position of echo-train with respect to Hahn echo time in the CPMG sequence, to eliminate the discontinuities of phase in k-space due to field inhomogeneities. Such echo shifts permit continuous sampling of phase errors.

The NMR signal can be described as below:

$$S(t) = \int\int M(r) exp[-j(k(t) \cdot r + \gamma E(r)t] dr \tag{1.24}$$

$$k(t) = \gamma \int_0^t G(t')dt' \tag{1.25}$$

Where $M(.)$ is the magnetization and $G(.)$ is the magnetic field gradient at the position r. $E(.)$ denotes the field component due to inhomogeneities including chemical shift and static field.

In the sequence at our local site, we did not have the capability to access and manipulate the source code, thus we performed an experiment where we put a probe inside the scanner and watched the trace on the oscilloscope screen (Figure 1.9). Usually in order to accommodate for the delay in the readout gradient the ΔTE (echo spacing) is increased [37], however in the acquired sequence an alternate scheme was procured. They keep the timing of the first two pulses (excitation and first refocusing pulse) constant and gradually increase the echo-spacing to perform the echo-shifting scheme. Based on our observation the echo spacing in the scheme differs from $10ms$ to $11.8ms$ for different k-space lines.

This creative solution has not been fully analyzed due to its complexity. However, Piredda *et al.* released a supplementary document (along with their 2020 paper)

Figure 1.9: Probed echo train using the Siemens scanner and the Korean 3D GRASE. The time difference of the first two pulses is 5 ms and first center k-space readout happens 10.68 ms after the excitation pulse.

that exhibits the results of exploring the classic solution where echo spacing remains constant throughout the sequence [37]. They stated that their results showed no discernible differences in magnitude images using the echo shifting method in the brain, but using the larger echo spacing resulted in the overestimation of MWF values. Looking at their MWF maps in the supplementary document, one could see the MWF overestimation when comparing the 10.7 ms echo spacing results to 11.8 ms, however, if you look closely at the frontal regions (frontal WM) of the maps you can see qualitatively better-looking WM tracks and MWF contrast in the brain, thus in can be assumed that there are visible benefits to the echo-shifting method even in the brain; especially, the ringing artifact pointed out by the authors.

Slice Over-sampling

We usually acquire 32 slices in our experiments using the 3D GRASE sequence, where some slices on either side (scanning the center region of the brain) contain significant aliasing artifacts. The aliasing artifact has strong effects on the multi-component

analysis. This is due to the fact that the MW signal makes up such a small portion of the signal that even if aliasing is not visible in the magnitude images its effects can be easily observed in the final MWF maps. One could set FOV such that a few slices on one side include air, therefore only one side would contain this artifact. The other solution is to apply slice oversampling method where we excite the same slab size but acquire data for a few extra slices on each side (which extra slices will be thrown away). Basically, the slab that the data is acquired from would be larger than the excited (intended) slab.

We tried to optimize the slice-oversampling factor with the underlying assumption that the acquisition time must remain constant. The results showed when using the factor of 33% for oversampling we would achieve the maximum number of unaliased slices. However, there was a downside to using this method; in order to keep the acquisition time constant, the size of the slab which data were acquired from, was supposed to remain fixed as well. Therefore, increasing oversampling meant we should decrease the excited slab size hence decreasing the overall available signal for acquisition. Thus it resulted in a loss of SNR. Moreover, the number of extra unaliased slices were small (2 extra slices), and due to the loss of SNR was deemed undesirable and the sequence parameters was left as it was.

1.4.2 ME-GRE Optimization

Gradient Polarity

In ME-GRE sequences using the bipolar readout scheme allows shorter echo-spacing compared to the monopolar option. Shorter echo-spacing grants the ability to capture more echoes containing MW signal (*i.e.* better temporal resolution of the signal decay). However, using the bipolar scheme introduces phase and magnitude modulation (on odd and even echoes) based on the polarity of the readout [35]. Shin *et al.* (2019) introduced the gradient pairing method to tackle this issue by getting two short term averages where in the second average all the gradient polarities are reversed; and then

the final image was calculated by the vector sum of the two images. Their results showed significant improvements in the MWI analysis results.

We tried to implement the same sequence scheme in the Siemens 3T scanner. Alas, we could not replicate the same data and this project was left aside; Images from the two averages required registrations, and also there no settings in the IDEA sequence programing platform to let the scanner know we are using the reverse polarity, thus there was even a shift in the k-space as it was saved backward by the scanner.

Nerve Stimulation

Short echo-spacing translates into fast gradient alternating during the scan, which usually will be flagged by the scanner and requires you to apply certain changes in order to prevent the subject from twitching during the scan (prevent nerve stimulations). Scanner usually asks for increasing the echo-spacing and changing the BW, but we tried to resolve this issue by changing the FOV or the resolution of the acquisition. Increasing the FOV seems the best way to go as it increases voxel size, thus increasing SNR.

1.5 Thesis Outline

This thesis focuses on multi-component transverse analysis in order to perform MWI analysis. Both T_2 and T_2^* based methods are explored and the common methods in the literature are used for comparison. All experiments are performed at 3T Siemens Prisma.

First, we try to constrain the flip angle parameter in the fitting process using the 3D GRASE data. The goal in mind is to supply a parameter using a reliable independent sequence in order to improve the analysis and decrease the variability of results.

Second, Bloch equations will be used to simulate and generate decay curves of the 2D MESE sequence, in order to enable the same multi-component analysis used for 3D data. Then using the same principles, we try to supply B_1^+ to investigate the effects

on the fitting results.

Finally, we try to replicate the typical techniques (regularized NNLS method and three-pool model) used for ME-GRE methods to attain MWF maps, then investigate the noise and modeling effects facing ME-GRE data analysis. To tackle the SNR issues of the ME-GRE method, we investigated the effects of non-local filtering on the MWF maps.

References

[1] S. H. Kolind, "Myelin Water Imaging: Development at 3.0 t, application to the study of multiple sclerosis, and comparison to diffusion tensor imaging," Ph.D. dissertation, University of British Colombia, 2008.

[2] M. Simons and K.-A. Nave, "Oligodendrocytes: Myelination and axonal support," *Cold Spring Harbor perspectives in biology*, vol. 8, no. 1:a020479, 2015. DOI: 10.1101/cshperspect.a020479.

[3] D. K. Hartline, "What is myelin?" *Neuron Glia Biology*, vol. 4, no. 2, 153–163, 2008. DOI: 10.1017/S1740925X09990263.

[4] P. van Gelderen, J. A. de Zwart, J. Lee, P. Sati, D. S. Reich, and J. H. Duyn, "Nonexponential t2* decay in white matter," *Magnetic Resonance in Medicine*, vol. 67, no. 1, pp. 110–117, 2012. DOI: 10.1002/mrm.22990.

[5] E. Alonso-Ortiz, I. R. Levesque, and G. B. Pike, "Mri-based myelin water imaging: A technical review," *Magnetic Resonance in Medicine*, vol. 73, no. 1, pp. 70–81, 2015. DOI: 10.1002/mrm.25198.

[6] C. Raine, *Morphology of Myelin and Myelination*. In: Morell P., editor. Myelin. 2nd Edition ed. New York: Plenum Press, 1984.

[7] C Laule, E Leung, D. K. Li, A. L. Traboulsee, D. W. Paty, A. L. MacKay, and G. R. Moore, "Myelin water imaging in multiple sclerosis: Quantitative correlations with histopathology," *Multiple Sclerosis Journal*, vol. 12, no. 6, pp. 747–753, 2006, PMID: 17263002. DOI: 10.1177/1352458506070928.

[8] J. Lee, J.-W. Hyun, J. Lee, E.-J. Choi, H.-G. Shin, K. Min, Y. Nam, H. J. Kim, and S.-H. Oh, "So you want to image myelin using mri: An overview and practical guide for myelin water imaging," *Journal of Magnetic Resonance Imaging, Online ahead of print.*, vol. n/a, no. n/a, 2020 Feb 3. DOI: 10.1002/jmri.27059.

[9] M. D. Does, "Inferring brain tissue composition and microstructure via mr relaxometry," *NeuroImage*, vol. 182, pp. 136 –148, 2018, Microstructural Imaging, ISSN: 1053-8119. DOI: 10.1016/j.neuroimage.2017.12.087.

[10] D. Kumar, S. Siemonsen, C. Heesen, J. Fiehler, and J. Sedlacik, "Noise robust spatially regularized myelin water fraction mapping with the intrinsic b1-error correction based on the linearized version of the extended phase graph model," *Journal of Magnetic Resonance Imaging*, vol. 43, no. 4, pp. 800–817, 2016. DOI: 10.1002/jmri.25078.

[11] D. J. Griffiths, *Introduction to Quantum Mechanics*. Upper Saddle River, NJ, 2 edition: Pearson, 2004.

[12] D. G. Nishimura, *Principles of Magnetic Resonance Imaging*. Stanford Univ,1.1 edition, 2010.

[13] J. C. Gore and R. Kennan, *Physical and Physiological Basis of Magnetic Relaxation*. In Magnetic Resonance Imaging. Mosby, 1999, ch. 3.

[14] K. C. McPhee, "Relaxometry in the Human Brain Using High Field MRI," Ph.D. dissertation, University of Alberta, 2017.

[15] E. M. Haacke, R. W. Brown, M. R. Thompson, and R. Venkatesan, *Magnetic Resonance Imaging: Physical Principles and Sequence Design*. Wiley-Liss, 1st edition, 1999.

[16] M. T. Vlaardingerbroek and J. A. d. Boer, *Magnetic Resonance Imaging*. Google-Books-ID: n3e0QgAACAAJ: Springer, 2nd edition, 1999.

[17] V Vasilescu, E Katona, V Simplăceanu, and D. Demco, "Water compartments in the myelinated nerve. iii. pulsed nmr results.," *Experientia*, vol. 34, no. 11, pp. 1443–1444, 1978. DOI: 10.1007/BF01932339.

[18] R. S. Menon and P. S. Allen, "Application of continuous relaxation time distributions to the fitting of data from model systems and excised tissue," *Magnetic Resonance in Medicine*, vol. 20, no. 2, pp. 214–227, 1991. DOI: 10.1002/mrm.1910200205.

[19] A. Mackay, K. Whittall, J. Adler, D. Li, D. Paty, and D. Graeb, "In vivo visualization of myelin water in brain by magnetic resonance," *Magnetic Resonance in Medicine*, vol. 31, no. 6, pp. 673–677, 1994. DOI: 10.1002/mrm.1910310614.

[20] C. Beaulieu, F. R. Fenrich, and P. S. Allen, "Multicomponent water proton transverse relaxation and t2-discriminated water diffusion in myelinated and nonmyelinated nerve," *Magnetic Resonance Imaging*, vol. 16, no. 10, pp. 1201 –1210, 1998, ISSN: 0730-725X. DOI: 10.1016/S0730-725X(98)00151-9.

[21] S. Webb, C. A. Munro, R. Midha, and G. J. Stanisz, "Is multicomponent t2 a good measure of myelin content in peripheral nerve?" *Magnetic Resonance in Medicine*, vol. 49, no. 4, pp. 638–645, 2003. DOI: 10.1002/mrm.10411.

[22] C. Laule, P. Kozlowski, E. Leung, D. K. Li, A. L. MacKay, and G. W. Moore, "Myelin water imaging of multiple sclerosis at 7 t: Correlations with histopathology," *NeuroImage*, vol. 40, no. 4, pp. 1575 –1580, 2008, ISSN: 1053-8119. DOI: 10.1016/j.neuroimage.2007.12.008.

[23] K. P. Whittall, A. L. Mackay, D. A. Graeb, R. A. Nugent, D. K. B. Li, and D. W. Paty, "In vivo measurement of t2 distributions and water contents in normal human brain," *Magnetic Resonance in Medicine*, vol. 37, no. 1, pp. 34–43, 1997. DOI: 10.1002/mrm.1910370107.

[24] T. Prasloski, A. Rauscher, A. L. MacKay, M. Hodgson, I. M. Vavasour, C. Laule, and B. Mädler, "Rapid whole cerebrum myelin water imaging using a 3d grase sequence," *NeuroImage*, vol. 63, no. 1, pp. 533 –539, 2012, ISSN: 1053-8119. DOI: 10.1016/j.neuroimage.2012.06.064.

[25] R. M. Lebel and A. H. Wilman, "Transverse relaxometry with stimulated echo compensation," *Magnetic Resonance in Medicine*, vol. 64, no. 4, pp. 1005–1014, 2010. DOI: 10.1002/mrm.22487.

[26] T. Prasloski, B. Mädler, Q.-S. Xiang, A. MacKay, and C. Jones, "Applications of stimulated echo correction to multicomponent t2 analysis," *Magnetic Resonance in Medicine*, vol. 67, no. 6, pp. 1803–1814, 2012. DOI: 10.1002/mrm.23157.

[27] J. Hennig, "Echoes—how to generate, recognize, use or avoid them in mr-imaging sequences. part i: Fundamental and not so fundamental properties of spin echoes," *Concepts in Magnetic Resonance*, vol. 3, no. 3, pp. 125–143, 1991. DOI: 10.1002/cmr.1820030302.

[28] C. L. Lawson and R. J. Hanson, *Solving least squares problems*. IEnglewood Cliffs, NJ: Prentice-Hall, 1974.

[29] P. C. Hansen, "Analysis of discrete ill-posed problems by means of the l-curve," *SIAM Review*, vol. 34, no. 4, pp. 561–580, 1992. DOI: 10.1137/1034115.

[30] V. Wiggermann, I. M. Vavasour, S. Kolind, A. L. MacKay, G. Helms, and A. Rauscher, "Non-negative least squares computation for in vivo myelin mapping using simulated multi-echo spin-echo t2 decay data," *NMR in Biomedicine*, vol. 33, no. 12, e4277, 2020.

[31] D. A. Yablonskiy, "Quantitation of intrinsic magnetic susceptibility-related effects in a tissue matrix. phantom study," *Magnetic Resonance in Medicine*, vol. 39, no. 3, pp. 417–428, 1998. DOI: 10.1002/mrm.1910390312.

[32] D. Hwang, D.-H. Kim, and Y. P. Du, "In vivo multi-slice mapping of myelin water content using t2* decay," *NeuroImage*, vol. 52, no. 1, pp. 198 –204, 2010, ISSN: 1053-8119. DOI: 10.1016/j.neuroimage.2010.04.023.

[33] Y. P. Du, R. Chu, D. Hwang, M. S. Brown, B. K. Kleinschmidt-DeMasters, D. Singel, and J. H. Simon, "Fast multislice mapping of the myelin water fraction using multicompartment analysis of t decay at 3t: A preliminary postmortem study," *Magnetic Resonance in Medicine*, vol. 58, no. 5, pp. 865–870, 2007. DOI: 10.1002/mrm.21409.

[34] E. Alonso-Ortiz, I. R. Levesque, and G. B. Pike, "Multi-gradient-echo myelin water fraction imaging: Comparison to the multi-echo-spin-echo technique," *Magnetic Resonance in Medicine*, vol. 79, no. 3, pp. 1439–1446, 2018. DOI: 10.1002/mrm.26809.

[35] H.-G. Shin, S.-H. Oh, M. Fukunaga, Y. Nam, D. Lee, W. Jung, M. Jo, S. Ji, J. Y. Choi, and J. Lee, "Advances in gradient echo myelin water imaging at 3t and 7t," *NeuroImage*, vol. 188, pp. 835 –844, 2019, ISSN: 1053-8119. DOI: 10.1016/j.neuroimage.2018.11.040.

[36] D. A. Feinberg and K. Oshio, "Gradient-echo shifting in fast mri techniques (erase imaging) for correction of field inhomogeneity errors and chemical shift," *Journal of Magnetic Resonance (1969)*, vol. 97, no. 1, pp. 177–183, 1992.

[37] G. F. Piredda, T. Hilbert, E. J. Canales-Rodríguez, M. Pizzolato, C. von Deuster, R. Meuli, J. Pfeuffer, A. Daducci, J.-P. Thiran, and T. Kober, "Fast and high-resolution myelin water imaging: Accelerating multi-echo grase with caipirinha," *Magnetic Resonance in Medicine*, vol. 85, no. 1, pp. 209–222, 2021.

Chapter 2

Three-Dimensional Myelin Water Fraction Mapping with Independent Flip Angle Map

2.1 Introduction

Transverse relaxation (T_2) mapping is commonly performed with a multiple spin-echo technique, though other methods are possible. As shown by MacKay [19], multiple component analysis of the transverse decay in the in-vivo brain can yield the myelin water fraction (MWF), identified as the short T_2 component. Myelin water is defined as water trapped between myelin bilayers and constitutes roughly one-sixth of the human brain white matter water reservoir [19]. MWF has been shown to correlate with histochemical myelin stains in the postmortem brain [7, 22, 38]. The use of this method is now widespread in research studies of the brain and spinal cord and has particular application to multiple sclerosis, a demyelinating disease [7, 22, 38, 39]. Spectrum analysis of the T_2 decay data gives an understanding of underlying water compartments, including myelin water and intra/extra-cellular water [8, 9, 18, 19, 23, 40, 41]. The discrimination of the myelin water component increases the specificity of T_2 mapping to myelin changes, although there may be other short T_2 species that serve as a confound [42, 43]. Multi-echo spin echo (MESE) data are acquired using an excitation pulse followed by a train of refocusing pulses. Perfect 180° refocusing is

required to generate an exclusively T_2 modulated signal decay. In practice, the theoretical refocusing stipulation is violated due to: imperfect refocusing profiles, transmit calibration errors, and RF interference effects [44], which all collude to alter the range of refocusing angles across the volume of interest [25]. Hence, MESE decay curves are considerably affected by the refocusing angles, therefore mono- or multi-exponential fittings of the corresponding T_2 times need to account for such effects [25, 26, 45].

Modeling of the MESE signal decay may be performed in many different ways including using the extended phase graph (EPG) algorithm [27, 46], which computes multi-echo signal decay curves given T_1, T_2, inter-echo spacing time, and the corresponding refocusing angle. For slice selective RF pulses, the analysis is more complex and requires the accounting of RF slice profile effects [9, 25, 47]. However, the current trend is to perform MWF imaging in the brain using a 3D sequence with nonselective pulses, which enables a simplified accounting of RF pulse effects. While 3D acquisitions avoid incidental magnetization transfer found in 2D methods, 3D scans generally have long acquisition times. By adding gradient echoes within each inter-echo spacing, it is possible to collect two gradient echoes and one spin-echo within each inter-echo time, enabling substantial time savings. This 3D GRASE approach is often used [8, 10, 24, 26, 30, 48], and has been validated in multi-site multi-vendor tests [49], and is the method used in this work.

Recent literature performs T_2 analysis of 3D GRASE for MWF, including stimulated echo compensation, using a multi-exponential fit adopting a regularized Non-Negative Least Squares (NNLS) algorithm to decompose decay curves into T_2 distributions with no prior assumption about the number of contributing T_2 components [10, 24, 26, 30, 39, 48]. The NNLS method assumes a range of T_2 values to create a dictionary matrix based on a model which determines the best fit for the underlying decay curve of each voxel which requires correct refocusing angles. Therefore, to produce proper dictionary matrices for the NNLS process, it is common practice to perform a flip angle optimization step to estimate the corresponding refocusing angle [10, 24,

26, 30, 42, 48]. However, estimation of the flip angle from the decay train is complicated by the oscillating behavior of stimulated echoes and noise and could lead to increased susceptibility of NNLS fit results to noise [10, 30, 48, 50]. There are two possible concerns using this flip angle optimization. First, the assumption that the non-regularized NNLS solution of actual flip angle would result in the smallest χ^2 value is not always true, since alternate refocusing flip angles could generate solutions that fit the noisy signal rather than the ground truth. This assumption would induce extra susceptibility of the final solution to noise. A second issue is the boundary effect since the EPG algorithm is symmetrical around 180° (i.e. 190° is the same as 170°). With the upper limit at 180°, this contributes to further underestimation when true flip angles are close to this boundary [30].

To overcome these potential concerns, we investigated whether supplying true flip angle values to the NNLS process would increase the precision of MWF estimations. This approach eliminates the extra optimization step but requires a flip angle map which has proven successful for single component T_2 mapping [51], and theoretically analyzed to have a significant effect for the case of low SNR data [50], by reducing the number of unknowns in the fitting process. We investigate the value of this approach for MWF in simulations and in-vivo human brain experiments.

2.2 Methods and Procedure

2.2.1 Simulation of T_2 Decay Data

Visible water compartments in the brain water pool could be categorized into three environments: myelin water (MW), intra-extra cellular water (IEW), and cerebrospinal fluid [18, 19, 23, 40, 41, 52]. Each of these environments shows different relaxation characteristics. Based on previous analyses on T_2 relaxometry of in-vivo data [10, 24, 26, 30, 48, 52, 53], we defined a model for simulations, which only consists of MW ($T_2 =\sim 5$ to $\sim 25ms, T_1 =\sim 500ms$) and IEW ($T_2 =\sim 60$ to $\sim 80ms, T_1 =\sim 1000ms$)

environments [8, 30, 38, 54, 55], corresponding to healthy WM tissue [8]. Using this model, simulated T_2 decay could be composed as:

$$S(t) = M_0 \sum_{j=1}^{n} \int D_j(T_2) \cdot EPG(T_2, \bar{\theta}) dT_2 + \epsilon(0, \sigma_n) \tag{2.1}$$

Where $S(t)$ is signal amplitude; M_0 represents the initial value (value at TE = 0) which is equal to the assumed proton density; D_j denotes the piecewise continuous distribution associated with each water compartment and j is the water compartment index. In our model, T_2 distributions for each water compartment are generated using a truncated Gaussian distribution with a standard deviation of 10% of the mean and were truncated to zero for values farther than 2 standard deviations from the mean [53]. $EPG(.)$ is the output of the extended phase graph algorithm, and $\bar{\theta}$ stands for all other required parameters. The $\epsilon(0, \sigma_n)$ function indicates the additive white Gaussian noise – we used Gaussian instead of Rician distribution as our assumed SNRs (at least for early echoes) were large enough that Rician would estimate a Gaussian distribution [30, 48, 56]. We used the SNR definition of [53]:

$$SNR = \frac{S(0)}{\sigma_n} = \frac{M_0}{\sigma_n} \tag{2.2}$$

In order to realize the Gaussian noise. We used M_0 instead of signal amplitude at $TE = 10ms$ since when assuming flip angles smaller than 180 degrees, the amplitude of the first echo is significantly smaller. All the simulations were analogous to the in-vivo 32 echo 3D GRASE/MESE sequence with $TE = \Delta TE = 10ms$.

2.2.2 Analysis and T2 Distribution Process

All data (simulation and in-vivo data) were analyzed on a voxel-wise approach using the regularized NNLS algorithm with stimulated echo estimation (https://mriresearch.med.ubc.ca/news-projects/myelin-water-fraction/). This method uses the standard

model for T_2 analyses [10, 24, 26, 30, 48, 52], which does not make any underlying assumptions about the distribution of signal decay [24, 26, 30, 52]:

$$y_i = \sum_{j=1}^{nT_2} S_j \times EPG(t, T_2, T_1, \alpha), i = 1, 2, ..., n \tag{2.3}$$

Where n is the number of echoes, y_i represents the echo signal amplitude acquired at time t_i and nT_2 is the number of logarithmically spaced T_2 values. Here we assumed $nT_2 = 60$ as further increasing this value would have negligible effects on the final distribution [30], and also raises computation time. The T_2 range was chosen to be from $8ms$ to $2s$ – we chose $T_{2\text{min}}$ (lower limit of the T_2 range) to be slightly smaller than echo-spacing to best capture the MW peak [30]. S_j is the corresponding weight in the distribution, and $EPG(.)$ denotes the predicted signal decay based on the EPG algorithm. In the fitting procedure a constant T_1 value ($= 1s$) is used for all decay curves and voxels since it has been shown to have negligible error [26]. The "α" parameter is the refocusing flip angle experienced by the voxel. This parameter needs to be set or estimated to calculate the final distribution. As per common practice, a regularization term was added, so that there would be about 2% increase in the sum of squared residual of the fitted curve, compared to the non-regularized solution; which would result in the desired level of smoothing and produce a relatively more stable solution [30, 39, 48]. Finally, after acquiring the solution, myelin water fraction is determined by applying a threshold (here we used $40ms$) on the T_2 distribution maps [9, 18, 19, 23, 26, 30]:

$$MWF = \frac{\sum_{T_{2min}=8ms}^{T_2=40ms} X(T_2)}{\Sigma X(T_2)} \tag{2.4}$$

Where $X(.)$ denotes the weights corresponding to each T2 in the predefined distribution.

2.2.3 Flip Angle Estimation

Typically, a number of linearly spaced flip angles – usually 8 flip angles ranging from 100° to 180° [26, 30]– is assumed in order to acquire non-regularized NNLS solutions. Then by back projecting the solution and comparing it to the experimental decay curve, the sum of squares measure of residuals or χ^2 is computed. Finally, χ^2 values versus flip angles are fed to a cubic spline function to interpolate the 8 data point curve. The assumption is that the true flip angle would produce the smallest χ^2, thus by calculating the flip angle that corresponds to minimum χ^2, we have our estimate to use for generating the basis decay curves for the NNLS process [10, 24, 26, 30, 48, 52].

2.2.4 Numerical Simulations

The effect of miscalculation of refocusing angle over the range 110° to 180° was considered by varying the error in the fitted refocusing angle from -20° to 20° in 0.5° steps. The procedure at each flip angle was repeated 500 times with the aforementioned simulation relaxation parameters to calculate the mean of MWF estimations. An ideal SNR of 10000 was used, then repeated with low SNR of 100. The fractions for water compartments were 85% IE, and 15% MW. The mean MWF estimation versus flip angle difference from ground truth was examined. For comparison of the estimated flip angle method to the proposed method, we generated experimental decay curves for flip angles ranging from 110° to 180°. For each flip angle, different SNR values of 50, 100, 200, 300, 500, 750, 1000 were applied to add 5000 realizations of white Gaussian noise to decay curves.

The precision of estimated MWF values was evaluated by comparing the ratio of standard deviations of MWF estimations. This ratio is investigated for MWF of 15%, as it is frequently reported in normal appearing WM [24, 48, 57, 58], and also for the case of MWF = 0 % as a representative of non-myelinated voxels.

2.2.5 In-vivo Experiments

Human brain data were acquired from eight healthy volunteers (2 females and 6 males, 22-42 years old) at 3 T Siemens Prisma (Siemens Healthcare, Erlangen, Germany) using a 64-channel head coil. A three-dimensional (3D) 32 echo GRASE sequence was used for T_2 measurement ($TE/\Delta TE/TR = 10/10/1000ms$, 32 slices with in-plane resolution of $1.5 \times 1.5mm$, $slicethickness = 5mm$, 5/8ths partial Fourier, and acquisition time 13 minutes and 23 seconds). A 3D T_1 weighted MPRAGE sequence was collected for region segmentation (1 mm isotropic resolution, 3.6 min). A Bloch-Siegert flip angle mapping sequence [59], was employed using spatial resolution $1.25 \times 1.25 \times 3.0mm^3$ and 37 seconds acquisition time. Images were registered using the SPM12 MATLAB toolbox.

Images were analyzed to produce MWF maps using the aforementioned processes. Comparisons were made between the standard approach using an estimated flip angle from the echo train, and a supplied flip angle map, using both flip angles and MWF maps were compared. Region-of-interest (ROI) measures were performed in three WM areas (genu, splenium, and forceps major) and two deep gray matter territories (putamen, caudate) using central unaliased slices from the 3D acquisition. ROI values were compared using the ratio of the inter-subject standard deviation of mean MWF. An F-test was used to reject the null hypothesis of equal standard deviation.

2.3 Results

2.3.1 Effect of Flip Angle Difference on MWF Estimation

For illustration purposes, in Figure 2.1 the signal decay is examined using 15% MWF with SNR of 200 and 100 and refocusing angle of 150°. Four decays are plotted: ground truth (zero noise), signal with noise, and fitted curves from the two approaches. Differences can be observed in the first few echoes, while fitted curves converge in later echoes which are not shown. When using the estimated flip angle

method, the fitted curve is closer to the pattern of the signal, which is affected by noise. However, the pattern of the fitted curve using the supplied flip angle is closer to the ground truth rather than to the signal itself. In the two anecdotal cases shown in Figure 2.1, the estimated flip angle method over-fits the solution to the noisy signal by mis-estimating the flip angle of the signal decay (147.4° in Figure 2.1.A and 144.9° in Figure 2.1.B) which in both cases results in further mis-estimations of MWF.

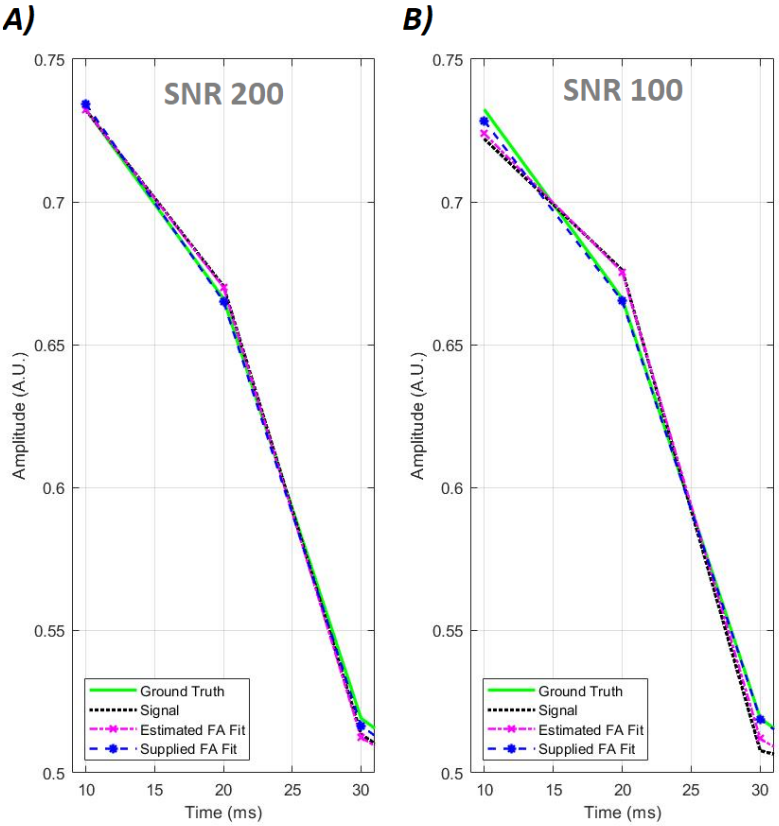

Figure 2.1: Two anecdotal simulated signal decay and the fitted decay curve results for SNR of 200 (A) and 100 (B), flip angle of 150°, and MWF of 15%. The first 3 echoes of the 32 echo signal decay are depicted to show expanded details. The ground truth signal is without noise. A) The fitted curve is the result of the estimated flip angle of 147.4° which estimates an MWF of 17.43% after the NNLS process. And the supplied flip angle fitted curve produced an MWF of 15.89%. B) The fitted curve is the result of estimated flip angle of 144.9° which estimates an MWF of 18.73% after the NNLS process. And the supplied flip angle fitted curve produced an MWF of 17.95%.

Figure 2.2 shows the relationship between MWF and flip angle difference, for an

ideal and low SNR with similar patterns for both, although different offsets. Generally, for flip angles less than 180°, over-estimation of flip angle results in under-estimation of MWF and vice versa. Smaller flip angles are more affected by flip angle errors. Note that for the true flip angle, there is a slight underestimation of MWF particularly for the case of SNR = 100 which could be considered as inherent in the nature of the fitting procedure, as it is shown in previous studies [48]. The slope of the pattern of MWF underestimation seems to be dependent on SNR levels and amplifies as the noise level elevates.

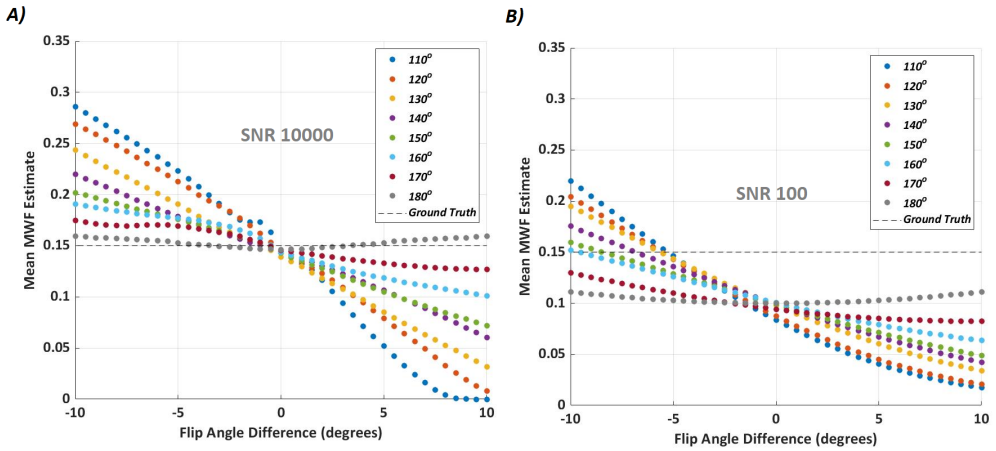

Figure 2.2: Simulation of the flip angle difference effects on NNLS fitting results for a range of flip angles (110° to 180°). Results are symmetric around 180°, so larger values are not shown. SNR value used for simulation was a) an ideal SNR of 10000 and b) a low SNR of 100.

Figure 2.3 illustrates the effect on the T2 spectrum of using a slightly larger flip angle than the ground truth for fitting. It shows a pattern of shifted shorter T2 weights towards larger T2 values, while the IE T2 peak does not shift. The short T2 shift is clearer at smaller flip angles (Figure 2.3.A) and reduces as angles rise (Figure 2.3.B, C) in alignment with Figure 2.2. All solutions are wider and smoother than the ground truth due to regularization.

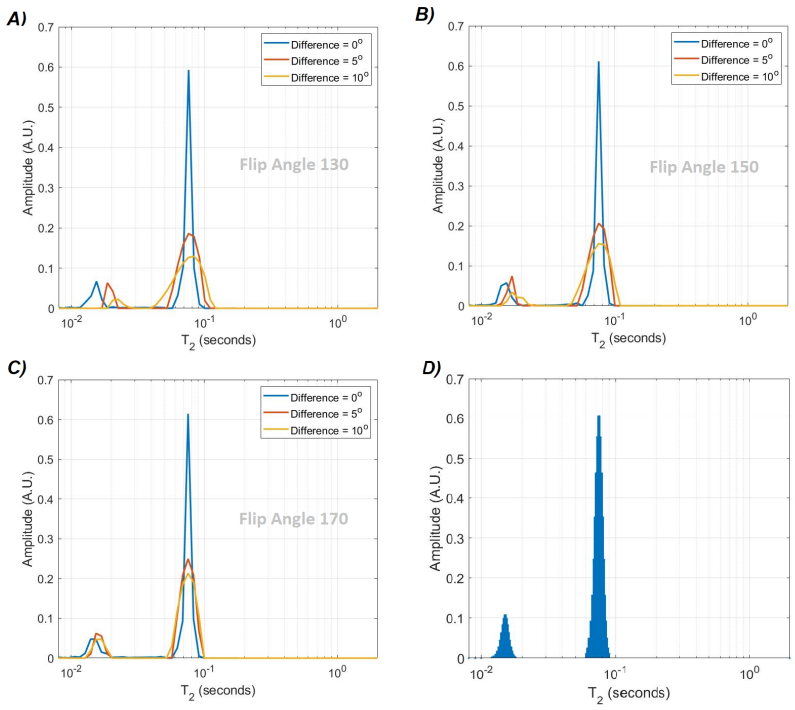

Figure 2.3: T_2 distribution results of the NNLS process for flip angles of A) 130°, B) 150°, C) 170° with MWF of 15% using the distribution in (D) to simulated the decay curves. Fixed T2 values were used for the simulations (MW T2 15ms, IEW T2 75ms) and 500 different realizations of noise with SNR of 10000 was added to the decay curve, in order to get a meaningful average final solution. Three different flip angle difference error values were shown to give a better understanding of NNLS fit when there is an overestimation of the flip angle parameter and to observe the solution when it significantly underestimates MWF.

2.3.2 Flip Angle Estimation

Figure 2.4.A, B show that the mean error of the flip angle estimation is fairly small for flip angles less than 165°, and the estimation mean seem to deviate significantly from the ground truth when it reaches the upper boundary. A positive bias of flip angle estimation can be observed for values over 165°, which then drops down reaching 180° as estimation values cannot exceed the upper boundary. Therefore, flip angle estimates at the upper boundary are either true or underestimated. Standard deviations of flip angle estimate seem to be pretty almost the same for smaller flip angles and for larger flip angles there is a sudden rise variance. Histogram of the estimation results of the smaller flip angle (*i.e.*150°, Figure 2.4.C) imitates the Gaussian distribution with a

little skewness to the right side. However, the relatively larger flip angle (i.e. 170°, Figure 2.4.D) displays a mixture model at smaller SNR values and a skewed (to the left) distribution at a relatively large SNR value. At smaller SNR values probability of misestimating the flip angle to 180° significantly rises as the SNR increases and also when the actual flip angle gets closer to the upper boundary.

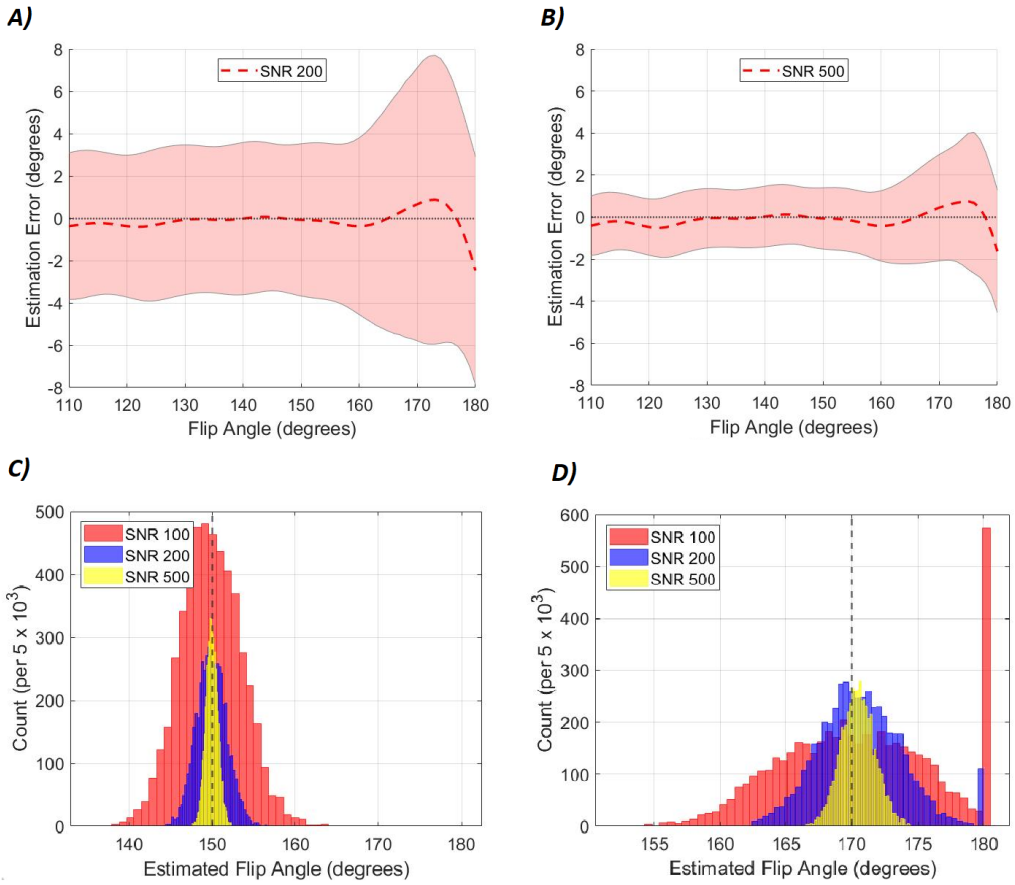

Figure 2.4: Flip angle optimization step results: A) mean flip angle estimation error at SNR of 200 plotted for a range of flip angles and the patches denote twice the size of standard deviation on each side of the main line, B) is the same as (A), with an SNR of 500, c) histogram of estimation results when the actual flip angle was 150° at SNR values of 100, 200, and 500, and D) the same as (C), with the actual flip angle of 170°. All of the generated signal decays used for this figure had an MWF of 15%.

2.3.3 Effect on MWF Estimation

Comparison of the ratio of MWF S.D. of estimated flip angle method to the supplied flip angle approach (Figure 2.5.A, B) shows improvement of repeatability and preci-

sion in MWF estimation, particularly when there is little to no MWF signal available in the signal decay. This pattern of precision improvement is larger at smaller flip angles and smaller SNR values. An opposite pattern of ratio of S.D. is observed at high SNRs (> 500) when the actual refocusing angle is around 170°, in which using the estimated flip angle parameter leads to higher precision.

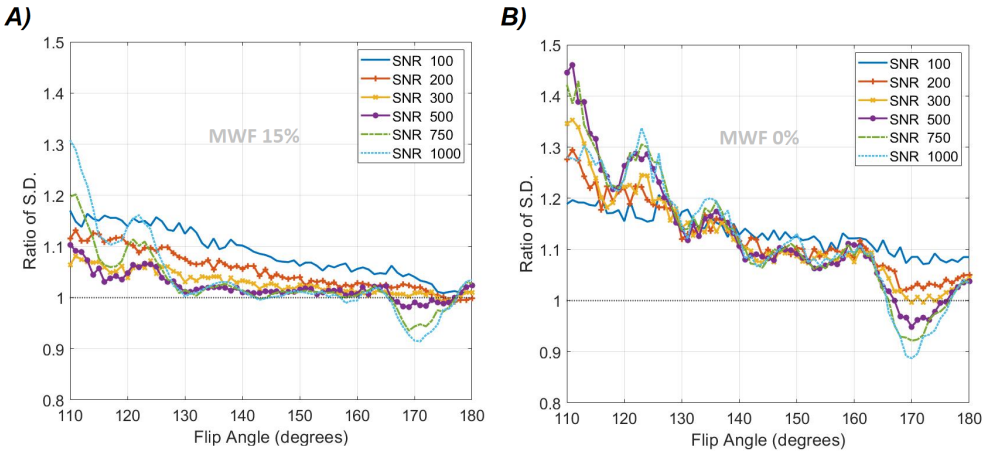

Figure 2.5: Ratio of the standard deviation of MWF estimations using estimated flip angle and supplied flip angle. The MWF values used were A) 15% and B) 0%. Values over the dotted line (y = 1) are where the precision of supplied flip angle map MWF estimation is better than estimated flip angle method.

2.3.4 In-vivo Results

An anecdotal example of the flip angle map and reference map is shown in Figure 2.6. The two maps seem to show overall good consistency, but looking at the percentage difference of the two maps shown in Figure 2.6.D¸ the underlying difference emerge. The expectation was to see a uniform map across the brain with a little paper and sand like noise (except for the CSF region). However, patterns of structure oriented contrasts are observed in the ratio map. WM regions seem to follow a general over-estimation in the estimated flip angle map with respect to the reference map.

Calculating the flip angle difference map by subtraction of the two maps provides a deeper understanding of voxel-wise estimation performance (Figure 2.7). Looking

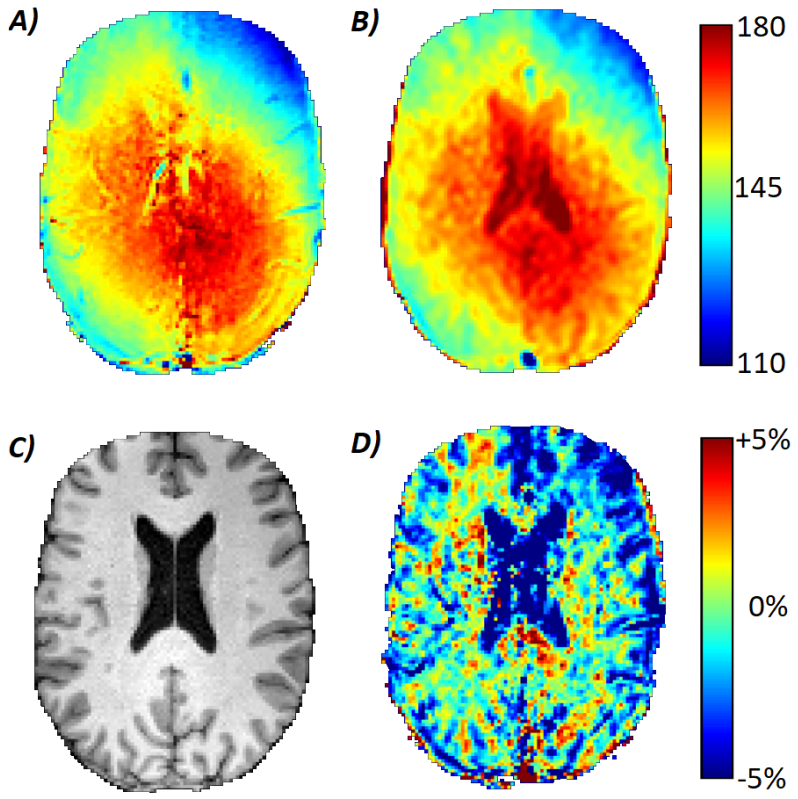

Figure 2.6: An example of flip angle maps from the same data-set. A) Estimated flip angle map (the result of the optimization step), and B) reference flip angle map of the same slice. D) Same slice of the magnitude image of the registered MPRAGE data. C) Percentage difference of the maps in parts A and B. Values over 1.0 denote where the estimated flip angle map is larger than the reference map.

at the difference maps (acquired from different subjects), in the slice lower in the brain a pattern of overestimation bias in the white matter regions can be observed. This positive bias follows the same structure as seen in the percentage difference map (Figure 2.6.D). However, when moving to slices higher in the brain we see less difference and more consistency between the two maps.

Figure 2.8, illustrates MWF maps produced by the two methods in three different subjects. The top row (Figure 2.8.A) depicts the estimated flip angle method results and the bottom row (Figure 2.8.B) the supplied flip angle results. Both maps are similar, however, the supplied flip angle MWF maps show elevated contrast in the WM (arrows point to notable examples) and even darker CSF.

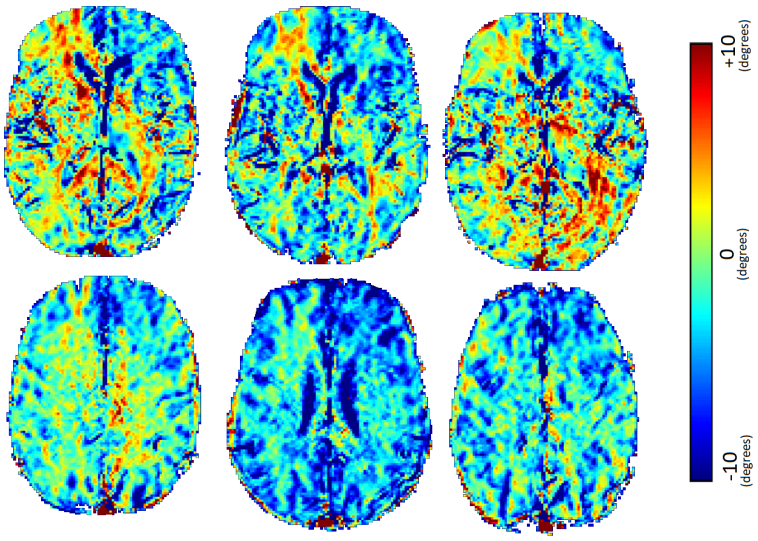

Figure 2.7: Difference maps (in degrees) of the estimated flip angle and reference maps. Maps that share a column are from the same subject but different slices. Three different subjects were chosen for this figure.

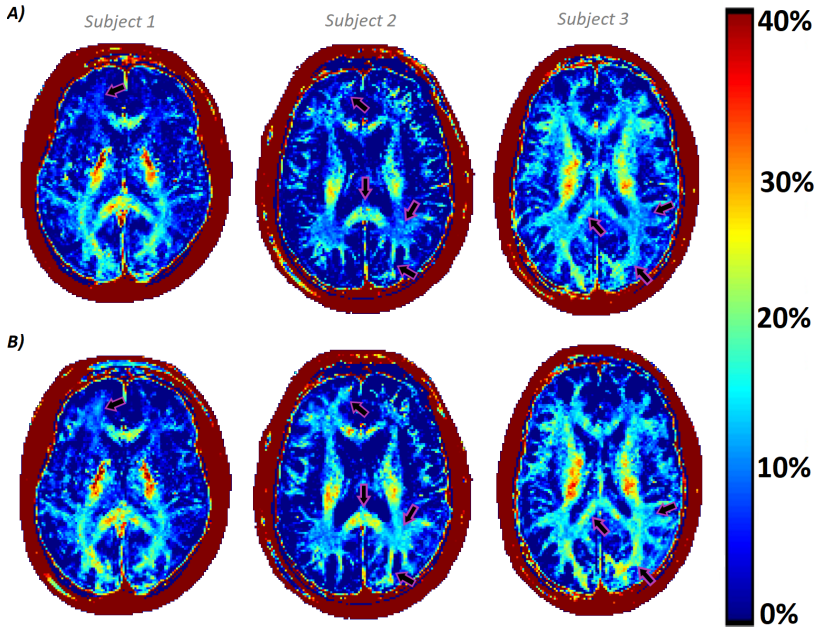

Figure 2.8: The results of the 3D GRASE sequence of a single representative subject after supplying flip angle using: A) estimated flip angle map (top row), and B) reference flip angle map (bottom row) to the NNLS process. The amplitude calibration is the same for all MWF maps. Arrows point out the anecdotal notable differences observed in the contrasts of the two maps.

ROI analysis of MWF maps illustrates a high correlation (correlation efficient $\approx$ 0.97) between results of the two approaches (the results are summarized numerically in Table 2.1). The mean of the WM structures has increased in comparison and on the other hand mean of the GM structure has decreased. In WM structures there are overestimations of refocusing angle hence a positive flip angle difference is observed overall. And on the other hand in the ROIs within GM matter territories, we see a negative flip angle difference mean which would mean that the estimated flip angle method would overestimate in such areas (supplied flip angle method produces smaller mean MWF).

Table 2.1: Summary of mean and S.D. of MWF values across all subjects. The flip angle difference is calculated by subtracting the mean estimated flip angle values by the mean reference flip angles. P-values show the significance of mean MWF difference in each ROIs when comparing the two methods, and Pearson's correlation coefficient of the mean MWF using the two methods are also brought here. The values in the table all round to one decimal point except for p-values.

Region of Interest	**Estimated FA MWF(%)**	**Supplied FA MWF(%)**	**FA Difference (degrees)**	**P-value (t-test)**	**Correlation Coefficient**
Splenium	16.9 ± 3.5	17.7 ± 3.1	0.4 ± 3.62	0.092	0.94
Genu	16.8 ± 2.8	15.8 ± 2.5	0.6 ± 2.16	0.047	0.90
Forceps Major	13.2 ± 1.8	14.7 ± 1.4	1.4 ± 2.7	0.004	0.85
Putamen	10.2 ± 2.5	9.8 ± 2.2	-2.2 ± 2.8	0.070	0.99
Caudate	5 ± 1.7	3.9 ± 1.1	-1.5 ± 2.2	0.016	0.80

Figure 2.8, is the visual representation of the mean MWF results in Table 2.1, which delineates a trend of decreased variability when supplying the flip angles. MWF values in the GM territories have also slightly decreased using the proposed method. There is a generally strong linear relationship between the results of the two methods which was expected, and the correlation coefficient seems to slightly drop in the forceps major and caudate ROIs. We should mention that most of the chosen ROIs were

in the lower regions of the brain, which we saw the largest differences between the estimated flip angle and the reference map. Consequently, more notable differences can be observed.

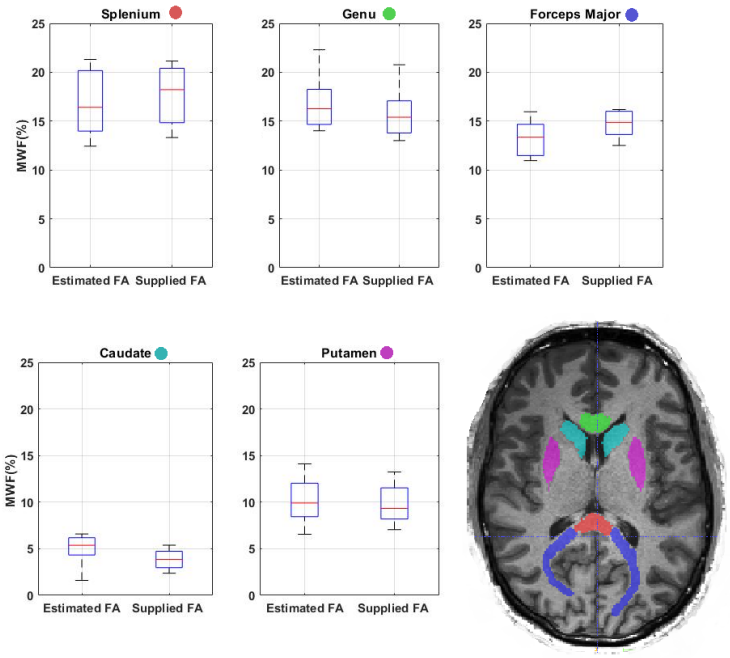

Figure 2.9: Boxplot of mean MWF values in each ROIs for all subjects. Three top row ROIs are from WM structures and the bottom row ones are deep GM territories. A slice from an MPRAGE acquisition containing color coded regions representing the ROIs is also included for the readers' interest.

2.4 Discussion

We explored effects of flip angle parameter on the final product of NNLS fitting (*i.e.* MWF), using ideal signal and for the case of noisy data, which resulted in a similar pattern that: over (under) -estimation of flip angle parameter would result in under (over) -estimation of MWF value compared to the ground truth. One theory for this pattern could be when the flip angle difference is positive (flip angle overestimation), as MW signal is only present at a few data points (echoes), it is more likely to be considered as noise by the NNLS process and the solution thrown off a bit; and for the case of negative flip angle (flip angle underestimation) the opposite takes place

in the process as the decay pattern comes into the equation, so the difference of the pattern of signal decay could be filled using decays from shorter T_2 values.

Here, the SNR definition was carefully stipulated (using amplitude of TE = 0), so that it would be calculated independent of the flip angle value assigned for simulation. Therefore, noise level (noise power) would be the same for all flip angles, considering the fact that for flip angles smaller (or larger) than 180°, the simulated signal would contain relatively smaller power. Hence, for a smaller flip angle, we would have a smaller signal to noise power ratio. However, our simulations (Figure 2.4) with the assumed definition of SNR, show that the flip angle estimation step produces similar and consistent results at all flip angles (except when we reach the upper boundary) for the same SNR, which could be explained by the emergence of the specific signal patterns generated at smaller flip angles, that compensates for the loss of signal power. The upper boundary effect was very much visible at all SNR values and even though simulated signal contained relatively larger signal power at such flip angle values, flip angle estimation near the boundary has the smallest accuracy and precision.

Difference of estimated flip angle map and the reference map calculated for in-vivo results (Figure 2.7), interestingly marked up WM areas and basically, all areas that contained signal decays with short T_2 component at slices in the middle and lower regions of the brain, with significantly positive differences. Therefore, this might thwart the efforts to use a spatial smoothing factor for the flip angle estimation to result in a better global flip angle fit, due to the structure oriented details observed in the estimated flip angle map. Moreover, we observed good consistency between the estimated flip angle map and reference map higher in the brain. This phenomenon can be due to the larger physiological noise in lower regions of the brain, and T_2^* effects of the GRASE sequence. Based on in-vivo results, there is an underestimation of flip angle bias where there is little to no short T_2 component in the signal decay, and an overestimation bias for tissue with significant MW signal (*i.e.* WM regions) or where short T_2 signal is observed, in slices lower in the brain. We should also

mention the top right region of the brain which seems to deviate from this pattern and is suspected to be due to the relatively smaller B_1 values observed in this region. In a recent study by Lankford and Does [50], there were predictions of spatial effects due to inaccuracies and inconsistencies of the presumed model on T_2 fitting results, which could explain the effects observed in the estimated flip angle map; As the optimization step is mainly based on minimization of the T_2 fitting solution. In another study by Wiggermann *et al.* [30], a good consistency between the estimated flip angle and the ground truth was found in their simulations, which we repeated and achieved the same results, but the simulations supposedly lack the artifacts that are present in the in-vivo results.

Lankford and Does, postulated that in order for the flip angle map to have a reducing effect on variance its SNR must be at least larger than half of the SNR of multi-echo acquisition, which here was met even though B1 map acquisition time was much shorter. Moreover, their assumption that high SNR values of multi-echoes would make it unlikely to have any effect on T_2 estimation does not hold, as the SNR of our acquisition was less than the necessary minimum SNR (=700) that Graham *et al.* previously demonstrated [53]. They also demonstrate that constraining flip angle to 180° (for Flip angle $>$ 150°) would decrease variability, which explains why we observe an undershoot in the ratio of standard deviations (Figure 2.5) near the upper boundary. The upper boundary effect mostly affects mean MWF estimate rather than variance, but we still see improvements in the variance even for larger flip angles.

Following the patterns of flip angle difference map, we observed (Table 2.1) elevation of MWF mean in ROIs in the WM and slight drop of MWF mean in deep GM territories, which was in alignment to simulation results of effects of flip angle difference to the ground truth on MWF estimation. Most of the chosen ROIs were in the lower regions of the brain, which we saw the largest differences between the estimated flip angle and the reference map. Consequently, more notable differences can be observed,

regions higher in the brain where there is more consistency between the two maps we would see less difference in the mean MWF values. It should be mentioned that large MWF values in deep GM territories observed in Figure 2.7, are possibly due to the iron and calcium concentration effect on shortening IE water T_2 values in the distribution [42, 43], and these areas could be dealt with using a post-processing step through peak assessment at large SNR values (since we need to be sure MW signal is not merged with IE due to smoothing of regularization) and adaptive thresholding. Here, we only focused on flip angle effects in the 3D acquisition and since B1 transmit field is considered to vary slowly across the slab of interest, a single flip angle is assumed for an entire voxel [26, 30]. However, for 2D acquisition due to the effect of slice profile, a range of flip angles is considered across each voxel, therefore in order to generate underlying decay curve for the fitting process, either the Bloch equation needs to be solved or EPG decay profiles need to be integrated across the slice [25, 51]. This increased complexity makes the results to be reasonably affected by the B_1 field, and B_1 estimations have been deemed questionable even for single component T_2 fitting [25, 51]. Previous work on 2D multi-echo spin-echo multi-component T_2 analysis [47, 60], showed plausible and reproducible results for MWF maps, but the effects of B_1 estimation were not examined thoroughly. Their B_1 estimation maps [47], denote the same structure oriented patterns in the estimated B_1 maps which need to be carefully inspected. We suspect using an independent B_1 map on 2D data would also be beneficial and opens up the possibility of using different refocusing angles for the echo train to deal with SAR issues or alternate decay models that maintain myelin water signal longer in the echo train by using smaller refocusing angles.

2.5 Conclusion

This study investigated the effects of the flip angle parameter in a common NNLS procedure used in the MWI literature. Comparing the estimated flip angle map with a reference flip angle map (acquired independently), enlightened the fact that there are

biases observed in the flip angle estimation results lower in the brain, especially where there is little to no short T_2 signal available in signal decay. Moreover, we observed structure oriented effects in the estimated flip angle maps in the 3D GRASE data, thus affecting the MWF estimation in such regions. Supplying an independent flip angle map to the NNLS procedure, proved to be fruitful and somewhat decreased inter-subject variability of MWF mean in the WM and GM ROIs which were in the troubled regions. Also, an elevation of mean MWF in the WM regions and a drop of the mean MWF in the GM territories were observed when supplying the reference flip angle map values. This proposed approach alleviates further variability that miscalculation of refocusing angle could introduce to NNLS solution.

2.6 Acknowledgment

This work was supported by the Canadian Institutes of Health Research [grant number MOP 102582]; and the Natural Sciences and Engineering Research Council of Canada [grant number RGPIN-2017-04006].

The 3D GRASE sequence was received from Dr. Jongho Lee at Seoul National University. The code received from the UBC MRI Research Center was the basis for the development of simulation codes and further analysis regarding MWF calculations.

References

[7] C Laule, E Leung, D. K. Li, A. L. Traboulsee, D. W. Paty, A. L. MacKay, and G. R. Moore, "Myelin water imaging in multiple sclerosis: Quantitative correlations with histopathology," *Multiple Sclerosis Journal*, vol. 12, no. 6, pp. 747–753, 2006, PMID: 17263002. DOI: 10.1177/1352458506070928.

[8] J. Lee, J.-W. Hyun, J. Lee, E.-J. Choi, H.-G. Shin, K. Min, Y. Nam, H. J. Kim, and S.-H. Oh, "So you want to image myelin using mri: An overview and practical guide for myelin water imaging," *Journal of Magnetic Resonance Imaging, Online ahead of print.*, vol. n/a, no. n/a, 2020 Feb 3. DOI: 10.1002/jmri.27059.

[9] M. D. Does, "Inferring brain tissue composition and microstructure via mr relaxometry," *NeuroImage*, vol. 182, pp. 136 –148, 2018, Microstructural Imaging, ISSN: 1053-8119. DOI: 10.1016/j.neuroimage.2017.12.087.

[10] D. Kumar, S. Siemonsen, C. Heesen, J. Fiehler, and J. Sedlacik, "Noise robust spatially regularized myelin water fraction mapping with the intrinsic b1-error correction based on the linearized version of the extended phase graph model," *Journal of Magnetic Resonance Imaging*, vol. 43, no. 4, pp. 800–817, 2016. DOI: 10.1002/jmri.25078.

[18] R. S. Menon and P. S. Allen, "Application of continuous relaxation time distributions to the fitting of data from model systems and excised tissue," *Magnetic Resonance in Medicine*, vol. 20, no. 2, pp. 214–227, 1991. DOI: 10.1002/mrm.1910200205.

[19] A. Mackay, K. Whittall, J. Adler, D. Li, D. Paty, and D. Graeb, "In vivo visualization of myelin water in brain by magnetic resonance," *Magnetic Resonance in Medicine*, vol. 31, no. 6, pp. 673–677, 1994. DOI: 10.1002/mrm.1910310614.

[22] C. Laule, P. Kozlowski, E. Leung, D. K. Li, A. L. MacKay, and G. W. Moore, "Myelin water imaging of multiple sclerosis at 7 t: Correlations with histopathology," *NeuroImage*, vol. 40, no. 4, pp. 1575 –1580, 2008, ISSN: 1053-8119. DOI: 10.1016/j.neuroimage.2007.12.008.

[23] K. P. Whittall, A. L. Mackay, D. A. Graeb, R. A. Nugent, D. K. B. Li, and D. W. Paty, "In vivo measurement of t2 distributions and water contents in normal human brain," *Magnetic Resonance in Medicine*, vol. 37, no. 1, pp. 34–43, 1997. DOI: 10.1002/mrm.1910370107.

[24] T. Prasloski, A. Rauscher, A. L. MacKay, M. Hodgson, I. M. Vavasour, C. Laule, and B. Mädler, "Rapid whole cerebrum myelin water imaging using a 3d grase sequence," *NeuroImage*, vol. 63, no. 1, pp. 533 –539, 2012, ISSN: 1053-8119. DOI: 10.1016/j.neuroimage.2012.06.064.

[25] R. M. Lebel and A. H. Wilman, "Transverse relaxometry with stimulated echo compensation," *Magnetic Resonance in Medicine*, vol. 64, no. 4, pp. 1005–1014, 2010. DOI: 10.1002/mrm.22487.

[26] T. Prasloski, B. Mädler, Q.-S. Xiang, A. MacKay, and C. Jones, "Applications of stimulated echo correction to multicomponent t2 analysis," *Magnetic Resonance in Medicine*, vol. 67, no. 6, pp. 1803–1814, 2012. DOI: 10.1002/mrm.23157.

[27] J. Hennig, "Echoes—how to generate, recognize, use or avoid them in mr-imaging sequences. part i: Fundamental and not so fundamental properties of spin echoes," *Concepts in Magnetic Resonance*, vol. 3, no. 3, pp. 125–143, 1991. DOI: 10.1002/cmr.1820030302.

[30] V. Wiggermann, I. M. Vavasour, S. Kolind, A. L. MacKay, G. Helms, and A. Rauscher, "Non-negative least squares computation for in vivo myelin mapping using simulated multi-echo spin-echo t2 decay data," *NMR in Biomedicine*, vol. 33, no. 12, e4277, 2020.

[38] A. MacKay, C. Laule, I. Vavasour, T. Bjarnason, S. Kolind, and B. Mädler, "Insights into brain microstructure from the t2 distribution," *Magnetic resonance imaging*, vol. 24, no. 4, pp. 515–525, 2006.

[39] I. M. Vavasour, K. P. Whittall, A. L. Mackay, D. K. Li, G. Vorobeychik, and D. W. Paty, "A comparison between magnetization transfer ratios and myelin water percentages in normals and multiple sclerosis patients," *Magnetic resonance in medicine*, vol. 40, no. 5, pp. 763–768, 1998.

[40] C. K. Jones, Q.-S. Xiang, K. P. Whittall, and A. L. MacKay, "Linear combination of multiecho data: Short t2 component selection," *Magnetic Resonance in Medicine: An Official Journal of the International Society for Magnetic Resonance in Medicine*, vol. 51, no. 3, pp. 495–502, 2004.

[41] J. P. Wansapura, S. K. Holland, R. S. Dunn, and W. S. Ball Jr, "Nmr relaxation times in the human brain at 3.0 tesla," *Journal of Magnetic Resonance Imaging: An Official Journal of the International Society for Magnetic Resonance in Medicine*, vol. 9, no. 4, pp. 531–538, 1999.

[42] H. E. Möller, L. Bossoni, J. R. Connor, R. R. Crichton, M. D. Does, R. J. Ward, L. Zecca, F. A. Zucca, and I. Ronen, "Iron, myelin, and the brain: Neuroimaging meets neurobiology," *Trends in neurosciences*, vol. 42, no. 6, pp. 384–401, 2019.

[43] C. Birkl, A. M. Birkl-Toeglhofer, V. Endmayr, R. Höftberger, G. Kasprian, C. Krebs, J. Haybaeck, and A. Rauscher, "The influence of brain iron on myelin water imaging," *Neuroimage*, vol. 199, pp. 545–552, 2019.

[44] C. M. Collins, W. Liu, W. Schreiber, Q. X. Yang, and M. B. Smith, "Central brightening due to constructive interference with, without, and despite dielectric resonance," *Journal of Magnetic Resonance Imaging: An Official Journal of the International Society for Magnetic Resonance in Medicine*, vol. 21, no. 2, pp. 192–196, 2005.

[45] C Jones, Q Xiang, K. Whittall, and A MacKay, "Calculating t2 and b1 from decay curves collected with non-180 refocusing pulses," in *11th annual meeting of the international society of magnetic resonance in medicine. Toronto, Canada*, vol. 1018, 2003.

[46] J. Hennig, "Multiecho imaging sequences with low refocusing flip angles," *Journal of Magnetic Resonance (1969)*, vol. 78, no. 3, pp. 397–407, 1988.

[47] A. Akhondi-Asl, O. Afacan, M. Balasubramanian, R. V. Mulkern, and S. K. Warfield, "Fast myelin water fraction estimation using 2d multislice cpmg," *Magnetic resonance in medicine*, vol. 76, no. 4, pp. 1301–1313, 2016.

[48] G. S. Drenthen, W. H. Backes, A. P. Aldenkamp, G. J. Op't Veld, and J. F. Jansen, "A new analysis approach for t2 relaxometry myelin water quantification: Orthogonal matching pursuit," *Magnetic resonance in medicine*, vol. 81, no. 5, pp. 3292–3303, 2019.

[49] L. E. Lee, E. Ljungberg, D. Shin, C. R. Figley, I. M. Vavasour, A. Rauscher, J. Cohen-Adad, D. K. Li, A. L. Traboulsee, A. L. MacKay, *et al.*, "Inter-vendor reproducibility of myelin water imaging using a 3d gradient and spin echo sequence," *Frontiers in neuroscience*, vol. 12, p. 854, 2018.

[50] C. L. Lankford and M. D. Does, "Propagation of error from parameter constraints in quantitative mri: Example application of multiple spin echo t2 mapping," *Magnetic resonance in medicine*, vol. 79, no. 2, pp. 673–682, 2018.

[51] K. C. McPhee and A. H. Wilman, "Transverse relaxation and flip angle mapping: Evaluation of simultaneous and independent methods using multiple spin echoes," *Magnetic resonance in medicine*, vol. 77, no. 5, pp. 2057–2065, 2017.

[52] S. M. Meyers, C. Laule, I. M. Vavasour, S. H. Kolind, B. Mädler, R. Tam, A. L. Traboulsee, J. Lee, D. K. Li, and A. L. MacKay, "Reproducibility of myelin water fraction analysis: A comparison of region of interest and voxel-based analysis methods," *Magnetic resonance imaging*, vol. 27, no. 8, pp. 1096–1103, 2009.

[53] S. J. Graham, P. L. Stanchev, and M. J. Bronskill, "Criteria for analysis of multicomponent tissue t2 relaxation data," *Magnetic Resonance in Medicine*, vol. 35, no. 3, pp. 370–378, 1996.

[54] L Chen, M Bernstein, J Huston, and S Fain, "Measurements of t1 relaxation times at 3.0 t: Implications for clinical mra," in *Proceedings of the 9th Annual Meeting of ISMRM, Glasgow, Scotland*, 2001.

[55] C. Labadie, J.-H. Lee, W. D. Rooney, S. Jarchow, M. Aubert-Frécon, C. S. Springer Jr, and H. E. Möller, "Myelin water mapping by spatially regularized longitudinal relaxographic imaging at high magnetic fields," *Magnetic resonance in medicine*, vol. 71, no. 1, pp. 375–387, 2014.

[56] H. Gudbjartsson and S. Patz, "The rician distribution of noisy mri data," *Magnetic resonance in medicine*, vol. 34, no. 6, pp. 910–914, 1995.

[57] S. H. Kolind, B. Mädler, S. Fischer, D. K. Li, and A. L. MacKay, "Myelin water imaging: Implementation and development at 3.0 t and comparison to 1.5 t measurements," *Magnetic Resonance in Medicine: An Official Journal of the International Society for Magnetic Resonance in Medicine*, vol. 62, no. 1, pp. 106–115, 2009.

[58] J. Guo, Q. Ji, and W. E. Reddick, "Multi-slice myelin water imaging for practical clinical applications at 3.0 t," *Magnetic resonance in medicine*, vol. 70, no. 3, pp. 813–822, 2013.

[59] L. I. Sacolick, L. Sun, M. W. Vogel, W. T. Dixon, and I. Hancu, "Fast radiofrequency flip angle calibration by bloch–siegert shift," *Magnetic resonance in medicine*, vol. 66, no. 5, pp. 1333–1338, 2011.

[60] G. S. Drenthen, W. H. Backes, A. P. Aldenkamp, and J. F. Jansen, "Applicability and reproducibility of 2d multi-slice grase myelin water fraction with varying acquisition acceleration," *Neuroimage*, vol. 195, pp. 333–339, 2019.

Chapter 3

Constraining the B_1^+ Parameter in 2D MESE data for MWI analysis

3.1 Introduction

The 3D MESE sequence could be considered as the gold standard for the acquisition of MESE data for the purpose of MWI analyses. However, the classic 3D MESE method is too long to be used in practical scan times. To achieve feasible scan time, 3D GRASE was suggested as an alternative using a three-fold speed up by collecting 2 gradient echoes around each spin echo. While 3D GRASE reduces total scan time to about a third, it produces data with lower SNR and contains T_2^* related artifacts [37, 47]. Moreover, the echo shift scheme requires the echo spacing to increase which produces suboptimal data that results in overestimation of MWF values [37]. Two-dimensional MESE methods have been used historically for MWI, but often with only a single slice to minimize magnetization transfer (MT) effects. Extending the single slice 2D sequence to a 2D multi-slice sequence is one way to achieve feasible scan time and brain coverage as an alternative to 3D methods. As well as MT effects, 2D also requires more complex modeling owing the slice selective pulses. Complete Bloch modeling is likely needed due to the very short myelin water T_2 time and the need to exactly account for RF pulse effects. Akhondi-Asl and colleagues have recently demonstrated this method using full Bloch modeling [47]. Beginning with a similar approach, we examine the value of an independent B1+ map in the MWI analysis

pathway.

More specifically, switching from a single slice (or 3D) to a 2D multi-slice MESE version requires changing non-selective refocusing pulses (or a selective one with a wide slice profile) into appropriate slice-selective ones. This introduces another complexity to the expected signal decay models on top of possible incidental MT effects from off-resonant slice excitation. Slice profiles in the 2D MESE scheme are not perfectly rectangular even in the absence of B_1^+ inhomogeneities. Therefore, one needs to account for the slice profiles to predict signal decay curves for multi-component analysis of multi-echo data. One could broaden the refocusing pulse profile to be more uniform throughout the excited slice; however, this solution would require a large gap between slices and limit the number of slices acquired within a single TR.

To predict the signal decay curves for different relaxation times we need to settle on a method that is the most accurate and reliable. There have been approaches where the slice profiles are estimated using the Shinnar-LeRoux (SLR) method where relaxation times are ignored during the application of RF pulses [14, 61], which could result in inaccurate decay curves corresponding to shorter T_2 values (like myelin water). Therefore, here we solved the Bloch equations to be as close to the reality of the data as we could.

Of course, the issue of B_1^+ inhomogeneity in the analysis should also be addressed. To handle the B_1^+ parameter, we used two different methods: First, we applied a similar scheme to past work [26, 47] that is adopting an optimization step to estimate B_1^+ value using the decay data; and the second novel method was to provide the B_1^+ values by employing an independent B_1^+ map to supply to the analysis.

3.2 Methods

3.2.1 Theory

The evolution of magnetization vectors in the presence of magnetic field gradients and RF fields can be described using the Bloch equations. Let $\vec{M}(t) = [M_x(t), M_y(t), M_z(t)]$ be the magnetization vector, then Bloch equations in the rotating frame read:

$$\frac{dM_x(t)}{dt} = \gamma(M(t) \times B_1(t))_x - \frac{M_x(t)}{T_2} \tag{3.1}$$

$$\frac{dM_y(t)}{dt} = \gamma(M(t) \times B_1(t))_y - \frac{M_y(t)}{T_2} \tag{3.2}$$

$$\frac{dM_z(t)}{dt} = \gamma(M(t) \times B_1(t))_z - \frac{M_z(t) - M_0}{T_1} \tag{3.3}$$

Where γ is the gyromagnetic ratio and $B_1(t)$ is the magnetic field experienced by the magnetization vector in the rotating frame. The $B_1(t)$ is defined by the sequence and can be simulated. We simulated our 2D MESE sequence pulse train using Siemens' simulation tool (POET) which produced a protocol file containing the exact gradients and RF fields as vectors over time. These values are depicted in Figure 3.1. Afterward, these vectors are processed to be used as direct inputs to a Bloch simulator. For Bloch simulation, a Bloch simulator toolkit was imported from the code project of Professor Brian A. Hargreaves (http://www-mrsrl.stanford.edu/~brian/blochsim/). This code models the RF pulse axis and one gradient axis (could handle up to 3-dimensional gradients), which we choose as the slice select dimension. The Bloch simulator was wrapped by our code to generate the proper signal decay curves for the corresponding relaxation parameters and B_1^+ values. Simulations were done over a symmetric position vector twice the size of the slice thickness at over 2000 different points, and time spacing in the simulation was set to $5\mu s$.

To generate a dictionary matrix of decay curves as a lookup table for multi-component analysis, 60 logarithmically spaced T_2 values ranging from 8 ms to 2

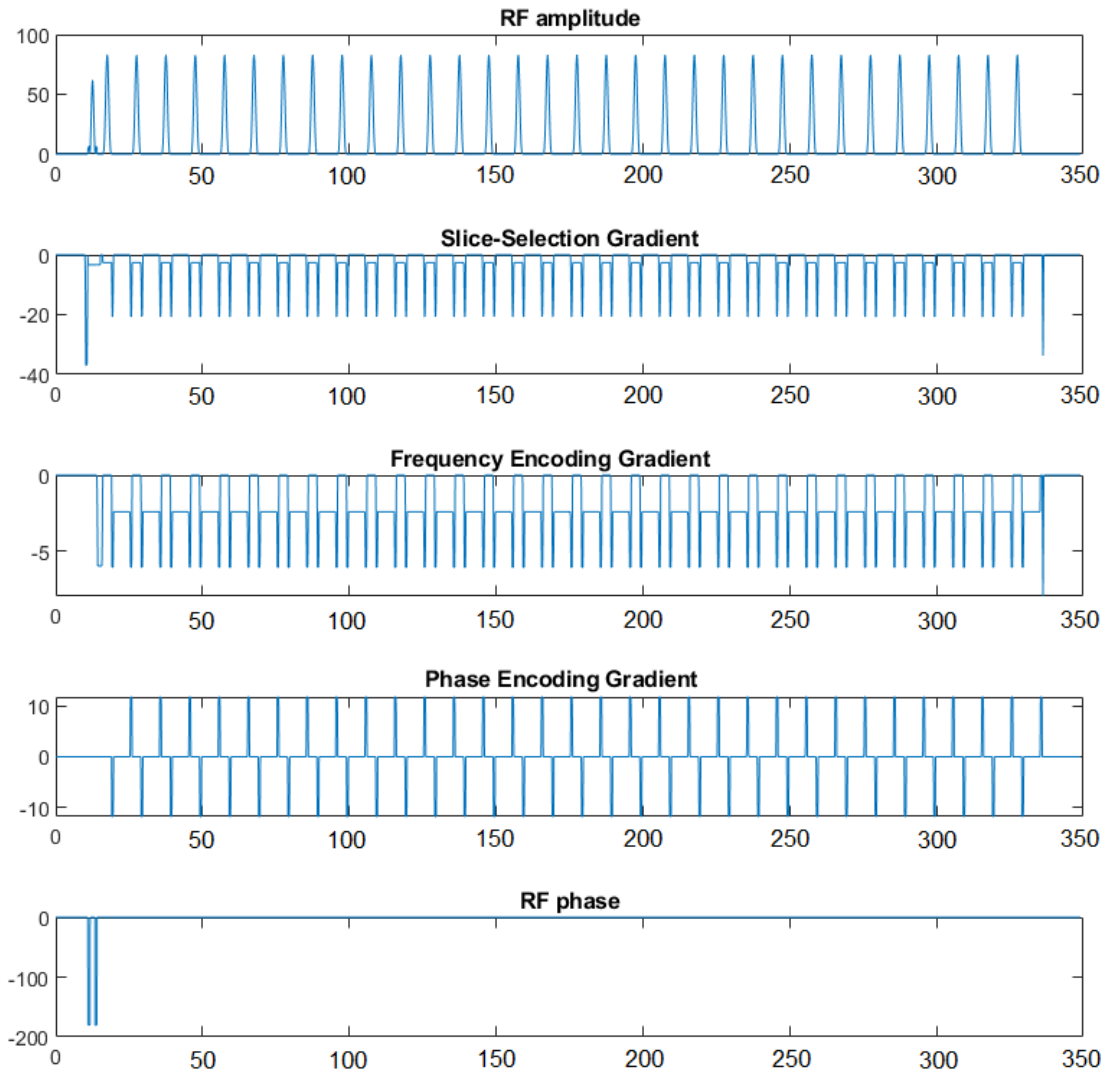

Figure 3.1: Simulated protocol of a 32 echoes 2D MESE sequence used in this work. This Scheme is for a single TR, and the time axis is in milliseconds and the y-axes unit are the direct output of the POET simulation: mT/m for gradients, RF magnitude is in $mT \times 10$, and RF phase is in degrees.

seconds were chosen (within the range used in the literature [23, 24, 30, 47, 48]) alongside normalized $B_1{}^+$ values over the range of 0.6 to 1.4 with 0.005 spacing. For the optimization step, the full range of $B_1{}^+$ values were tested in the multi-component analysis (non-negative least squares algorithm) and the smallest residual among the entire spectrum was chosen as the estimated $B_1{}^+$. After the $B_1{}^+$ value is settled the corresponding decay curves from the lookup table are chosen to apply a regularized

NNLS fitting procedure (same as 3D GRASE analysis in Chapter 2) to calculate a T_2 distribution and then the corresponding MWF value for each voxel.

3.2.2 Numerical Simulation

To simulate the $B_1{}^+$ estimation using the optimization step, 100 different $B_1{}^+$ values ranging from 0.5 to 1.5 were chosen to generate corresponding decay curves. To see the effect of MWF value on the estimation 15 values from 1% to 30% were adopted. The base T_2 distributions to simulate decay curves were generated by using two truncated Gaussians (truncated after 2 standard deviations and S.D. was chosen to be 10% of the mean) centered at 60 ms (intra/extra-cellular water) and 10 ms (myelin water) and the ratio of the area under the Gaussians was set based on the MWF values. Then 500 different Rician noise realizations were added to each decay curve. Then we will plot the estimation results for a range of different SNR levels to investigate the accuracy of results. The mean absolute error was calculated using the following equation:

$$MAE(B) = \frac{\sum_{n=1}^{N} |B - B_n|}{N} \tag{3.4}$$

Where B is the ground truth, B_n is the estimation result of the nth trial, and N denotes the number of trials (=500). The SNR levels ranging from 100 to 1000 were assumed here. To investigate the effect of $B_1{}^+$ error on MWF estimation, a range of errors (from -0.3 to 0.3) were assumed using a MWF of 15% for multi-component decay generation to simulate normal appearing WM signal.

3.2.3 In-vivo Experiments

Data were collected from five healthy subjects on a 3T Siemens Prisma (Erlangen, Germany). A 2D MESE sequence was used with TR 2000 ms, echo-spacing 10 ms, refocusing/excitation slice-thickness factor 1.26, distance factor 200%, slice thickness 5 mm, in-plane resolution $1.2 \times 1.3mm$, 3 averages, and acquisition time of 12 minutes.

A 40-second Bloch-Siegert B_1 mapping sequence was applied to produce a reference $B_1{}^+$ map with voxel dimensions of $1.3 \times 1.3 \times 3mm^3$. A 3D MPRAGE sequence with isotropic 1 mm resolution was also collected for the purpose of segmentation. Data was then registered to 2D MESE images using the SPM12 toolbox on MATLAB 2019a.

3.2.4 In-vivo Analysis

Two methods for computing MWF were tested using either standard fitting [26, 47] or the same fitting with the $B_1{}^+$ parameter supplied from the independent flip angle map. We used a threshold of 40 ms to calculate MWF values from the fitting procedure. For the fitting we applied the same regularized NNLS for multi-component T_2 analysis commonly used in literature [26, 30, 47], as mentioned in Section 3.2.1. Finally, WM regions were manually segmented (bilaterally) to calculate mean MWF for both methods, and a student t-test was applied to see whether there is a significant difference between the two methods. In addition, to depict the effect of using the proposed method the scatter-plots of MWF difference of the method versus the reference $B_1{}^+$ values were plotted, and linear regression was used to fit lines to the entire data illustrated in the scatter-plots.

3.3 Results

3.3.1 Simulation

Simulated signal decays using different $B_1{}^+$ values are shown in Figure 3.2. When the curves are normalized to the amplitude of their first echoes, decay curves that have $B_1{}^+$ values with equal distance to $B_1{}^+$ of 1 (symmetrical around 1) exhibit very similar decay patterns.

Histograms of $B_1{}^+$ estimation results are depicted in Figure 3.3 for $B_1{}^+$ of 1.1 and three different MWF of 1% (representative of signal with little to no MW signal), 15% (to simulate normal appearing WM signal), and 25%. $B_1{}^+$ estimation seems to

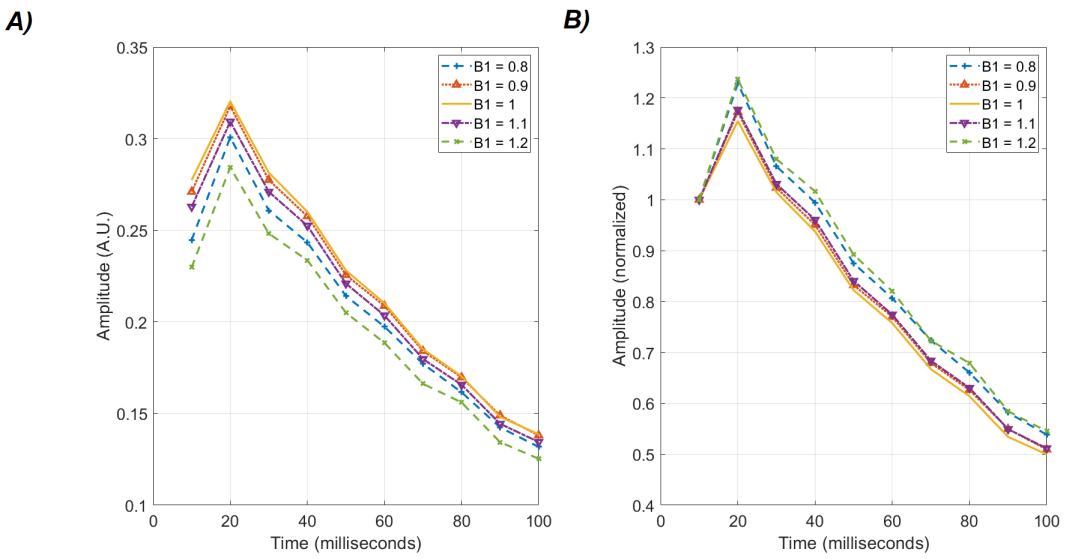

Figure 3.2: Simulated decay curves using different $B_1{}^+$ illustrating the subtle differences in decay pattern for values on either side of 1.0. The decay curves were produced using the POET simulation parameters of the 2D MESE sequence. All curves are generated using single-component decay using T_2 of $75ms$ and T_1 of $1s$. Curves in (B) are the same ones as (A) normalized to the first value of each curve

find a wide range of values for SNR of 100 and starts to separate into two distinct distributions as SNR levels increase. MWF level somewhat adversely affects the distribution of $B_1{}^+$ estimate (Figure 3.3).

Figure 3.4 shows the mean absolute error of estimation in the $B_1{}^+$ optimization step. Absolute mean error drops from about 10% to less than 3% when SNR increases from 100 to 1000. Error is mostly around $B_1{}^+ = 0.9$ and 1.1 for smaller SNRs and for larger SNRs it is narrowed around $B_1{}^+$ of 1. The optimization step has the smallest errors at the extreme $B_1{}^+$ values and the MWF levels have a subtle effect on the mean absolute error.

Now, let's take a look at the effects of using wrong $B_1{}^+$ estimates on MWF estimation in Figure 3.5. Both SNR values used for simulations resulted in similar patterns. The general pattern in Figure 3.5 is that when $B_1{}^+$ is less (more) than 1, mean MWF estimation would be over- (under-) estimated if we use larger (smaller) $B_1{}^+$ value compared to ground truth; and we would get under- (over-) estimated MWF the

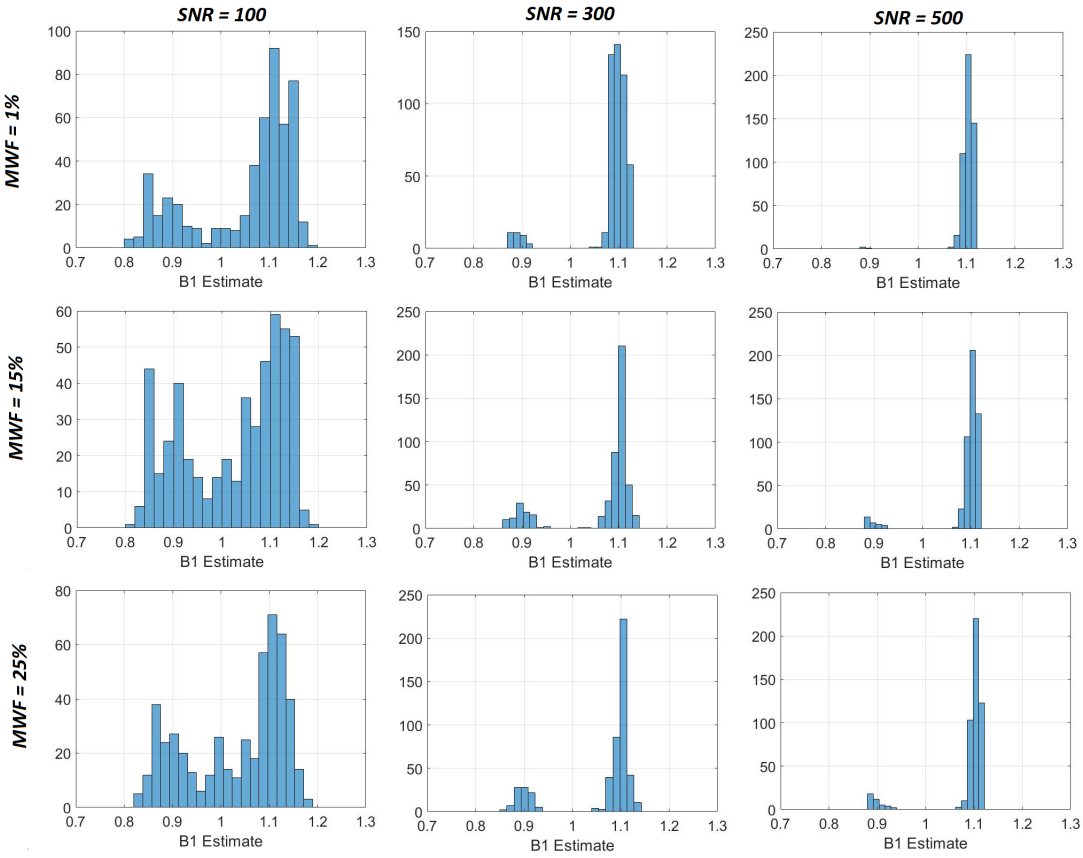

Figure 3.3: $B_1{}^+$ estimation results where ground truth is $B_1{}^+ = 1.1$. Histograms are plotted for SNRs of 100, 300, 400 for MWF values of 1%, 15%, and 25%. For each of the histograms, 500 points were simulated and the number of bins was set to 20.

other way around. This pattern would start to take the opposite direction as $B_1{}^+$ errors exceed 20% of the ground truth. Symmetrical $B_1{}^+$ values around 1 seem to take similar yet opposite patterns with respect to the $B_1{}^+$ error used for the fitting procedure.

3.3.2 In-vivo Experiments

$B_1{}^+$ maps from the optimization step results are depicted in Figure 3.6 alongside the reference map data. There seems to be a good consistency between the reference map and the estimated map where $B_1{}^+$ is less than 1 (correlation coefficient for $B_1{}^+ < 1$ is $r = 0.5$ and for $B_1{}^+ > 1$, $r = -0.2$ between the estimated and reference values) and underestimated for the rest. In the difference map, some structure oriented patterns

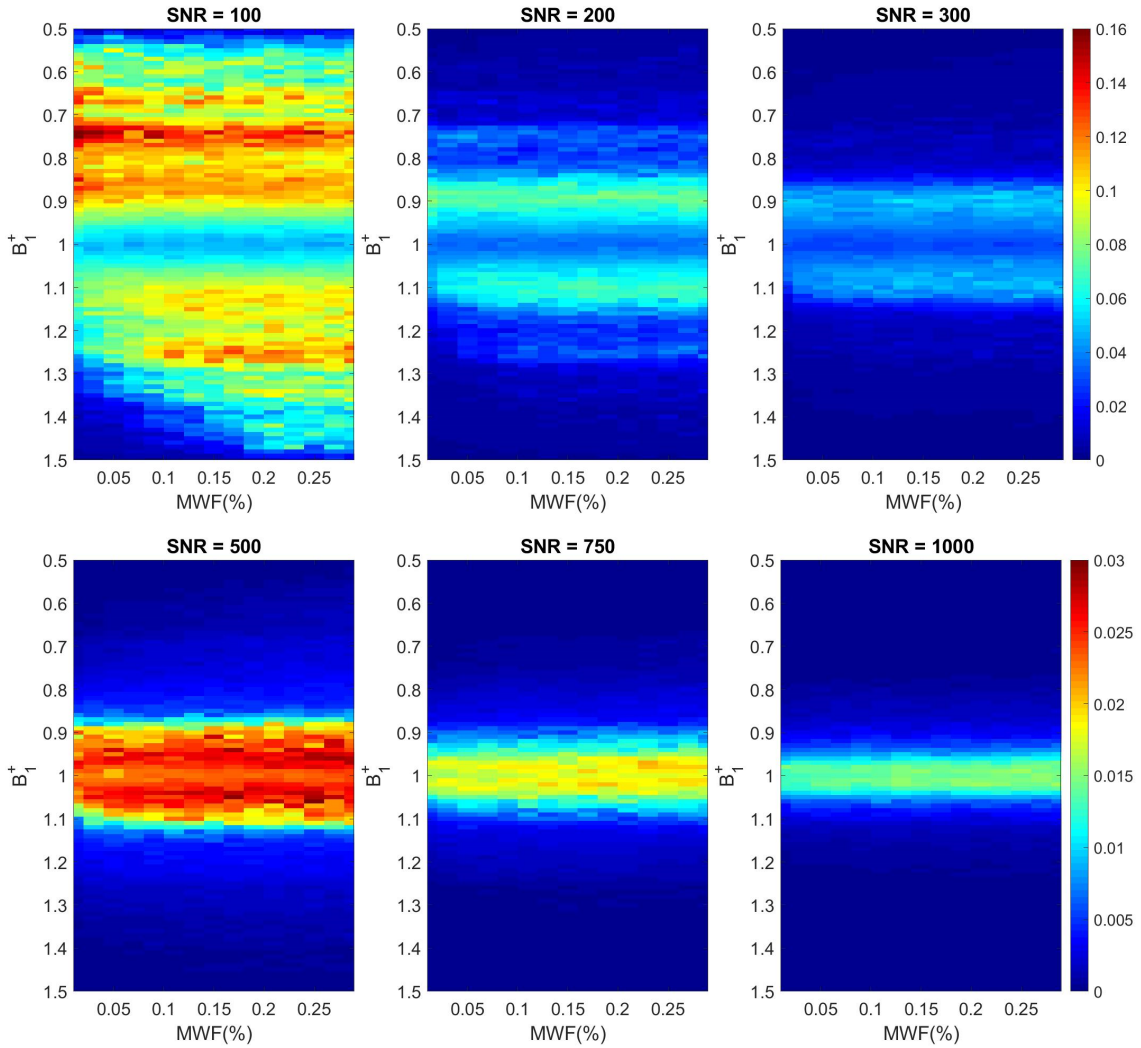

Figure 3.4: Mean absolute error of B_1^+ estimations for MWF range of 1% to 30%. Color scales are kept equal in each row; the first row scales to 0.16 and the second row to 0.03 for illustration purposes.

emerge.

MWF maps are shown in Figure 3.7, where we see some improvements when using the reference B_1^+ map for the multi-component analysis. The estimated B_1^+ results show some MWF underestimations in the WM tracts, compared to the supplied B_1^+ method (p-value = 0 using student t-test).

The box plots of the ROIs in Figure 3.8 do not seem to show any general patterns, however, the splenium which is usually in the region where we observe notable B_1^+

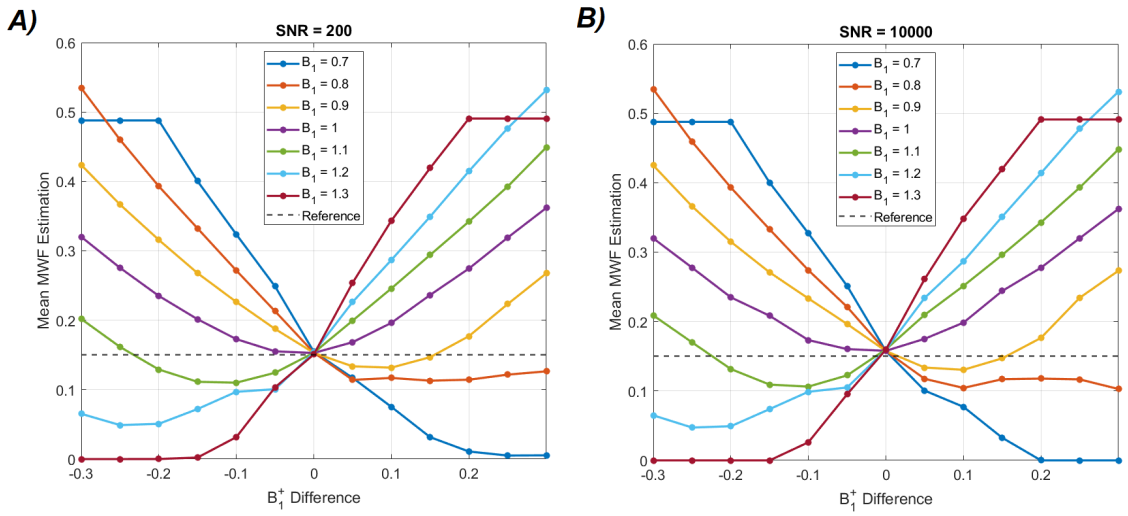

Figure 3.5: The effect of using wrong $B_1{}^+$ values on MWF estimations using SNR of A)200 and B)10000. Units on the x-axis show $B_1{}^+$ value error from the ground truth and the y-axis is the mean MWF estimation averaging over 500 experiments.

difference between the two maps, the paired t-test showed a significant difference between the two methods (p = 1.2e-4). Mean MWF over the entire WM (p-value= 4.2×10^{-5}) and also the frontal WM region (p-value = 0.02) showed a significant difference and a general mean MWF elevation in the mean MWF of the entire WM.

Figure 3.9 illustrates the scatter plots of all subjects where $B_1{}^+$ values and MWF difference of the two methods for all WM voxels. Methods perform similarly around $B_1{}^+$ of 1 and start to deviate for larger and smaller values. We tried linear regression ($\Delta MWF(\%) = mB_1^+ + b$, where m is the slope and b is the bias of the regression) for values over $B_1{}^+$ of 1 and attained slope of 33.3 with a bias of -34.2 (p-values $= 0, r = 0.6$), and repeated for values under $B_1{}^+ = 1$ and reached sloped -14.4 and bias of 13.7 (p-values $= 0, r = -0.4$).

3.4 Discussion

Here we replicated previously tested methods to produce MWF maps using a 2D MESE sequence, with a different approach of incorporating $B_1{}^+$ maps from an independent $B_1{}^+$ mapping sequence. The purpose was to improve the estimation process

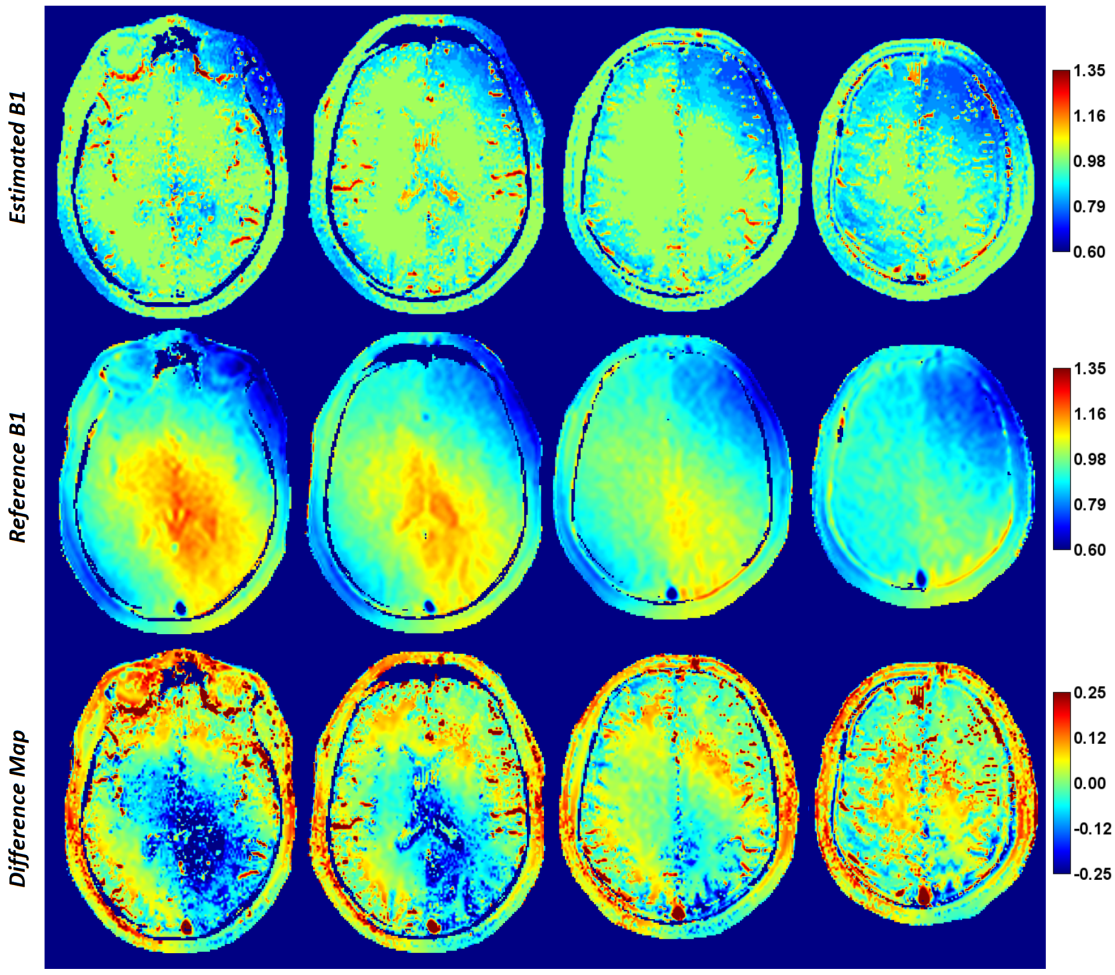

Figure 3.6: B_1^+ mapping results from optimization step (first row), registered B_1^+ maps form an independent B_1^+ mapping sequence (second row), and the difference of the two maps (third row).

of multi-component fitting by removing one of the main parameters in the estimation process. The independent B_1^+ map was compared to a standard B_1^+ estimation process from the decay data itself, as used in past work [24, 47].

Simulation results showed the level of unreliability of the estimation process across a range of SNRs and MWFs. Generally, the estimation absolute error decreases to less than 3% for SNR 1000. In the histogram results of the B_1^+ estimation, two distinct peaks appear that notably elevate the probability of mis-estimation. These two peaks generally seem to assume symmetrical values around B_1^+ of 1. However, with more extreme B_1^+ values such as less than 0.7 or greater than 1.3, the simulations show

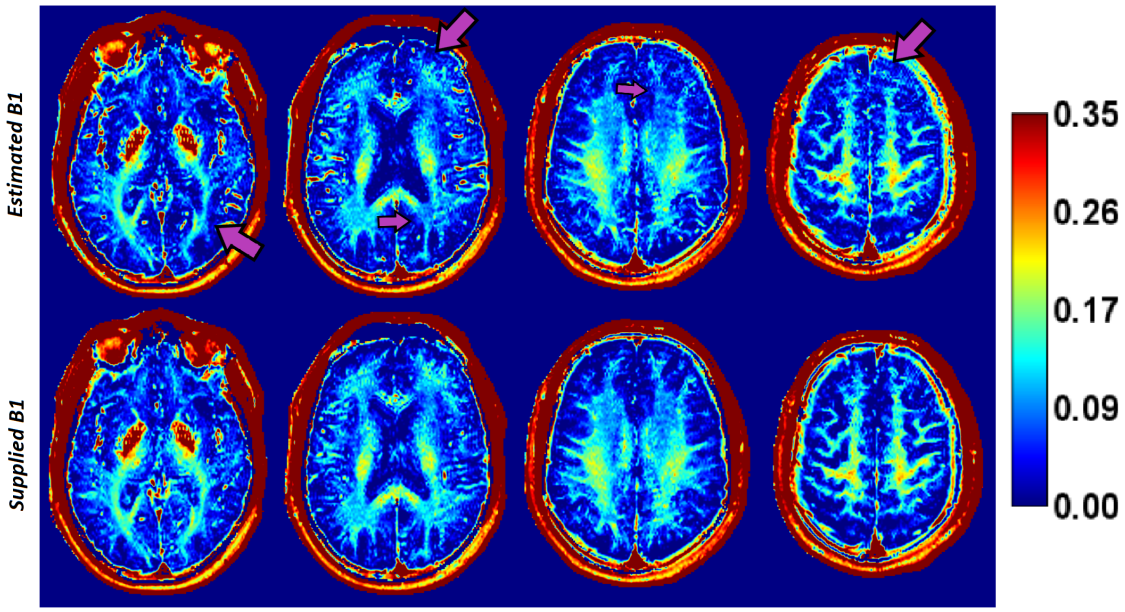

Figure 3.7: MWF maps using estimated $B_1{}^+$ values (top row) and reference $B_1{}^+$ values from an independent map(bottom row). Results are from a single subject. Purple arrows point to the areas where we observe improvements when supplying the $B_1{}^+$ values from the reference map.

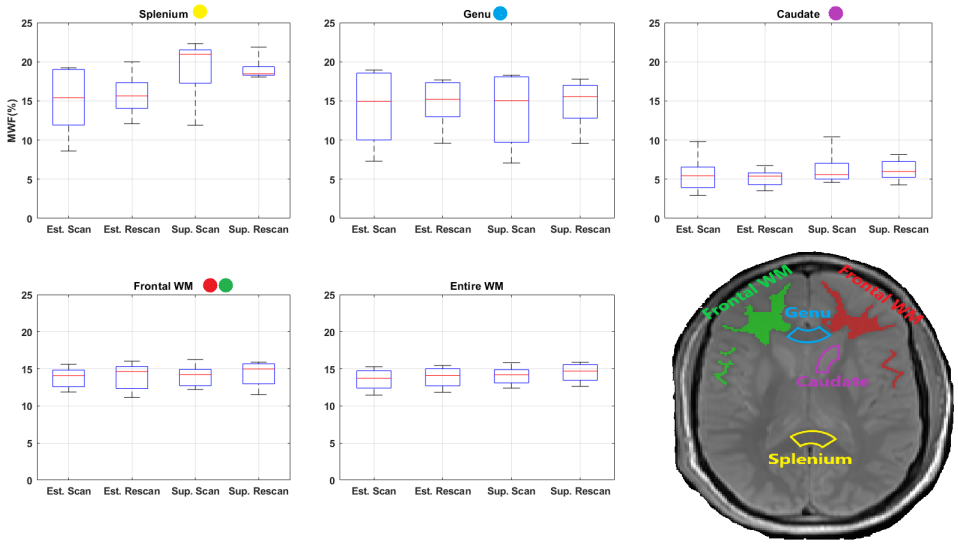

Figure 3.8: Box plots of the mean MWF over each ROIs. Scan and rescan data-sets were considered independent in the course of plotting. MWF values are displayed in percentage. The axial magnitude image shows the general placement of segmented ROIs. The prefixes "Est." and "Sup." denote the estimated and supplied $B_1{}^+$ methods, respectively.

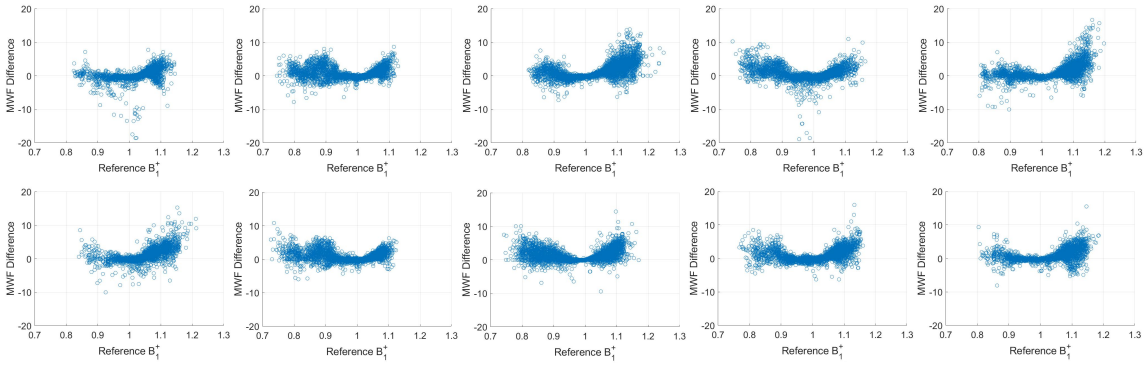

Figure 3.9: Scatter plot of the reference $B_1{}^+$ values versus MWF difference of the two methods (supplied $B_1{}^+$ minus estimated $B_1{}^+$ results) of all subjects. The first row is the scan and the second row is the rescan of each subject respectively. Three central slices of each subject were used for these plots.

reduced error possibly due to the more easily distinguishable patterns that diverge from the decay curves generated from the $B_1{}^+$ values around 1. $B_1{}^+$ estimation in the in-vivo data resulted in somewhat smooth maps, where most of the estimations were around one. Comparing to the reference $B_1{}^+$ map most voxels were underestimated and the MWF differences of the two methods were in alignment with the simulation results (Figure 3.5). Relatively large $B_1{}^+$ values ($B_1{}^+ > 1.05$) were underestimated to the values under $B_1{}^+ = 1$, which resulted in smaller MWF values compared to the reference $B_1{}^+$ values. The misestimations could be easily understood when looking at Figure 3.2.B where symmetrical values around 1 result in very similar decay patterns. Supplying the $B_1{}^+$ maps showed improvements in the MWF maps and there was a significant difference in the mean MWF estimation of the WM region using the paired t-test (p-value < 0.005). The difference $B_1{}^+$ map in the in-vivo data illustrates large regions of B1 mismatch which could not be solved by further smoothing. Extreme MWF values in the estimated $B_1{}^+$ method suggest that $B_1{}^+$ estimation fails where there are sharp transitions in the magnitude image.

McPhee and Wilman in 2015 [62] showed the benefits of using $B_1{}^+$ from an independent map for single component T_2 fitting from 2D MESE, where simultaneous fitting of the T_2 and $B_1{}^+$ was found to be insufficient in some cases. With only 3 unknowns

per voxel (So, T_2 and $B_1{}^+$), an independent $B_1{}^+$ map would reduce the unknowns by one-third, thus it is not surprising that single component fitting can benefit. However, multi-component fitting is an order of magnitude more complex as one needs to fit for over 60 parameters per voxel (T_2 points in the distribution and $B_1{}^+$). Supplying the $B_1{}^+$ map, would only slightly reduce the number of unknowns; however, the $B_1{}^+$ is a critical parameter that is required for dictionary matrix generation. Our work showed notable improvements in the final MWF maps, particularly in areas with $B_1{}^+$ greater than 1. We have implemented a similar Bloch simulation for decay curve generation as Akhondi-Asl *et al.* [47] did in their 2016 paper, and the estimated $B_1{}^+$ maps are fairly similar and comparable. Their maps have the upper boundary of 1.05 which shows the same pattern of underestimation as in our generated $B_1{}^+$ estimates. The MWF maps are also very much comparable.

While the value of an independent $B_1{}^+$ map for MWF fitting has been demonstrated, the method does require an additional $B_1{}^+$ scan. Whole brain $B_1{}^+$ maps may be acquired in 40 s with adequate spatial resolution as used here. Recent methods suggest this acquisition time can be substantially reduced to as little as 10 seconds [63], which is trivial compared to the 10+ minutes for typical MWF scans. The accuracy of the supplied $B_1{}^+$ values are determined by the $B_1{}^+$ mapping sequence and the registration process. Due to the slow varying nature of $B_1{}^+$ values, any slight mis-registration is not that much of a concern.

In this work, we used a 2D MESE sequence rather than a 3D version. 3D MESE is an extremely slow sequence that is impractical for a large number of slices, without employing techniques such as compressed sensing [64]. Many groups use a 3D GRASE for faster imaging, however, this sequence mixes in gradient echoes and often echo shifting, which both can affect the true MWF results. Furthermore, 3D GRASE is not available on all scanners. However, 2D MESE also has many limitations including SAR, MT, and SNR. The number of slices acquired in a single TR is limited by SAR. Moreover, the incidental MT effects may also affect results. 2D methods must also

have adequate spacing between interleaved slices to limit cross-talk and reduce MT effects. 2D methods generally have reduced SNR and SNR has a major impact on the fitting process. We used 3 averages to increase the SNR levels to ∼300 and the results are within the acceptable range with plausible tract definitions.

In conclusion, directly supplying the B_1^+ value to the fitting process via a B_1^+ map can avoid noise and artifacts in the MESE images which could affect the B_1^+ optimization/estimation step, and removes one parameter from the fitting procedure to attain more reliable solutions.

References

[14] K. C. McPhee, "Relaxometry in the Human Brain Using High Field MRI," Ph.D. dissertation, University of Alberta, 2017.

[23] K. P. Whittall, A. L. Mackay, D. A. Graeb, R. A. Nugent, D. K. B. Li, and D. W. Paty, "In vivo measurement of t2 distributions and water contents in normal human brain," *Magnetic Resonance in Medicine*, vol. 37, no. 1, pp. 34–43, 1997. DOI: 10.1002/mrm.1910370107.

[24] T. Prasloski, A. Rauscher, A. L. MacKay, M. Hodgson, I. M. Vavasour, C. Laule, and B. Mädler, "Rapid whole cerebrum myelin water imaging using a 3d grase sequence," *NeuroImage*, vol. 63, no. 1, pp. 533 –539, 2012, ISSN: 1053-8119. DOI: 10.1016/j.neuroimage.2012.06.064.

[26] T. Prasloski, B. Mädler, Q.-S. Xiang, A. MacKay, and C. Jones, "Applications of stimulated echo correction to multicomponent t2 analysis," *Magnetic Resonance in Medicine*, vol. 67, no. 6, pp. 1803–1814, 2012. DOI: 10.1002/mrm.23157.

[30] V. Wiggermann, I. M. Vavasour, S. Kolind, A. L. MacKay, G. Helms, and A. Rauscher, "Non-negative least squares computation for in vivo myelin mapping using simulated multi-echo spin-echo t2 decay data," *NMR in Biomedicine*, vol. 33, no. 12, e4277, 2020.

[37] G. F. Piredda, T. Hilbert, E. J. Canales-Rodríguez, M. Pizzolato, C. von Deuster, R. Meuli, J. Pfeuffer, A. Daducci, J.-P. Thiran, and T. Kober, "Fast and high-resolution myelin water imaging: Accelerating multi-echo grase with caipirinha," *Magnetic Resonance in Medicine*, vol. 85, no. 1, pp. 209–222, 2021.

[47] A. Akhondi-Asl, O. Afacan, M. Balasubramanian, R. V. Mulkern, and S. K. Warfield, "Fast myelin water fraction estimation using 2d multislice cpmg," *Magnetic resonance in medicine*, vol. 76, no. 4, pp. 1301–1313, 2016.

[48] G. S. Drenthen, W. H. Backes, A. P. Aldenkamp, G. J. Op't Veld, and J. F. Jansen, "A new analysis approach for t2 relaxometry myelin water quantification: Orthogonal matching pursuit," *Magnetic resonance in medicine*, vol. 81, no. 5, pp. 3292–3303, 2019.

[61] N. Ben-Eliezer, D. K. Sodickson, and K. T. Block, "Rapid and accurate t2 mapping from multi–spin-echo data using bloch-simulation-based reconstruction," *Magnetic resonance in medicine*, vol. 73, no. 2, pp. 809–817, 2015.

[62] K. C. McPhee and A. H. Wilman, "T2 quantification from only proton density and t2-weighted mri by modeling actual refocusing angles," *NeuroImage*, vol. 118, pp. 642–650, 2015.

[63] A. Lesch, M. Schlöegl, M. Holler, K. Bredies, and R. Stollberger, "Ultrafast 3d bloch–siegert b-mapping using variational modeling," *Magnetic resonance in medicine*, vol. 81, no. 2, pp. 881–892, 2019.

[64] A. V. Dvorak, V. Wiggermann, G. Gilbert, I. M. Vavasour, E. L. MacMillan, L. Barlow, N. Wiley, P. Kozlowski, A. L. MacKay, A. Rauscher, *et al.*, "Multi-spin echo t2 relaxation imaging with compressed sensing (metrics) for rapid myelin water imaging," *Magnetic resonance in medicine*, vol. 84, no. 3, pp. 1264–1279, 2020.

Chapter 4

Implementation of Multi-Echo Gradient Recalled Echo

4.1 Introduction

In this chapter, a multiple echo gradient echo (ME-GRE) sequence is implemented for myelin water imaging at 3T. Current models for data analysis are implemented that consider magnitude only or magnitude and frequency multi-component model. A recently introduced form of nonlocal filter is then applied to the MWI results and examined both in simulations and human brain experiments.

ME-GRE sequences have been tried in both 2D and 3D configurations for MWI analysis [4, 8, 32–35, 65]. 3D imaging sequences have an SNR advantage compared to 2D acquisitions and also the magnetization transfer (MT) effects are not of any concern. However, 3D acquisition suffers more from slice-select aliasing effects, and is more susceptible to motion artifacts; moreover, T_1 weighted biases due to using reduced repetition times make 3D results harder to compare and analyze [5, 8, 35]. To cut down on acquisition time in the 3D ME-GRE, one needs to use smaller repetition times ($\sim 60ms$) [35] and since there are significant differences between the T_1 values of water compartments, excitation flip angle must be chosen accordingly. One could choose a properly optimized flip angle to maximize the myelin water signal to increase the SNR of the MW compartment; this obviously leads to MWF overestimations due to suppression of other components with longer T_1. On the other hand, in 2D acqui-

sitions, TR is commonly appointed to a large enough value to avoid such T_1 weighted biases. Incidental MT effects from off-resonant slices can be mitigated by using long TRs and low power RF [66]. Moreover, there are no aliasing artifacts, shorter acquisition time, and fewer motion artifacts compared to 3D acquisition. In this work, we solely use the 2D ME-GRE sequence for acquisitions.

There are also other parameters to consider including echo spacing, number of echoes, and bipolar or mono-polar readout type. Shorter echo spacing would result in better temporal efficacy of MW signal, meaning there would be more echoes where MW signal is available in the signal decay. Alas, the hardware considerations restrain this parameter due to limits on gradient switching to minimize nerve stimulation, as well as SNR limits on exceedingly high BW. Echo spacing is also affected by the type of the readout gradient (monopolar or bipolar). Bipolar readout results in shorter echo-spacing, but rapid gradient polarity changes in bipolar acquisition induces magnitude and phase modulations between odd and even echoes [33, 35] which introduces notable artifacts in the final MWI analysis. To overcome this modulation, some have tried to register odd and even echoes [33], and recently an interesting gradient pairing sequence has been introduced by Shin *et al.* [35]. They propose to acquire two measurements of each line in the k-space which the polarities have reversed for the second one (20 echoes in total). Then calculate the final image using the two complex image which shows promising improvements in the final MWI analyses.

After the image acquisition, a data preparation/refinement step before the application of MWI analysis is common. This refinement usually consists of filtering the 4-dimensional data set (3 spatial dimensions and the 4th is echo time). Low pass filtering is common practice. Anisotropic diffusion filtering (ADF) has also been used which assumes magnitude gradients in each region of the brain remain constant and filters on a local basis [32]. There is also the potential of using nonlocal filters on ME-GRE data to increase SNR. Non-local filters use multi-spectral images which are defined as images taken at different flip angles, different echo times, etc. The advan-

tage of non-local filters is that they don't use proximity as the criterion of selection of similar voxels. The problem with using proximity as the selection criterion is twofold: First, one needs to choose a local kernel and thus limits the number of incorporated in the filtering process. Second is the inclusion of dissimilar voxels, especially near the borders of each region which results in blurring the image. A recently introduced non-local filter called nonlocal estimation of multi-spectral magnitudes (NESMA) has shown promising results in de-noising MR images [67]. However, in the original paper, they have not studied the effects of this filter on parameter estimation. One needs to investigate what is the cost of gaining SNR.

A second step before data analysis is managing local field gradient effects, which are one of the main artifacts in ME-GRE MWI, especially present near tissue-air interfaces. Therefore, there have been notable attempts at modeling it and compensating for this artifact. Alonso-Ortiz *et al.* [68], introduced an iterative method to fit for local field gradient in the slice direction assuming there is negligible loss due to in-plane gradients. They find initial values for the slice direction gradient from the first few echoes and assume later echoes contain a single water compartment decay. Then employing an NLLS algorithm try to fit for T_2^* and G_z at the same time. The other more complex approach is the voxel spread function introduced by Yablonskiy *et al.* [69] which tries to model the response of the macroscopic local field difference more accurately and reverse the effects. One group has even tried incorporating local tissue susceptibility [65], which has not been adopted by other groups. Most common practices adopt the simple first order LFG estimation or implementing VSF in the slice direction [70]. However, recent trends show that incorporating this parameter in the model in order to fit an extra parameter could also be beneficial. These kinds of literature usually assume that LFG effects can be modeled via a single sinc function, thus fitting for an extra parameter would be better than just using the values of the data preparation step, assuming the fit is insufficient due to inaccurate modeling [35]. For the MWI analysis, one must choose a model for fitting for signal decay curves,

as we know from analyses of MESE data ignoring a simple parameter would result in notable differences in the results. A lot of literature that have chosen the three pool models for 3T and four pool models and fit using the NLLS algorithm [32, 33, 35, 71]. However, there are several studies that use the same NNLS approach [5, 34, 68] but fit for an actual T_2^* distribution which is predicated on the assumption that frequency shifts if the water compartments at 3T is negligible.

4.2 Methods

4.2.1 LFG Correction

To calculate local field gradients, one needs to acquire local field shifts (ΔB_0) first. There are several ways: fitting a line to unwrap phase of each voxel, simply using the difference of a couple of later echoes in the train (as the short T_2^* water component has dissipated), or use the first steps of QSM processing code. Here, we used the simple process of using the phase of two adjacent echoes to estimate local field shifts by using the following equation:

$$G_z(r,z) = arg[S(r,z,TE_1)S^*(r,z,TE_2)S^*(r,z+\delta z,TE_1)S(r,z+\delta z,TE_2)]/(\gamma \delta z \Delta TE) \tag{4.1}$$

Where G_z is the gradient in the z direction, r is in-plane coordinates of a voxel, δz is the distance between two slices, ΔTE is the difference of echo times, TE_i is the echo time with its corresponding index, the symbol arg denotes the operation of taking the angle (rad) of a complex value, $S(.)$ denotes the signal at the given coordinate and time, and gamma is the gyromagnetic ratio. Using this equation one does not even need to unwrap the phase images. Finally, after estimating the local gradients, we calculate the magnitude modulation by the following equation:

$$S(t) = S_0(t) \cdot sinc(\gamma G_z \frac{\Delta Z}{2} t) \tag{4.2}$$

A simple division would result in the intended compensation. There is the possibility that the *sinc* function reaches zero where there is strong LFG present with long echo trains. In such scenarios, one can use the echoes before the *sinc* function reaches zero and compensate for the modulation or incorporate the *sinc* function in the model. Note that only the z-direction is considered since the z-dimension has the largest voxel size and also the strongest gradients for brain regions above the sinuses.

4.2.2 Non-local Filtering with NESMA

The assumption is that data consists of a multi-spectral (here multi-echo) set of images S defined on a discrete grid with the following Rician-distributed conditional probability density function [67]:

$$P(S_k|A_k,\sigma) = \frac{S_k}{\sigma^2} exp(-\frac{S_k^2 + A_k^2}{2\sigma^2}) \cdot I_0(\frac{S_k A_k}{\sigma^2}) \tag{4.3}$$

Where S_k denotes the signal intensity measured at the spectral image k, A_k is true signal intensity, sigma is the standard deviation of the noise, and I_0 is zeroth order Bessel function. The images include background regions where one can estimate the standard deviation of the noise, and it is assumed that the noise is stationary and σ remains constant throughout S.

The criterion to acquire similar voxels here is relative Euclidian distance (RED):

$$RED(i,j) = \frac{\sum_{k=1}^{K}(S_k(i) - S_k(j))^2}{\sum_{k=1}^{K} S_k^2(i)} \tag{4.4}$$

Choosing RED as the relative distance on top of being easy to implement and relatively fast to calculate, simplifies further equations for calculating the correct threshold levels. In order to set threshold levels, one needs to consider sources of relative distance. The first source is additive noise. Since we have large SNR in the MWI sequence one can assume the noise to be white Gaussian noise. Now, let's

calculate the expected value of relative distance when the voxels contain the same signal but different noise realization:

$$S_1(t) = A(t) + n_1(t) \tag{4.5}$$

$$S_2(t) = A(t) + n_2(t) \tag{4.6}$$

$$E\{RED(S_1, S_2)\} = 2(\frac{m \times \sigma_n}{\sum_{i=1}^{m} A_i^2}) \tag{4.7}$$

If we assume SNR to be:

$$SNR = \frac{A}{\sigma_n} \tag{4.8}$$

Then we would have:

$$E\{RED(S_1, S_2)\} \approx \frac{2}{(SNR)^2} \tag{4.9}$$

Now, let's consider the other source of difference which are the compartment specific parameters (relaxations, frequency shift, and relative amplitudes). This certainly elevates the level of complexity when it comes to setting a threshold. How we determine the threshold decides the margin error that we are accepting in the process of filtering. In order to simplify the process of calculating the margin of error one needs to sweep over a range of parameters in order to optimize for a threshold that results on an acceptable margin of error and when comparing to the noise levels would be plausible compared to the expected value of RED. Since we are doing MWI analysis most important parameter should be the margin of error in the MWF. Therefore, we decided our margin for error would be 1% of MWF difference between the two signal decay and in order to calculate the acceptable difference that would result in an RED

within the margin, we did a parameter sweep over the range of parameters in the two pool model (as the focus here is 3 Tesla data, one can recalculate for other models as well) to calculate the minimum RED with the maximum range of margin error which is 1% MWF difference. One needs to consider that signal levels drop as we reach later echoes so here we only used the first 12 echoes ($\sim 34ms$) to calculate the threshold of accepted error in order to have high enough SNR levels.

4.2.3 Curve Fitting

For the curve fitting model, we used the complex three pool model and fit the magnitude data. It has been shown that fitting to the complex data shows improvements in calculating the MW compartment frequency shift but has negligible effects on MWF estimation [71]. The final model for fitting is brought here:

$$S(t) = |A_{my} \cdot e^{-(\frac{1}{T^*_{2my}} + i2\pi\Delta f_{my})t} + A_{ax} \cdot e^{-(\frac{1}{T^*_{2ax}} + i2\pi\Delta f_{ax})t} + A_{ex} \cdot e^{-(\frac{1}{T^*_{2ex}} + i2\pi\Delta f_{ex})t}| \tag{4.10}$$

$$= |A_{my} \cdot e^{-(\frac{1}{T^*_{2my}} + i2\pi\Delta f_{my-ex})t} + A_{ax} \cdot e^{-(\frac{1}{T^*_{2ax}} + i2\pi\Delta f_{ax-ex})t} + A_{ex} \cdot e^{-(\frac{1}{T^*_{2ex}})t}| \tag{4.11}$$

Where my, ax, and ex subscripts denote myelin, axonal, and extracellular water compartments, respectively. A is the relative amplitude of each compartment, $T_2{}^*$ is the relaxation parameter, and deltaf denotes the resonance frequency shift. Since we are using the magnitude of the signal one of the frequency shifts can be omitted as the reference, thus there would be 8 parameters in total. These parameters are fit through an iterative non-linear algorithm. In MATLAB there are two functions that provide this NNLS process "lsqcurvefit" and "lsqnonlin" which are basically the same function with different model or cost function definition (TolX =1e-8, TolFun =1e-8).

We also fitted a $T_2{}^*$ distribution using the same NNLS procedure applied for MESE data. We chose 60 logarithmically spaced relaxation parameters ranging from $1ms$

to 2*seconds* to generate exponential decay curves for the dictionary matrix. Then applied the following regularized cost function using the "lsqnonneg" function of MATLAB:

$$\chi^2 + \mu \sum_{j=1}^{M} s_j^2, \mu \geq 0 \tag{4.12}$$

$$1.02\chi_m in^2 \leq \chi^2 \leq 1.025\chi_m in^2 \tag{4.13}$$

Where χ^2 is the sum of squared residuals of the fit, μ is the regularization parameter, and s_j is the signal at the jth echo. MWF was calculated according to the following equation:

$$MWF = \sum_{T_{2min}^*}^{T_{2max}^*} \tag{4.14}$$

Where T_{2min}^* and T_{2min}^* were 1 ms and 25 ms, respectively.

4.2.4 Numerical Simulations

A 3D phantom using a modified Shepp-Logan test image was employed to generate a reference MWF map. $T_2{}^*$ of myelin water, axonal water, and extracellular water was respectively set to 10, 64, and 48 ms. The ratio of axonal water proportion to cellular water was set to two for the entire phantom. Frequency shifts were incorporated for MWF of 10% ($f_{my} = 15Hz, f_{ex} = 5$) and 5% ($f_{my} = -5Hz, f_{ex} = 1$). SNR was defined as the amplitude of the first echo divided by the standard deviation of the noise. For each voxel Rician distributed noise was realized with three different SNRs (100, 200, and 500). First echo time and echo spacing were both set to 2 ms and signal decay was simulated for 32 echoes in total. MWI analysis was done for 18, 26, and 32 echoes.

4.2.5 In-vivo Experiment

All in-vivo experiments were performed at 3T (Siemens Prisma) using 64 channel head receive coil. Data were collected from 5 healthy volunteers. We collected a 2D mono-polar readout gradient multi-echo gradient echo with 36 slices, slice thickness $3mm$, in-plane resolution $1.5 \times 1.5mm$, repetition time $2seconds$, first echo time $2.01ms$, echo spacing of $2.86ms$, echo train length 18 echoes, flip angle 85°, and distance factor 0% with interleaved slice acquisition configuration. The acquisition had one average taking 3 minutes and 45 seconds.

To check the effectiveness of a spatial saturation pulse on dampening the physiological noise arising from blood influx, we also conducted experiments with and without the saturation pulse for comparison. Data were collected using 18 echoes 2D mono-polar MEGRE with 16 slices, 50% distance factor, $230 \times 230mm$ FOV, 3mm slice thickness, 1.4×1.4 mm in-plane resolution, first echo time $2.01ms$, echo-spacing $2.86ms$, BW $600Hz/pixel$, and TR $2000ms$. Acquisition time was 4 minutes and saturation pulse was applied to a region of $100mm$ thickness below the slab of interest.

These scans were acquired within the same MRI session as the 2D MESE data in the previous chapter and the same ROIs were registered to the MEGRE data for a more comprehensive MWF comparison.

4.3 Results

4.3.1 Numerical Simulations

Using a modified Shepp-Logan test image, we generated a reference MWF map (Figure 4.1) to simulate an ME-GRE phantom based on the aforementioned parameters.

MWI analysis results are brought in (Figure 4.2). Single component fitting results are more robust to noise since we are fitting only a single parameter, but nevertheless, improvements can be observed when SNR levels elevate. Three-pool model seems to be highly affected by the noise, SNR of levels of 500 and 1000 show plausible MWF

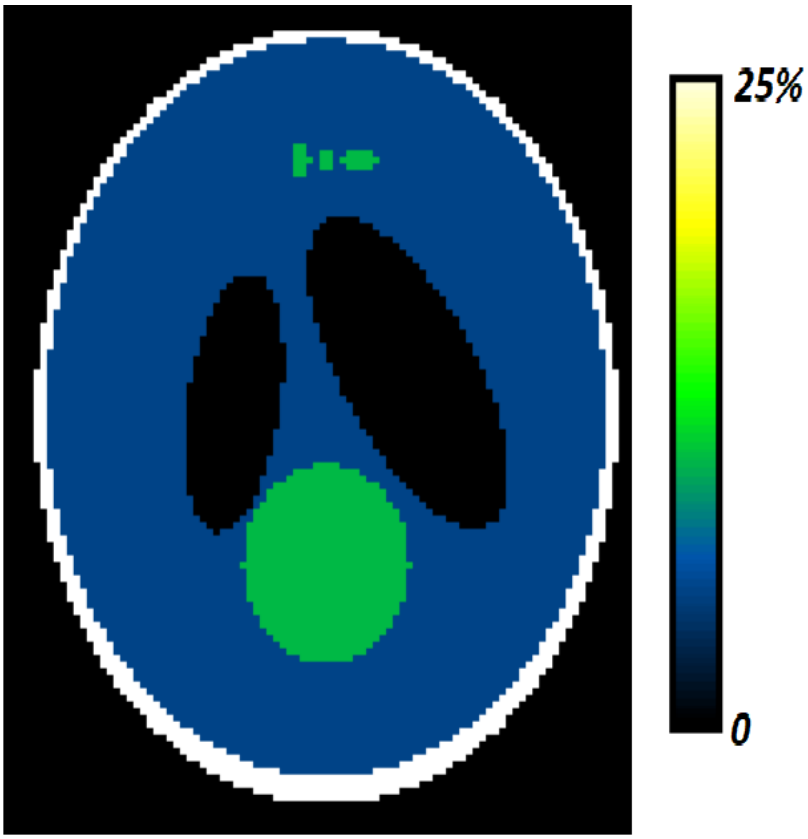

Figure 4.1: Reference MWF map using a modified Shepp-Logan test image. Values are 100%, 10%, 5%, and 10^{-5} %.

values which are qualitatively acceptable as well. The NNLS fit seems a bit more robust to noise, however, underestimated MWF values all around. Especially areas in which myelin water compartment has 15 Hz frequency shift, such that estimations completely fail.

4.3.2 In-vivo Experiment

The final results of the MWI analyses are brought in Figure 4.3. Underestimations of the T_2^* relaxation parameter in the top regions of the relaxation map is an indication of the local field inhomogeneity effects. There seem to be some left/right asymmetries in the single component fit. Three-pool model results look very noisy and LFG artifacts in the top regions are clearly visible. The NNLS fitting MWF maps look better than the three-pool model, but large artifacts are visible. The estimated SNR

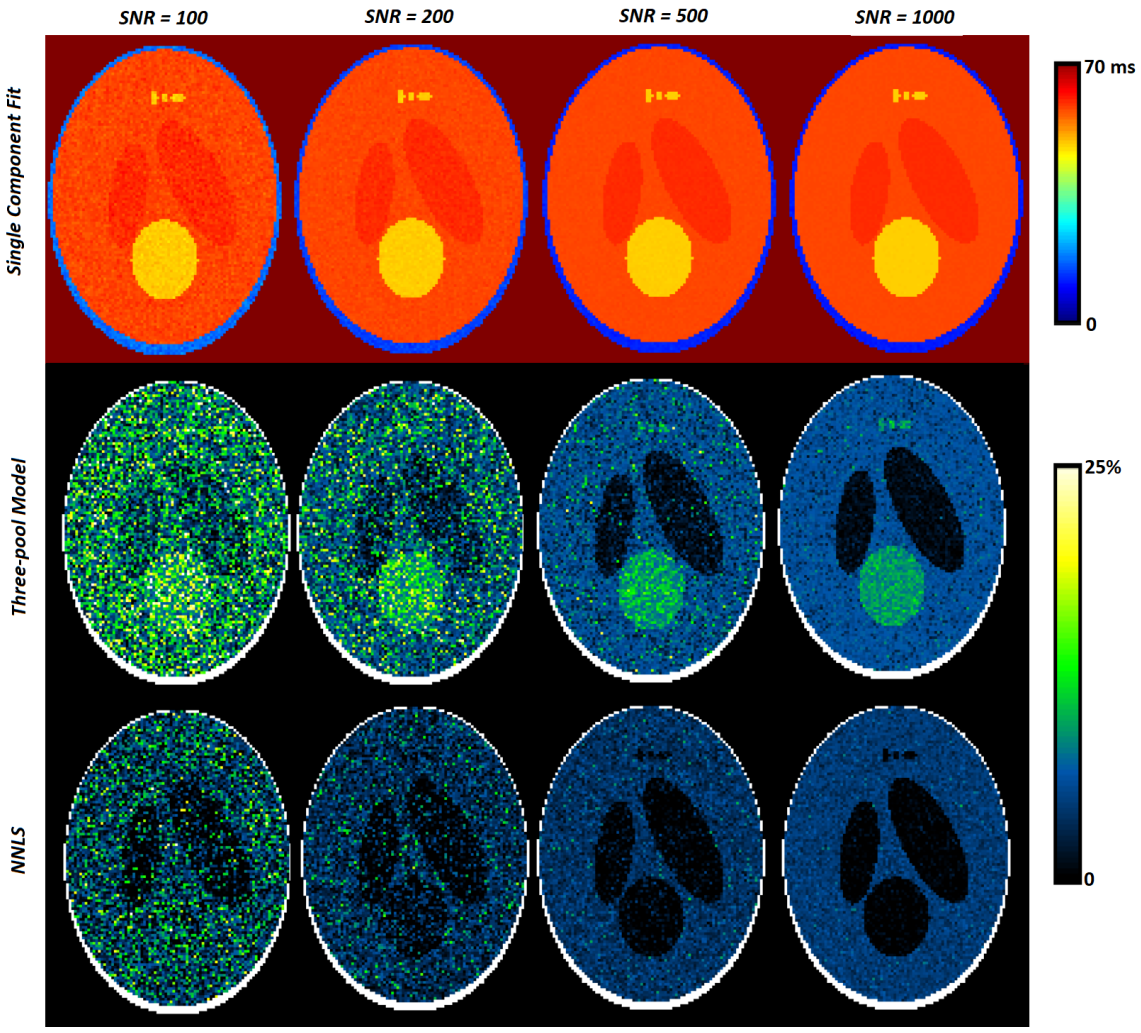

Figure 4.2: Numerical simulation results of the Shepp-Logan phantom. The first row is the single component fitting of the T_2^* relaxation parameter. The second row is the three-pool model MWF maps and the third row depicts the MWF maps using the NNLS fitting procedure.

of the in-vivo data was ~ 500.

Results after applying the NESMA filter are brought in Figure 4.4. The artifacts of the LFG have been omitted in the frontal regions of the brain and genu seems more consistent to the splenium of the corpus callosum. This effect can also be observed in the single component results, where using the original data we observe some underestimations in the frontal WM (Figure 4.3). MWF maps look much better with structural definitions even in deep gray matter. NNLS fit shows smaller MWF values overall, in alignment with numerical simulations.

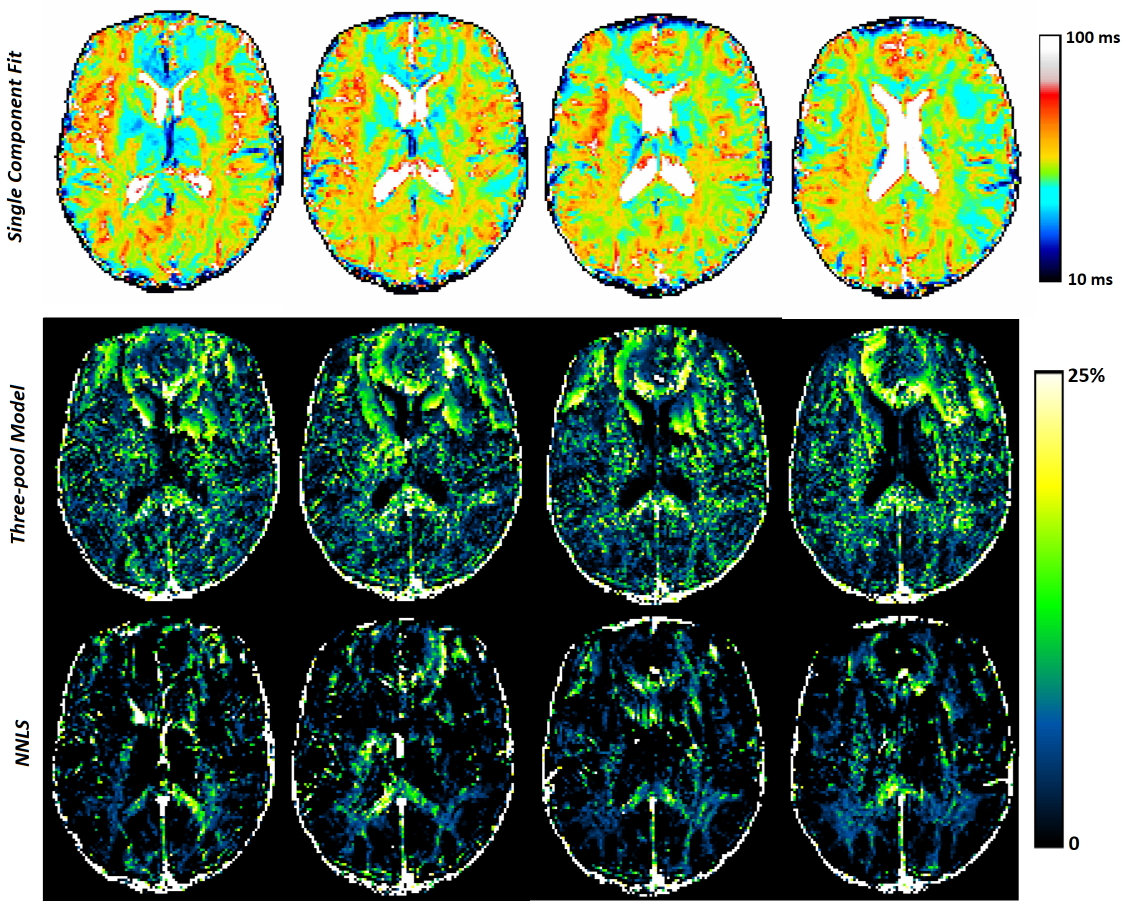

Figure 4.3: MWI analysis result of the 2D ME-GRE data. The first row is the single component fit of the T_2^* relaxation parameter, the second row is the three-pool model MWF maps, and the third is the NNLS fitting results.

Results of the saturation pulse experiment are illustrated in Figure 4.5. In the MWF of the data without saturation, we can clearly see underestimations in the final product of our analysis (*i.e.* MWF maps). There are also ripple-shaped artifacts observed in the MWF maps that emerge as a pattern of over and underestimations. Such patterns notably affect MWF estimation variability and decrease SNR of MEGRE data.

We used the 2D MESE MWF maps acquired using the supplied B1 values (same data as the previous chapter, Chapter 3) as our reference data and plotted the scatter plots of the 2D MEGRE MWFs versus the reference data. Two WM regions (Genu and Splenium of Corpus Callosum) and two GM territories (Caudate and Putamen)

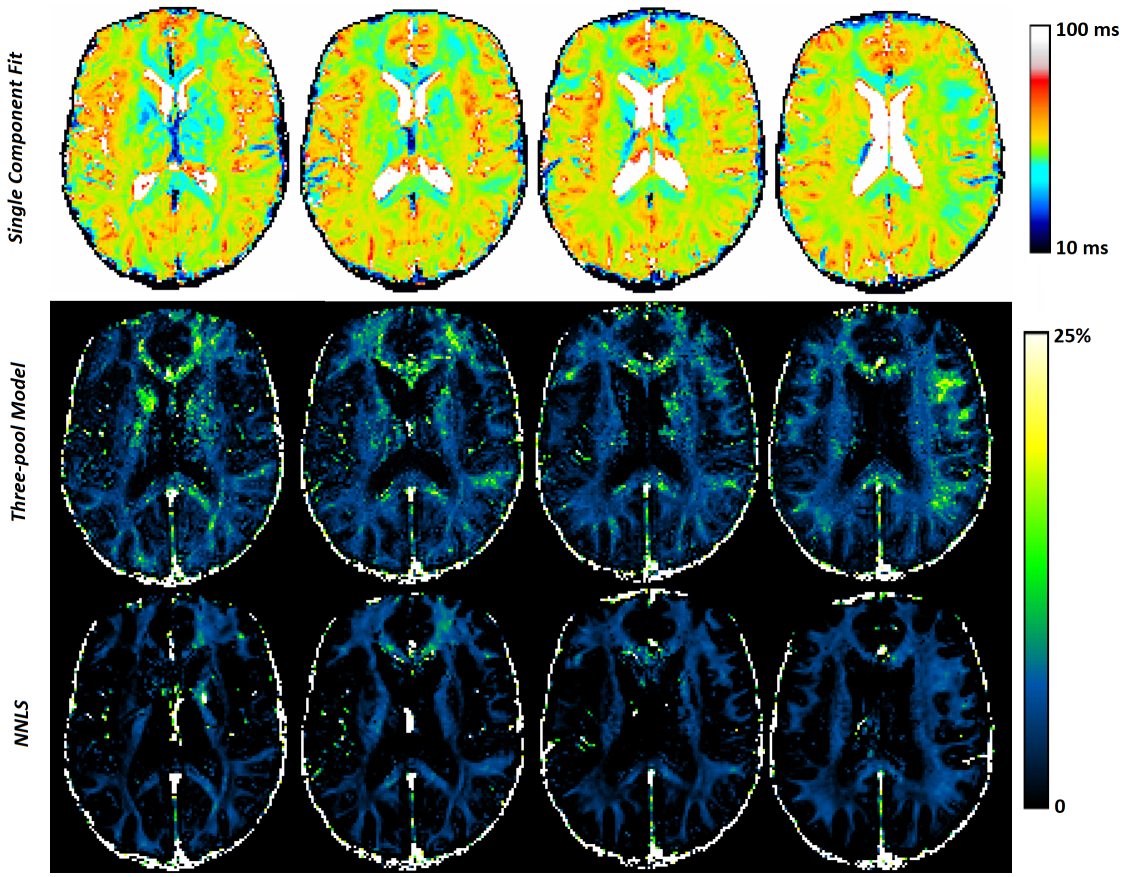

Figure 4.4: Fitting results after applying NESMA filter. Same data as Figure 4.3

were used to calculate mean MWFs for the scatter plots and used linear regression to fit a line to the data. Generally, three-pool model results show a stronger linear correlation with the reference method (Figure 4.6), and the strongest correlation was observed between NESMA filtered data using the three-pool model and the reference method (R = 0.75, p-value = 2e-8), and the normal NNLS data has the largest slope amongst all the scatter plots.

4.4 Discussion

Here we reviewed the general procedure that is used to perform MWI analysis on ME-GRE data. Simulation results showed that it is possible to find plausible MWF maps using the common methods for 2D MEGRE, but it requires high levels of SNR. We also proposed using a NESMA filter to overcome noise issues of the MEGRE

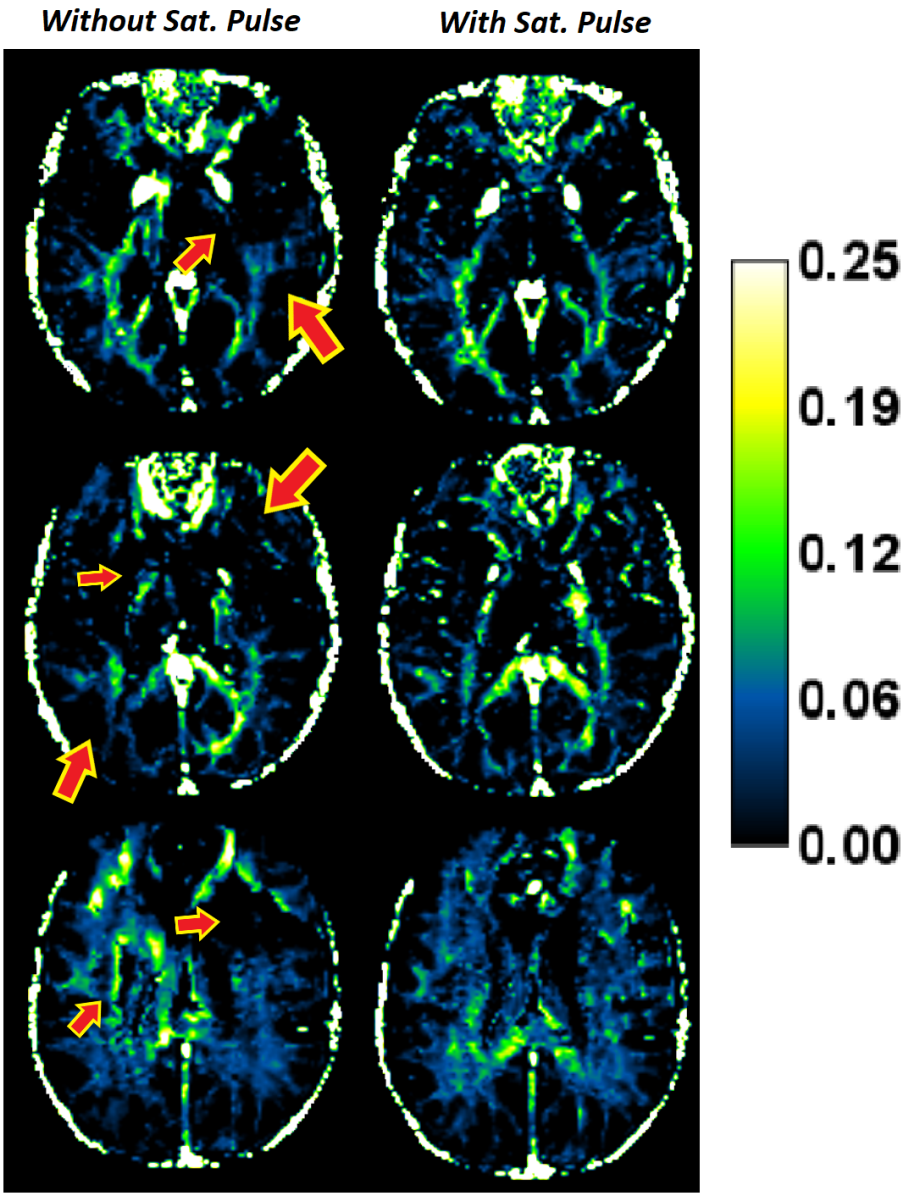

Figure 4.5: MWF maps with and without accounting for blood flow using the saturation pulse. The first column shows the MWF maps when there is no saturation pulse and the second one includes a saturation pulse in the acquisition process. MWF maps are acquired using the NNLS method. Red arrows point to the areas that we see notable improvements.

data and found that doing so would produce MWF maps with less artifact and with high correlation with our reference method, and single component fitting results also showed improvements.

Simulations showed using the regularized NNLS fitting is more robust to noise but

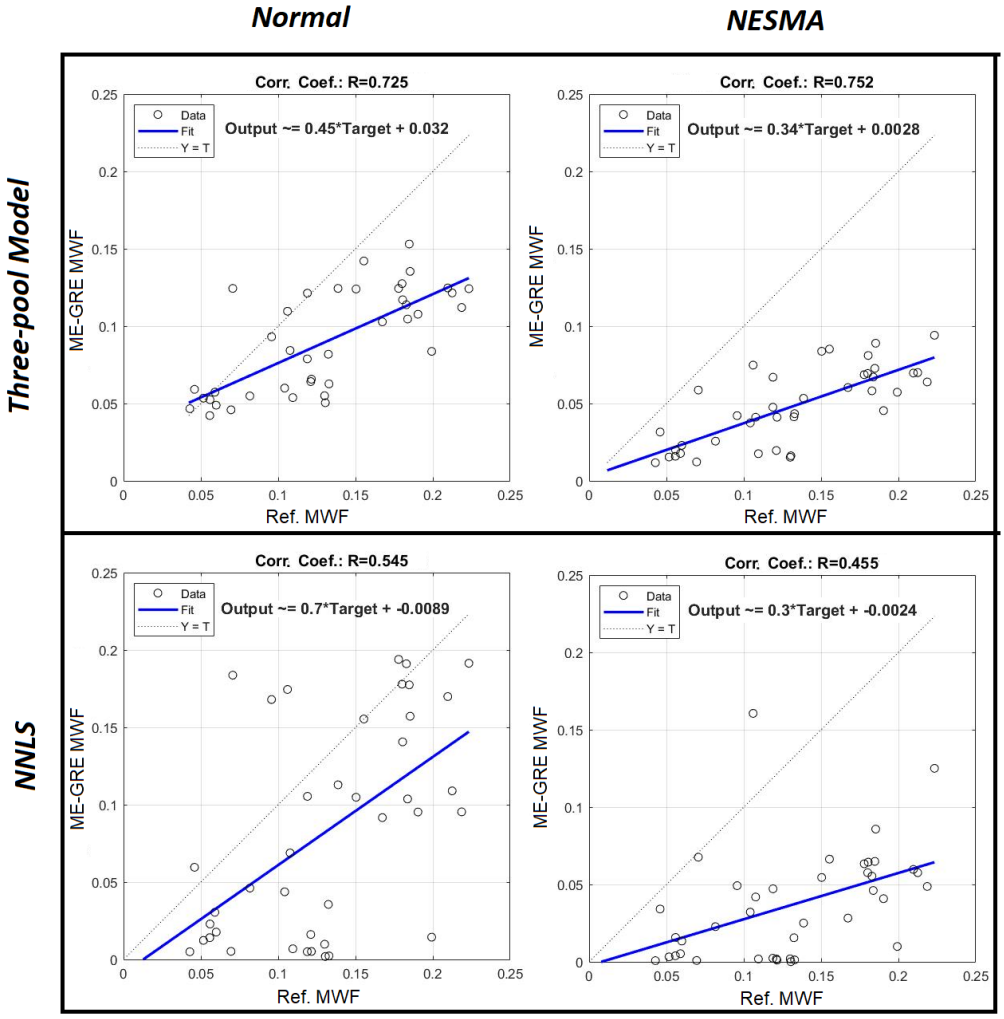

Figure 4.6: Scatter plots of the MEGRE MWFs versus the reference method (2D MESE using supplied B1 values) with fitted lines using linear regression. The target (x-axis) denotes the mean MWFs in each ROIs using the reference method and the output (y-axis) is the mean MWF in the MEGRE results. MWF from both methods (NNLS and 3PM) are shown with and without NESMA filter. $\boldsymbol{R}$ denotes the correlation coefficient of each scatter.

generally, underestimates MWF value compared to three-pool mode and where there are significant resonance frequency shifts ($> 10Hz$) between the water pools, the NNLS method cannot detect any MW signal. Comparing the MWF results with the reference method showed a higher correlation with three-pool models compared to the NNLS method; however, the NNLS method produced larger MWFs in the segmented ROIs which resulted in a higher slope when using linear regression between the results

and the reference method. It is possible that this method is working better in regions where the WM fibers are parallel to the B_0 field and starts to fail where there is a significant angle between the WM bundle and the main magnetic field; As literature suggests there would be notable resonance frequency shifts between water compartments in such regions [4, 70]. Therefore, we see some notable underestimation data points in the scatter plot.

Previous research done by Lee and colleagues [66] had shown advantages of employing a saturation pulse in the acquisition procedure to limit the effects of blood inflow, which here was reiterated and results showed improvements and were comparable to previous research. The observed improvements in our results were mostly qualitative and the quantitative comparison did not show any significant improvements in the results, as we average the results over a region and the artifacts start to disappear when averaged over a large enough region.

The NESMA method produces MWF maps with better quality (at least visually) and quantitatively produced data with higher precision and higher correlation with the reference method, however, these improvements come at a cost. There is a thresholding dilemma in that using a large value would result in blurring the image and a very small one would prevent the filter from performing to its full potential (by incorporating as many voxels as possible). The threshold here is set where the MWF difference of the various incorporated voxels would be less than 1% and was considered sufficient. However, this value was set on the naive assumption that there were no frequency shifts between the water compartments as it would make the threshold very complex. In order to incorporate the frequency shifts in the thresholding process, one can use a registered DTI image to estimate the frequency shifts and add it to the voxel similarity cost function. But, one needs to consider if using this method would actually be advantageous to other methods of noise reduction (*e.g.* acquiring more averages). Moreover, we observe a dramatic reduction of the slope of NNLS data compared to the reference data. This is in fact the major effect of our naive

assumption of little to no frequency shifts between the water compartments. This allows the amalgamation of voxels with and without frequency shifts that predominantly impact regularized NNLS method results.

Overall, the MEGRE method produced MWF maps which are comparable to their MESE based counterpart. The SNR problem of the MEGRE data is a major issue that needs to be addressed especially if one uses the three-pool model to perform the MWI analysis. Adopting a saturation pulse to limit the physiological noise seems a necessary step in the acquisition process which seems to come with no cost in the process, but one needs to be aware of possible MT effects. The 2D MEGRE sequence was fast and feasible, and the MT effects were minimized by using a long TR and a distance factor of 50% also further improved the quality of MWF maps. In short, we have implemented a starting point for the ME-GRE methods of MWF. Our main focus was the MESE methods of previous chapters.

References

[4] P. van Gelderen, J. A. de Zwart, J. Lee, P. Sati, D. S. Reich, and J. H. Duyn, "Nonexponential t2* decay in white matter," *Magnetic Resonance in Medicine*, vol. 67, no. 1, pp. 110–117, 2012. DOI: 10.1002/mrm.22990.

[5] E. Alonso-Ortiz, I. R. Levesque, and G. B. Pike, "Mri-based myelin water imaging: A technical review," *Magnetic Resonance in Medicine*, vol. 73, no. 1, pp. 70–81, 2015. DOI: 10.1002/mrm.25198.

[8] J. Lee, J.-W. Hyun, J. Lee, E.-J. Choi, H.-G. Shin, K. Min, Y. Nam, H. J. Kim, and S.-H. Oh, "So you want to image myelin using mri: An overview and practical guide for myelin water imaging," *Journal of Magnetic Resonance Imaging, Online ahead of print.*, vol. n/a, no. n/a, 2020 Feb 3. DOI: 10.1002/jmri.27059.

[32] D. Hwang, D.-H. Kim, and Y. P. Du, "In vivo multi-slice mapping of myelin water content using t2* decay," *NeuroImage*, vol. 52, no. 1, pp. 198 –204, 2010, ISSN: 1053-8119. DOI: 10.1016/j.neuroimage.2010.04.023.

[33] Y. P. Du, R. Chu, D. Hwang, M. S. Brown, B. K. Kleinschmidt-DeMasters, D. Singel, and J. H. Simon, "Fast multislice mapping of the myelin water fraction using multicompartment analysis of t decay at 3t: A preliminary postmortem study," *Magnetic Resonance in Medicine*, vol. 58, no. 5, pp. 865–870, 2007. DOI: 10.1002/mrm.21409.

[34] E. Alonso-Ortiz, I. R. Levesque, and G. B. Pike, "Multi-gradient-echo myelin water fraction imaging: Comparison to the multi-echo-spin-echo technique," *Magnetic Resonance in Medicine*, vol. 79, no. 3, pp. 1439–1446, 2018. DOI: 10.1002/mrm.26809.

[35] H.-G. Shin, S.-H. Oh, M. Fukunaga, Y. Nam, D. Lee, W. Jung, M. Jo, S. Ji, J. Y. Choi, and J. Lee, "Advances in gradient echo myelin water imaging at 3t and 7t," *NeuroImage*, vol. 188, pp. 835 –844, 2019, ISSN: 1053-8119. DOI: 10.1016/j.neuroimage.2018.11.040.

[65] Z. Wu, H. He, Y. Sun, Y. Du, and J. Zhong, "High resolution myelin water imaging incorporating local tissue susceptibility analysis," *Magnetic Resonance Imaging*, vol. 42, pp. 107 –113, 2017, ISSN: 0730-725X. DOI: 10.1016/j.mri.2017.06.005.

[66] J. Lee, Y. Nam, J. Y. Choi, E. Y. Kim, S.-H. Oh, and D.-H. Kim, "Mechanisms of t2* anisotropy and gradient echo myelin water imaging," *NMR in Biomedicine*, vol. 30, no. 4, e3513, 2017. DOI: 10.1002/nbm.3513.

[67] M. Bouhrara, M. C. Maring, and R. G. Spencer, "A simple and fast adaptive nonlocal multispectral filtering algorithm for efficient noise reduction in magnetic resonance imaging," *Magnetic resonance imaging*, vol. 55, pp. 133–139, 2019.

[68] E. Alonso-Ortiz, I. R. Levesque, R. Paquin, and G. B. Pike, "Field inhomogeneity correction for gradient echo myelin water fraction imaging," *Magnetic Resonance in Medicine*, vol. 78, no. 1, pp. 49–57, 2017. DOI: 10.1002/mrm.26334.

[69] D. A. Yablonskiy, A. L. Sukstanskii, J. Luo, and X. Wang, "Voxel spread function method for correction of magnetic field inhomogeneity effects in quantitative gradient-echo-based mri," *Magnetic Resonance in Medicine*, vol. 70, no. 5, pp. 1283–1292, 2013. DOI: 10.1002/mrm.24585.

[70] H. Lee, Y. Nam, H.-J. Lee, J.-J. Hsu, R. G. Henry, and D.-H. Kim, "Improved three-dimensional multi-echo gradient echo based myelin water fraction mapping with phase related artifact correction," *NeuroImage*, vol. 169, pp. 1–10, 2018.

[71] Y. Nam, J. Lee, D. Hwang, and D.-H. Kim, "Improved estimation of myelin water fraction using complex model fitting," *NeuroImage*, vol. 116, pp. 214–221, 2015.

Chapter 5

Conclusions, Limitations, & Future Directions

5.1 Summary of Findings

It has been more than 25 years since the in-vivo visualization of myelin water using multi-component analysis of multi-echo data has been introduced [19]. The aforementioned article has sparked a notable train of studies in the field which is called MWI. Some have introduced creative solutions to facilitate using the same principles to apply for MWI analysis with alternate sequences to overcome issues dealing with the shortcomings of the original method [24, 26, 33, 47]. These contributions in turn spawned quite a few studies to deal with the challenges of alternative solutions. The 3D GRASE sequence was introduced to tackle the slow timings of the CPMG sequence [72] which itself introduced the challenge of dealing with stimulated echoes. Prasloski *et al.* in their 2012 paper introduced an optimization method to estimate local flip angles to enable using 3D methods which led to quite a few studies to investigate the feasibility of this solution [30] and even the constraining of this flip angle parameter [50]. In Chapter 2, we investigated the benefits of constraining the flip angle parameter in the fitting process and determined not only are there notable improvements when constraining this parameter using an alternate mapping method, but also the optimization method in the in-vivo data would be biased and skewed in the outcome of estimation due to the presence of artifacts. This observation spiked

the idea to investigate the same effect in 2D MESE data, where the signal generation is much more complex, owing to slice profile effects across the voxel. In Chapter 3, we tried to replicate the full Bloch simulation as suggested in previous literature [47], and detected that the optimization method in the 2D data has even stronger effects/error and since 2D sequences have smaller SNR compared to 3D, the estimated $B_1{}^+$ maps showed stronger deviations when compared to the reference map.

In Chapter 4, we reiterated the common procedures that are being used in the ME-GRE methods for MWI. These methods seemed less reliable as there were quite a few issues with the final MWF maps. The low SNR of MEGRE data resulted in very noisy maps which were dependent on the methods/models that we used. The three-pool model resulted in larger MWF values, but maps had poor image quality and variations within similar WM regions were large. The regularized NNLS method produced somewhat better-looking maps with less variation due to the incorporation of regularization. However, this method does not incorporate the resonance frequency shifts of the water compartments, therefore we observed underestimations in the final MWF maps. Simulations agreed with our findings, where there was a significant frequency shift incorporated in the signal generation NNLS method resulted in little to no MWF value (where in fact there was a significant MW signal in the simulated decay curve). We addressed the SNR issue of the ME-GRE sequences by employing a nonlocal filter called NESMA. The MWF maps had much better image quality after the application of NESMA and analysis showed that the correlation of MWF values with the reference method increases when using this approach.

5.2 Limitations

MWI methods come with many challenges relating to the analysis itself and to the pulse sequences used. The SAR limit is one of the issues of the MESE sequences, particularly for interleaved 2D MESE. In the 2D sequence, SAR limits the number of slices that are excited during a single TR. The trade-off seems to affect the total ac-

quisition time as well, which makes parameter tuning a bit more complex. Moreover, if we put a constraint on acquisition time, it would translate to limiting the number of slices; and therefore, preventing a whole brain acquisition.

A second limitation of MESE sequences is $B_1{}^+$ inhomogeneity across the brain, leading to different flip angles in different regions. For example, the presence of $B_1{}^+$ inhomogeneities results in a higher flip angle in the middle of the brain than the edges due to RF interference. Effects from these variations can be minimized by measuring the $B_1{}^+$ map.

Even though regularizations are used to achieve better robustness against noise, SNR is still a major factor in the quality of MWI results. Previous literature has concluded that the NNLS method requires an SNR of more than 700 (for $\Delta TE = 10ms$ and $N_{echoes} = 32$) to produce reliable results [53]. 3D MESE sequence would achieve this level of SNR, but it requires a long acquisition time, and the common substitute 3D GRASE does not meet the SNR requirement. 2D MESE has the same issue with SNR and one needs to acquire multiple averages. Some have tried increasing the number of echoes (up to 64) [30] and decreasing the echo spacing (down to 9ms) [47], alas the effects/improvements are not that notable to overcome the SNR requirement.

Another challenge of the MWI analysis is the limited spatial resolution. This is directly entangled with the SNR and the acquisition time. With a typical goal being substantial brain coverage, voxel dimensions are strongly limited by the available scan time. For example, a long acquisition of 13 min was used for 3D GRASE for MWI, but only achieved a voxel dimension of $1.5 \times 1.5 \times 5mm3$. Certainly, the potential diagnostic utility of MWI is limited to large regions and fine features such as demyelination at lesion edges cannot be measured.

The MEGRE methods have even smaller SNR levels (compared to MESE sequences), and other effects such as B_0 inhomogeneities and physiological noise sources exacerbate the quality of MWI analysis results. Using higher fields (7 Tesla) helps with the SNR [8, 35]and even makes spine MWI analysis possible with plausible resolutions,

but higher fields come with greater effects of physiological motion and susceptibility effects from air-tissue interfaces that increase dramatically with the field. The B_0 inhomogeneity effects must be carefully compensated using accurate models; for example, the voxel spread function introduced by Yablonskiy *et al.* (2013) [69] seems like a proper solution but increases the post-processing computation time. One must always consider the application of proper shimming when acquiring MEGRE data. In the MEGRE sequences echo spacing and first echo time can be much smaller (compared to MESE counterparts) but they are limited by hardware and nerve stimulation due to fast gradient changes.

Our results showed that regularized NNLS methods that simply use exponential decays without incorporating any frequency shifts in their model, seems to fail when applied to MEGRE data where there are notable frequency shifts between water compartments; and multiple-pool models (NLLS) perform better as they include the frequency shifts in the parameter estimation process. However, the NLLS method seems to require higher levels of SNR even though seemingly there are fewer parameters to fit for. Moreover, the NLLS method could result in suboptimal solutions as in the fitting process gradients reach zero values in the local extremum of the fit, which makes final solutions very much dependable on initial values (our initial guess of parameters). Of course, the dependency on initial values could be overcome by employing a multi-seed approach, where we use multiple sets of initial values and choose the solution with the smallest residuals.

5.3 Future Directions

There is only so much that one can do in the parameter estimation side of the MWI analysis, but it would always come down to the acquisition side to provide large enough SNRs. Some have tried using deep learning methods to acquire faster MWI analysis [73]. However, there is the issue that such neural networks are trained using the same NNLS method that acquires the solution which makes the accuracy of such

approaches less than the classic solution. One could still try to use machine learning methods to train neural networks for the recon side, but in the author's opinion the only benefit would be faster computation time and perhaps the possibility of real-time MWI analysis.

Another major factor is the acquisition time of the sequence that directly affects the clinical feasibility of the analysis. Some have tried compressed sensing on 3D MESE to achieve more feasible timings for full brain scan [64] which seems a more plausible route to take when compared to 3D GRASE and its concerning artifacts. One could see the future of the field in the innovative sequence schemes that tackle the timing issue side and parameter estimation side at the same time. The resolution and the voxel sizes should also be considered and perhaps a 3D scheme that could acquire symmetrical resolution in all directions would be the optimal approach.

Multiple-pool models require initial guesses which directly affects the estimation results. One could try to constrain the initial values and even parameters by using an independent sequence. For example, one could try to use DTI images to constrain the resonant frequency shift parameters and investigate the aftermath.

There has not been enough focus on the characteristics of the myelin water compartment itself and usually, it is overshadowed by other interesting products like MWF. It could be beneficial to directly investigate and map the transverse relaxation parameter of myelin water. The regularization of the fitting procedure and the low SNR of MW signal hinders such investigations. One possible scheme would be to damp the other water compartments as it is done in the ViSTa sequence [74] and then acquire multiple echoes to enable attaining a T_2/T_2^* map of myelin water.

As well as technical advances in pulse sequence, the MWI methods can continue to be applied to demyelinating and remyelinating diseases like multiple sclerosis.

References

[8] J. Lee, J.-W. Hyun, J. Lee, E.-J. Choi, H.-G. Shin, K. Min, Y. Nam, H. J. Kim, and S.-H. Oh, "So you want to image myelin using mri: An overview and practical guide for myelin water imaging," *Journal of Magnetic Resonance Imaging, Online ahead of print.*, vol. n/a, no. n/a, 2020 Feb 3. DOI: 10.1002/jmri.27059.

[19] A. Mackay, K. Whittall, J. Adler, D. Li, D. Paty, and D. Graeb, "In vivo visualization of myelin water in brain by magnetic resonance," *Magnetic Resonance in Medicine*, vol. 31, no. 6, pp. 673–677, 1994. DOI: 10.1002/mrm.1910310614.

[24] T. Prasloski, A. Rauscher, A. L. MacKay, M. Hodgson, I. M. Vavasour, C. Laule, and B. Mädler, "Rapid whole cerebrum myelin water imaging using a 3d grase sequence," *NeuroImage*, vol. 63, no. 1, pp. 533 –539, 2012, ISSN: 1053-8119. DOI: 10.1016/j.neuroimage.2012.06.064.

[26] T. Prasloski, B. Mädler, Q.-S. Xiang, A. MacKay, and C. Jones, "Applications of stimulated echo correction to multicomponent t2 analysis," *Magnetic Resonance in Medicine*, vol. 67, no. 6, pp. 1803–1814, 2012. DOI: 10.1002/mrm.23157.

[30] V. Wiggermann, I. M. Vavasour, S. Kolind, A. L. MacKay, G. Helms, and A. Rauscher, "Non-negative least squares computation for in vivo myelin mapping using simulated multi-echo spin-echo t2 decay data," *NMR in Biomedicine*, vol. 33, no. 12, e4277, 2020.

[33] Y. P. Du, R. Chu, D. Hwang, M. S. Brown, B. K. Kleinschmidt-DeMasters, D. Singel, and J. H. Simon, "Fast multislice mapping of the myelin water fraction using multicompartment analysis of t decay at 3t: A preliminary postmortem study," *Magnetic Resonance in Medicine*, vol. 58, no. 5, pp. 865–870, 2007. DOI: 10.1002/mrm.21409.

[35] H.-G. Shin, S.-H. Oh, M. Fukunaga, Y. Nam, D. Lee, W. Jung, M. Jo, S. Ji, J. Y. Choi, and J. Lee, "Advances in gradient echo myelin water imaging at 3t and 7t," *NeuroImage*, vol. 188, pp. 835 –844, 2019, ISSN: 1053-8119. DOI: 10.1016/j.neuroimage.2018.11.040.

[47] A. Akhondi-Asl, O. Afacan, M. Balasubramanian, R. V. Mulkern, and S. K. Warfield, "Fast myelin water fraction estimation using 2d multislice cpmg," *Magnetic resonance in medicine*, vol. 76, no. 4, pp. 1301–1313, 2016.

[50] C. L. Lankford and M. D. Does, "Propagation of error from parameter constraints in quantitative mri: Example application of multiple spin echo t2 mapping," *Magnetic resonance in medicine*, vol. 79, no. 2, pp. 673–682, 2018.

[53] S. J. Graham, P. L. Stanchev, and M. J. Bronskill, "Criteria for analysis of multicomponent tissue t2 relaxation data," *Magnetic Resonance in Medicine*, vol. 35, no. 3, pp. 370–378, 1996.

[64] A. V. Dvorak, V. Wiggermann, G. Gilbert, I. M. Vavasour, E. L. MacMillan, L. Barlow, N. Wiley, P. Kozlowski, A. L. MacKay, A. Rauscher, *et al.*, "Multi-spin echo t2 relaxation imaging with compressed sensing (metrics) for rapid myelin water imaging," *Magnetic resonance in medicine*, vol. 84, no. 3, pp. 1264–1279, 2020.

[69] D. A. Yablonskiy, A. L. Sukstanskii, J. Luo, and X. Wang, "Voxel spread function method for correction of magnetic field inhomogeneity effects in quantitative gradient-echo-based mri," *Magnetic Resonance in Medicine*, vol. 70, no. 5, pp. 1283–1292, 2013. DOI: 10.1002/mrm.24585.

[72] B Mädler and A MacKay, "Towards whole brain myelin imaging," *International Society for Magnetic Resonance in Medicine, Berlin, Germany*, 2007.

[73] H. Liu, Q.-S. Xiang, R. Tam, A. V. Dvorak, A. L. MacKay, S. H. Kolind, A. Traboulsee, I. M. Vavasour, D. K. Li, J. K. Kramer, *et al.*, "Myelin water imaging data analysis in less than one minute," *NeuroImage*, vol. 210, p. 116 551, 2020.

[74] S.-H. Oh, M. Bilello, M. Schindler, C. E. Markowitz, J. A. Detre, and J. Lee, "Direct visualization of short transverse relaxation time component (vista)," *Neuroimage*, vol. 83, pp. 485–492, 2013.

Bibliography

[1] S. H. Kolind, "Myelin Water Imaging: Development at 3.0 t, application to the study of multiple sclerosis, and comparison to diffusion tensor imaging," Ph.D. dissertation, University of British Colombia, 2008.

[2] M. Simons and K.-A. Nave, "Oligodendrocytes: Myelination and axonal support," *Cold Spring Harbor perspectives in biology*, vol. 8, no. 1:a020479, 2015. DOI: 10.1101/cshperspect.a020479.

[3] D. K. Hartline, "What is myelin?" *Neuron Glia Biology*, vol. 4, no. 2, 153–163, 2008. DOI: 10.1017/S1740925X09990263.

[4] P. van Gelderen, J. A. de Zwart, J. Lee, P. Sati, D. S. Reich, and J. H. Duyn, "Nonexponential t2* decay in white matter," *Magnetic Resonance in Medicine*, vol. 67, no. 1, pp. 110–117, 2012. DOI: 10.1002/mrm.22990.

[5] E. Alonso-Ortiz, I. R. Levesque, and G. B. Pike, "Mri-based myelin water imaging: A technical review," *Magnetic Resonance in Medicine*, vol. 73, no. 1, pp. 70–81, 2015. DOI: 10.1002/mrm.25198.

[6] C. Raine, *Morphology of Myelin and Myelination*. In: Morell P., editor. Myelin. 2nd Edition ed. New York: Plenum Press, 1984.

[7] C Laule, E Leung, D. K. Li, A. L. Traboulsee, D. W. Paty, A. L. MacKay, and G. R. Moore, "Myelin water imaging in multiple sclerosis: Quantitative correlations with histopathology," *Multiple Sclerosis Journal*, vol. 12, no. 6, pp. 747–753, 2006, PMID: 17263002. DOI: 10.1177/1352458506070928.

[8] J. Lee, J.-W. Hyun, J. Lee, E.-J. Choi, H.-G. Shin, K. Min, Y. Nam, H. J. Kim, and S.-H. Oh, "So you want to image myelin using mri: An overview and practical guide for myelin water imaging," *Journal of Magnetic Resonance Imaging, Online ahead of print.*, vol. n/a, no. n/a, 2020 Feb 3. DOI: 10.1002/jmri.27059.

[9] M. D. Does, "Inferring brain tissue composition and microstructure via mr relaxometry," *NeuroImage*, vol. 182, pp. 136 –148, 2018, Microstructural Imaging, ISSN: 1053-8119. DOI: 10.1016/j.neuroimage.2017.12.087.

[10] D. Kumar, S. Siemonsen, C. Heesen, J. Fiehler, and J. Sedlacik, "Noise robust spatially regularized myelin water fraction mapping with the intrinsic b1-error correction based on the linearized version of the extended phase graph model," *Journal of Magnetic Resonance Imaging*, vol. 43, no. 4, pp. 800–817, 2016. DOI: 10.1002/jmri.25078.

[11] D. J. Griffiths, *Introduction to Quantum Mechanics*. Upper Saddle River, NJ, 2 edition: Pearson, 2004.

[12] D. G. Nishimura, *Principles of Magnetic Resonance Imaging*. Stanford Univ,1.1 edition, 2010.

[13] J. C. Gore and R. Kennan, *Physical and Physiological Basis of Magnetic Relaxation*. In Magnetic Resonance Imaging. Mosby, 1999, ch. 3.

[14] K. C. McPhee, "Relaxometry in the Human Brain Using High Field MRI," Ph.D. dissertation, University of Alberta, 2017.

[15] E. M. Haacke, R. W. Brown, M. R. Thompson, and R. Venkatesan, *Magnetic Resonance Imaging: Physical Principles and Sequence Design*. Wiley-Liss, 1st edition, 1999.

[16] M. T. Vlaardingerbroek and J. A. d. Boer, *Magnetic Resonance Imaging*. Google-Books-ID: n3e0QgAACAAJ: Springer, 2nd edition, 1999.

[17] V Vasilescu, E Katona, V Simplăceanu, and D. Demco, "Water compartments in the myelinated nerve. iii. pulsed nmr results.," *Experientia*, vol. 34, no. 11, pp. 1443–1444, 1978. DOI: 10.1007/BF01932339.

[18] R. S. Menon and P. S. Allen, "Application of continuous relaxation time distributions to the fitting of data from model systems and excised tissue," *Magnetic Resonance in Medicine*, vol. 20, no. 2, pp. 214–227, 1991. DOI: 10.1002/mrm.1910200205.

[19] A. Mackay, K. Whittall, J. Adler, D. Li, D. Paty, and D. Graeb, "In vivo visualization of myelin water in brain by magnetic resonance," *Magnetic Resonance in Medicine*, vol. 31, no. 6, pp. 673–677, 1994. DOI: 10.1002/mrm.1910310614.

[20] C. Beaulieu, F. R. Fenrich, and P. S. Allen, "Multicomponent water proton transverse relaxation and t2-discriminated water diffusion in myelinated and nonmyelinated nerve," *Magnetic Resonance Imaging*, vol. 16, no. 10, pp. 1201 –1210, 1998, ISSN: 0730-725X. DOI: 10.1016/S0730-725X(98)00151-9.

[21] S. Webb, C. A. Munro, R. Midha, and G. J. Stanisz, "Is multicomponent t2 a good measure of myelin content in peripheral nerve?" *Magnetic Resonance in Medicine*, vol. 49, no. 4, pp. 638–645, 2003. DOI: 10.1002/mrm.10411.

[22] C. Laule, P. Kozlowski, E. Leung, D. K. Li, A. L. MacKay, and G. W. Moore, "Myelin water imaging of multiple sclerosis at 7 t: Correlations with histopathology," *NeuroImage*, vol. 40, no. 4, pp. 1575 –1580, 2008, ISSN: 1053-8119. DOI: 10.1016/j.neuroimage.2007.12.008.

[23] K. P. Whittall, A. L. Mackay, D. A. Graeb, R. A. Nugent, D. K. B. Li, and D. W. Paty, "In vivo measurement of t2 distributions and water contents in normal human brain," *Magnetic Resonance in Medicine*, vol. 37, no. 1, pp. 34–43, 1997. DOI: 10.1002/mrm.1910370107.

[24] T. Prasloski, A. Rauscher, A. L. MacKay, M. Hodgson, I. M. Vavasour, C. Laule, and B. Mädler, "Rapid whole cerebrum myelin water imaging using a 3d grase sequence," *NeuroImage*, vol. 63, no. 1, pp. 533 –539, 2012, ISSN: 1053-8119. DOI: 10.1016/j.neuroimage.2012.06.064.

[25] R. M. Lebel and A. H. Wilman, "Transverse relaxometry with stimulated echo compensation," *Magnetic Resonance in Medicine*, vol. 64, no. 4, pp. 1005–1014, 2010. DOI: 10.1002/mrm.22487.

[26] T. Prasloski, B. Mädler, Q.-S. Xiang, A. MacKay, and C. Jones, "Applications of stimulated echo correction to multicomponent t2 analysis," *Magnetic Resonance in Medicine*, vol. 67, no. 6, pp. 1803–1814, 2012. DOI: 10.1002/mrm.23157.

[27] J. Hennig, "Echoes—how to generate, recognize, use or avoid them in mr-imaging sequences. part i: Fundamental and not so fundamental properties of spin echoes," *Concepts in Magnetic Resonance*, vol. 3, no. 3, pp. 125–143, 1991. DOI: 10.1002/cmr.1820030302.

[28] C. L. Lawson and R. J. Hanson, *Solving least squares problems*. IEnglewood Cliffs, NJ: Prentice-Hall, 1974.

[29] P. C. Hansen, "Analysis of discrete ill-posed problems by means of the l-curve," *SIAM Review*, vol. 34, no. 4, pp. 561–580, 1992. DOI: 10.1137/1034115.

[30] V. Wiggermann, I. M. Vavasour, S. Kolind, A. L. MacKay, G. Helms, and A. Rauscher, "Non-negative least squares computation for in vivo myelin mapping using simulated multi-echo spin-echo t2 decay data," *NMR in Biomedicine*, vol. 33, no. 12, e4277, 2020.

[31] D. A. Yablonskiy, "Quantitation of intrinsic magnetic susceptibility-related effects in a tissue matrix. phantom study," *Magnetic Resonance in Medicine*, vol. 39, no. 3, pp. 417–428, 1998. DOI: 10.1002/mrm.1910390312.

[32] D. Hwang, D.-H. Kim, and Y. P. Du, "In vivo multi-slice mapping of myelin water content using t2* decay," *NeuroImage*, vol. 52, no. 1, pp. 198 –204, 2010, ISSN: 1053-8119. DOI: 10.1016/j.neuroimage.2010.04.023.

[33] Y. P. Du, R. Chu, D. Hwang, M. S. Brown, B. K. Kleinschmidt-DeMasters, D. Singel, and J. H. Simon, "Fast multislice mapping of the myelin water fraction using multicompartment analysis of t decay at 3t: A preliminary postmortem study," *Magnetic Resonance in Medicine*, vol. 58, no. 5, pp. 865–870, 2007. DOI: 10.1002/mrm.21409.

[34] E. Alonso-Ortiz, I. R. Levesque, and G. B. Pike, "Multi-gradient-echo myelin water fraction imaging: Comparison to the multi-echo-spin-echo technique," *Magnetic Resonance in Medicine*, vol. 79, no. 3, pp. 1439–1446, 2018. DOI: 10.1002/mrm.26809.

[35] H.-G. Shin, S.-H. Oh, M. Fukunaga, Y. Nam, D. Lee, W. Jung, M. Jo, S. Ji, J. Y. Choi, and J. Lee, "Advances in gradient echo myelin water imaging at 3t and 7t," *NeuroImage*, vol. 188, pp. 835 –844, 2019, ISSN: 1053-8119. DOI: 10.1016/j.neuroimage.2018.11.040.

[36] D. A. Feinberg and K. Oshio, "Gradient-echo shifting in fast mri techniques (erase imaging) for correction of field inhomogeneity errors and chemical shift," *Journal of Magnetic Resonance (1969)*, vol. 97, no. 1, pp. 177–183, 1992.

[37] G. F. Piredda, T. Hilbert, E. J. Canales-Rodríguez, M. Pizzolato, C. von Deuster, R. Meuli, J. Pfeuffer, A. Daducci, J.-P. Thiran, and T. Kober, "Fast and high-resolution myelin water imaging: Accelerating multi-echo grase with caipirinha," *Magnetic Resonance in Medicine*, vol. 85, no. 1, pp. 209–222, 2021.

[38] A. MacKay, C. Laule, I. Vavasour, T. Bjarnason, S. Kolind, and B. Mädler, "Insights into brain microstructure from the t2 distribution," *Magnetic resonance imaging*, vol. 24, no. 4, pp. 515–525, 2006.

[39] I. M. Vavasour, K. P. Whittall, A. L. Mackay, D. K. Li, G. Vorobeychik, and D. W. Paty, "A comparison between magnetization transfer ratios and myelin water percentages in normals and multiple sclerosis patients," *Magnetic resonance in medicine*, vol. 40, no. 5, pp. 763–768, 1998.

[40] C. K. Jones, Q.-S. Xiang, K. P. Whittall, and A. L. MacKay, "Linear combination of multiecho data: Short t2 component selection," *Magnetic Resonance in Medicine: An Official Journal of the International Society for Magnetic Resonance in Medicine*, vol. 51, no. 3, pp. 495–502, 2004.

[41] J. P. Wansapura, S. K. Holland, R. S. Dunn, and W. S. Ball Jr, "Nmr relaxation times in the human brain at 3.0 tesla," *Journal of Magnetic Resonance Imaging: An Official Journal of the International Society for Magnetic Resonance in Medicine*, vol. 9, no. 4, pp. 531–538, 1999.

[42] H. E. Möller, L. Bossoni, J. R. Connor, R. R. Crichton, M. D. Does, R. J. Ward, L. Zecca, F. A. Zucca, and I. Ronen, "Iron, myelin, and the brain: Neuroimaging meets neurobiology," *Trends in neurosciences*, vol. 42, no. 6, pp. 384–401, 2019.

[43] C. Birkl, A. M. Birkl-Toeglhofer, V. Endmayr, R. Höftberger, G. Kasprian, C. Krebs, J. Haybaeck, and A. Rauscher, "The influence of brain iron on myelin water imaging," *Neuroimage*, vol. 199, pp. 545–552, 2019.

[44] C. M. Collins, W. Liu, W. Schreiber, Q. X. Yang, and M. B. Smith, "Central brightening due to constructive interference with, without, and despite dielectric resonance," *Journal of Magnetic Resonance Imaging: An Official Journal of the International Society for Magnetic Resonance in Medicine*, vol. 21, no. 2, pp. 192–196, 2005.

[45] C Jones, Q Xiang, K. Whittall, and A MacKay, "Calculating t2 and b1 from decay curves collected with non-180 refocusing pulses," in *11th annual meeting of the international society of magnetic resonance in medicine. Toronto, Canada*, vol. 1018, 2003.

[46] J. Hennig, "Multiecho imaging sequences with low refocusing flip angles," *Journal of Magnetic Resonance (1969)*, vol. 78, no. 3, pp. 397–407, 1988.

[47] A. Akhondi-Asl, O. Afacan, M. Balasubramanian, R. V. Mulkern, and S. K. Warfield, "Fast myelin water fraction estimation using 2d multislice cpmg," *Magnetic resonance in medicine*, vol. 76, no. 4, pp. 1301–1313, 2016.

[48] G. S. Drenthen, W. H. Backes, A. P. Aldenkamp, G. J. Op't Veld, and J. F. Jansen, "A new analysis approach for t2 relaxometry myelin water quantification: Orthogonal matching pursuit," *Magnetic resonance in medicine*, vol. 81, no. 5, pp. 3292–3303, 2019.

[49] L. E. Lee, E. Ljungberg, D. Shin, C. R. Figley, I. M. Vavasour, A. Rauscher, J. Cohen-Adad, D. K. Li, A. L. Traboulsee, A. L. MacKay, *et al.*, "Inter-vendor reproducibility of myelin water imaging using a 3d gradient and spin echo sequence," *Frontiers in neuroscience*, vol. 12, p. 854, 2018.

[50] C. L. Lankford and M. D. Does, "Propagation of error from parameter constraints in quantitative mri: Example application of multiple spin echo t2 mapping," *Magnetic resonance in medicine*, vol. 79, no. 2, pp. 673–682, 2018.

[51] K. C. McPhee and A. H. Wilman, "Transverse relaxation and flip angle mapping: Evaluation of simultaneous and independent methods using multiple spin echoes," *Magnetic resonance in medicine*, vol. 77, no. 5, pp. 2057–2065, 2017.

[52] S. M. Meyers, C. Laule, I. M. Vavasour, S. H. Kolind, B. Mädler, R. Tam, A. L. Traboulsee, J. Lee, D. K. Li, and A. L. MacKay, "Reproducibility of myelin water fraction analysis: A comparison of region of interest and voxel-based analysis methods," *Magnetic resonance imaging*, vol. 27, no. 8, pp. 1096–1103, 2009.

[53] S. J. Graham, P. L. Stanchev, and M. J. Bronskill, "Criteria for analysis of multicomponent tissue t2 relaxation data," *Magnetic Resonance in Medicine*, vol. 35, no. 3, pp. 370–378, 1996.

[54] L Chen, M Bernstein, J Huston, and S Fain, "Measurements of t1 relaxation times at 3.0 t: Implications for clinical mra," in *Proceedings of the 9th Annual Meeting of ISMRM, Glasgow, Scotland*, 2001.

[55] C. Labadie, J.-H. Lee, W. D. Rooney, S. Jarchow, M. Aubert-Frécon, C. S. Springer Jr, and H. E. Möller, "Myelin water mapping by spatially regularized longitudinal relaxographic imaging at high magnetic fields," *Magnetic resonance in medicine*, vol. 71, no. 1, pp. 375–387, 2014.

[56] H. Gudbjartsson and S. Patz, "The rician distribution of noisy mri data," *Magnetic resonance in medicine*, vol. 34, no. 6, pp. 910–914, 1995.

[57] S. H. Kolind, B. Mädler, S. Fischer, D. K. Li, and A. L. MacKay, "Myelin water imaging: Implementation and development at 3.0 t and comparison to 1.5 t measurements," *Magnetic Resonance in Medicine: An Official Journal of the International Society for Magnetic Resonance in Medicine*, vol. 62, no. 1, pp. 106–115, 2009.

[58] J. Guo, Q. Ji, and W. E. Reddick, "Multi-slice myelin water imaging for practical clinical applications at 3.0 t," *Magnetic resonance in medicine*, vol. 70, no. 3, pp. 813–822, 2013.

[59] L. I. Sacolick, L. Sun, M. W. Vogel, W. T. Dixon, and I. Hancu, "Fast radiofrequency flip angle calibration by bloch–siegert shift," *Magnetic resonance in medicine*, vol. 66, no. 5, pp. 1333–1338, 2011.

[60] G. S. Drenthen, W. H. Backes, A. P. Aldenkamp, and J. F. Jansen, "Applicability and reproducibility of 2d multi-slice grase myelin water fraction with varying acquisition acceleration," *Neuroimage*, vol. 195, pp. 333–339, 2019.

[61] N. Ben-Eliezer, D. K. Sodickson, and K. T. Block, "Rapid and accurate t2 mapping from multi–spin-echo data using bloch-simulation-based reconstruction," *Magnetic resonance in medicine*, vol. 73, no. 2, pp. 809–817, 2015.

[62] K. C. McPhee and A. H. Wilman, "T2 quantification from only proton density and t2-weighted mri by modeling actual refocusing angles," *NeuroImage*, vol. 118, pp. 642–650, 2015.

[63] A. Lesch, M. Schlöegl, M. Holler, K. Bredies, and R. Stollberger, "Ultrafast 3d bloch–siegert b-mapping using variational modeling," *Magnetic resonance in medicine*, vol. 81, no. 2, pp. 881–892, 2019.

[64] A. V. Dvorak, V. Wiggermann, G. Gilbert, I. M. Vavasour, E. L. MacMillan, L. Barlow, N. Wiley, P. Kozlowski, A. L. MacKay, A. Rauscher, *et al.*, "Multi-spin echo t2 relaxation imaging with compressed sensing (metrics) for rapid myelin water imaging," *Magnetic resonance in medicine*, vol. 84, no. 3, pp. 1264–1279, 2020.

[65] Z. Wu, H. He, Y. Sun, Y. Du, and J. Zhong, "High resolution myelin water imaging incorporating local tissue susceptibility analysis," *Magnetic Resonance Imaging*, vol. 42, pp. 107 –113, 2017, ISSN: 0730-725X. DOI: 10.1016/j.mri.2017.06.005.

[66] J. Lee, Y. Nam, J. Y. Choi, E. Y. Kim, S.-H. Oh, and D.-H. Kim, "Mechanisms of t2* anisotropy and gradient echo myelin water imaging," *NMR in Biomedicine*, vol. 30, no. 4, e3513, 2017. DOI: 10.1002/nbm.3513.

[67] M. Bouhrara, M. C. Maring, and R. G. Spencer, "A simple and fast adaptive nonlocal multispectral filtering algorithm for efficient noise reduction in magnetic resonance imaging," *Magnetic resonance imaging*, vol. 55, pp. 133–139, 2019.

[68] E. Alonso-Ortiz, I. R. Levesque, R. Paquin, and G. B. Pike, "Field inhomogeneity correction for gradient echo myelin water fraction imaging," *Magnetic Resonance in Medicine*, vol. 78, no. 1, pp. 49–57, 2017. DOI: 10.1002/mrm.26334.

[69] D. A. Yablonskiy, A. L. Sukstanskii, J. Luo, and X. Wang, "Voxel spread function method for correction of magnetic field inhomogeneity effects in quantitative gradient-echo-based mri," *Magnetic Resonance in Medicine*, vol. 70, no. 5, pp. 1283–1292, 2013. DOI: 10.1002/mrm.24585.

[70] H. Lee, Y. Nam, H.-J. Lee, J.-J. Hsu, R. G. Henry, and D.-H. Kim, "Improved three-dimensional multi-echo gradient echo based myelin water fraction mapping with phase related artifact correction," *NeuroImage*, vol. 169, pp. 1–10, 2018.

[71] Y. Nam, J. Lee, D. Hwang, and D.-H. Kim, "Improved estimation of myelin water fraction using complex model fitting," *NeuroImage*, vol. 116, pp. 214–221, 2015.

[72] B Mädler and A MacKay, "Towards whole brain myelin imaging," *International Society for Magnetic Resonance in Medicine, Berlin, Germany*, 2007.

[73] H. Liu, Q.-S. Xiang, R. Tam, A. V. Dvorak, A. L. MacKay, S. H. Kolind, A. Traboulsee, I. M. Vavasour, D. K. Li, J. K. Kramer, *et al.*, "Myelin water imaging data analysis in less than one minute," *NeuroImage*, vol. 210, p. 116 551, 2020.

[74] S.-H. Oh, M. Bilello, M. Schindler, C. E. Markowitz, J. A. Detre, and J. Lee, "Direct visualization of short transverse relaxation time component (vista)," *Neuroimage*, vol. 83, pp. 485–492, 2013.